NASA CR - 135317

MERCURY ION THRUSTER RESEARCH - 1977

PREPARED FOR

LEWIS RESEARCH CENTER

NATIONAL AERONAUTICS AND SPACE ADMINISTRATION

GRANT NGR-06-002-112

(NASA-CR-135317) MERCURY ION THRUSTER RESEARCH, 1977 Annual Report, 1 Dec. 1976 - 1 Dec. 1977 (Colorado State Univ.) 163 p HC A08/MF A01 CSCL 21C

N78-15167

Unclas

G3/20 01833

Annual Report

December 1977

Paul J. Wilbur
Department of Mechanical Engineering
Colorado State University
Fort Collins, Colorado

1. Report No.	2. Government Accession No	3 Recipient's Catalog No
NASA CR-135317		

4. Title and Subtitle	5. Report Date
MERCURY ION THRUSTER RESEARCH - 1977	6. Performing Organization Code
7. Author(s) Paul J. Wilbur	8 Performing Organization Report No.
9. Performing Organization Name and Address Department of Mechanical Engineering, Colorado State University, Fort Collins, Colorado 80523	10 Work Unit No.
	11. Contract or Grant No. NGR-06-002-112
12. Sponsoring Agency Name and Address National Aeronautics and Space Administration, Washington, D. C. 20546	13. Type of Report and Period Covered Dec. 1, 1976 - Dec. 1, 1977
	14. Sponsoring Agency Code

15 Supplementary Notes

Grant Monitor, William Kerslake
Spacecraft Technology Div.
NASA Lewis Research Center
Cleveland, Ohio 44135

16. Abstract

The measured ion beam divergence characteristics of two and three-grid, multiaperture accelerator systems are presented. The effects of perveance, geometry, net-to-total accelerating voltage, discharge voltage and propellant are examined. Three-grid systems are shown to exhibit less divergent beams than two-grid systems. This difference becomes most pronounced at low net-to-total accelerating voltage ratios. The screen-to-accelerator grid separation distance and net-to-total accelerating voltage ratio are shown to effect the divergence angle greatly. The accelerator hole diameter-to-screen hole diameter ratio is shown to have the greatest effect on the maximum obtainable perveance. A study of the main discharge keeper electrode shows that this electrode can be eliminated without degrading thruster performance. Studies on divergent and radial magnetic field 15-cm diameter thrusters are presented; they show that the screen grid can be biased slightly above cathode potential to reduce sputter damage to this grid without degrading thruster performance substantially. The applicability of the model describing doubly-charged ion densities in mercury thrusters is demonstrated for an 8-cm diameter thruster. The results of detailed Langmuir probing of the interior of an operating cathode are presented. These results are used to determine the ionization fraction as a function of position upstream of the cathode orifice. A mathematical model of discharge chamber electron diffusion and collection processes is presented. Scaling laws which should be useful in estimating performance of large diameter and/or high specific impulse thrusters are presented. A model describing the production of ionized molecular nitrogen in ion thrusters is presented.

17. Key Words (Suggested by Author(s))	18. Distribution Statement
Electrostatic Thruster Hollow Cathode	Unclassified - Unlimited

19. Security Classif. (of this report)	20. Security Classif. (of this page)	21. No. of Pages	22. Price*
Unclassified	Unclassified	166	

* For sale by the National Technical Information Service, Springfield, Virginia 22161

NASA-C-168 (Rev 10-75)

TABLE OF CONTENTS

ION BEAM DIVERGENCE CHARACTERISTICS
OF TWO-GRID ACCELERATOR SYSTEMS

Graeme Aston

Knowledge of ion* beam divergence characteristics for multi-aperture accelerator systems is important for both electric space propulsion and ground applications of electron-bombardment ion sources. A highly collimated beam (minimum off-axis ion velocity components) is generally preferred for both applications. The amount of ion beam divergence depends on the geometrical grid parameters and operating conditions of the accelerator system. Theoretical approaches used to date for predicting the performance of multiaperture accelerator systems have shown general trends only.[1-4] These theoretical approaches have been limited to the investigation of single aperture accelerator systems only. Previous experimental results have shown differences in the ion beam divergence characteristics of single and multiaperture accelerator systems.[5] A detailed experimental investigation was therefore undertaken to determine ion beam divergence over a wide range of geometrical and operating parameters of multiaperture accelerator systems.

---

* Since this section deals only with singly charged positive ions, the term "ion" is used with the exclusive meaning "singly charged positive ion."

Nomenclature

ℓ_g = Grid separation distance.

d_s = Screen hole diameter.

d_a = Accelerator hole diameter.

t_s = Screen grid thickness.

t_a = Accelerator grid thickness.

ℓ_e = Effective acceleration length.

V_T = Total accelerating voltage.

V_n = Net accelerating voltage.

V_D = Discharge voltage.

V_S = Sheath potential.

V_p = Plasma potential.

R = Net-to-total accelerating voltage ratio.

α = Ion beam divergence angle.

f_D = Ion beam divergence factor.

J_B = Beam current per hole.

q = Ion charge.

ε_o = Free space permittivity.

M_i = Ion mass.

ϕ_i = Propellant first ionization potential.

Ion Beam Formation

The ion extraction system chosen for this study was the two-grid accelerator geometry common to most electron-bombardment ion sources. Figure 1(a) depicts a portion of this multiaperture system showing the co-axial hole geometry and ion beamlet formation. Figure 2 illustrates

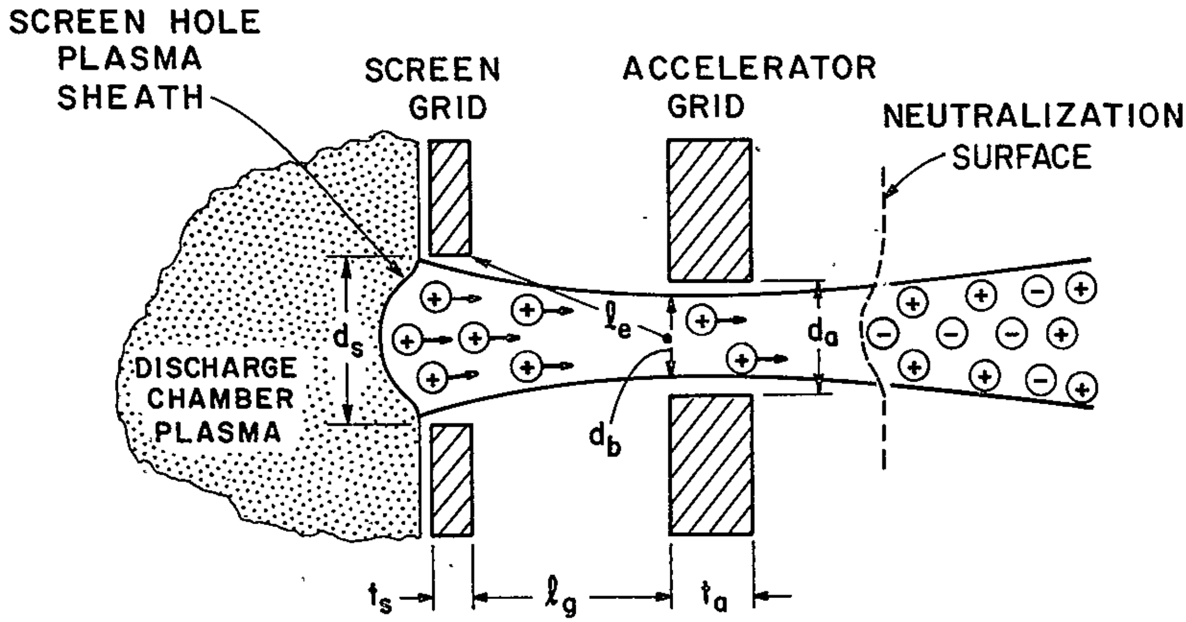

a) NORMAL OPERATION

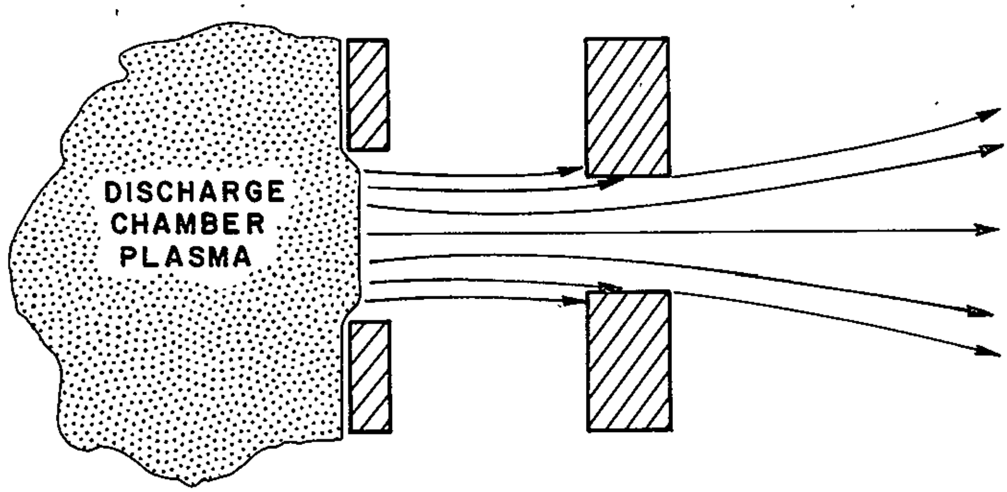

b) HIGH IMPINGEMENT OPERATION

ION BEAMLET FORMATION

FIGURE 1

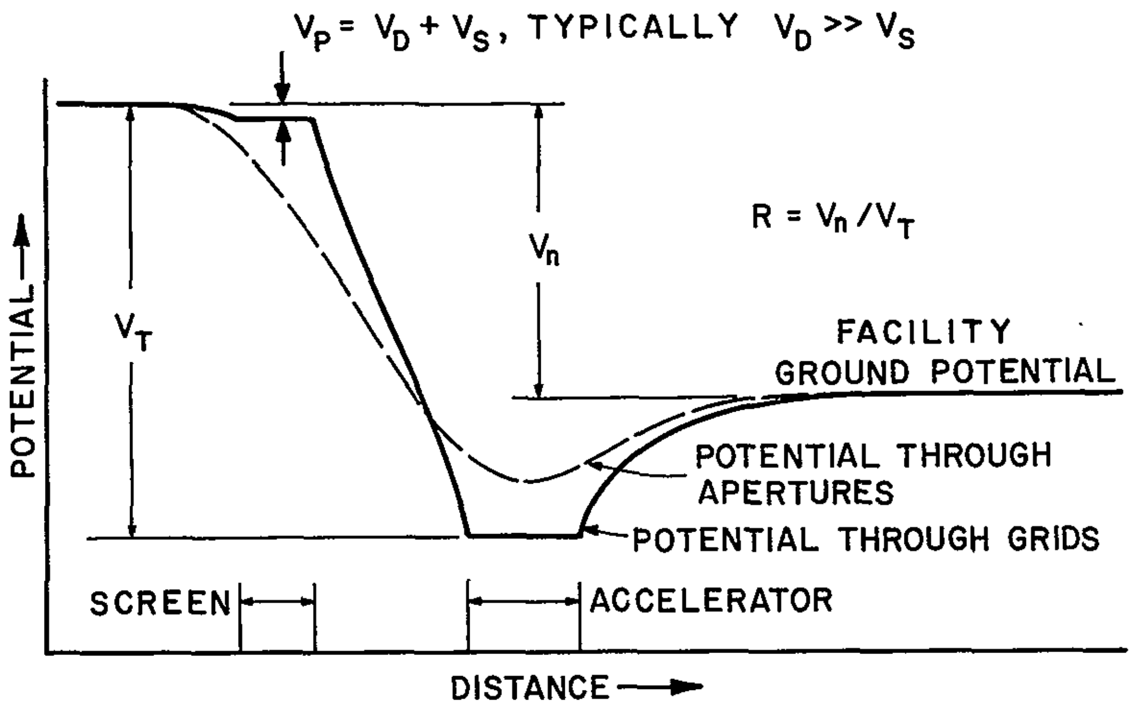

ACCELERATOR SYSTEM POTENTIAL VARIATION

FIGURE 2

the variation in electrical potential associated with the grid geometry of Fig. 1(a).

A low density singly ionized plasma is generated within a discharge chamber by electron-bombardment of neutral propellant atoms. The discharge chamber is at a potential a few tens of volts positive of the screen grid, which is at a high positive potential (Fig. 2). Around each screen hole a stable plasma sheath is formed. This sheath is a space-charge limited, emissive surface of positive ions from the discharge plasma. The ions reach the sheath with the Bohm velocity[6] and are accelerated by the strong electric field between the positive sheath and negative accelerator grid hole (Fig. 2). Depending upon the amount of focusing that occurs, most of the ions will pass through the accelerator grid hole and be ejected at high velocity into the region beyond (downstream side of the grids).

The ion, or beam current leaving the accelerator system is space-charge limited, so that the accelerator system resembles a vacuum diode. The perveance for a parallel plate diode can be obtained from Child's law[7]

$$\frac{J_B}{V_T{}^{3/2}} = \frac{\pi\varepsilon_0}{9}\left[\frac{2q}{M_i}\right]^{\frac{1}{2}}\left[\frac{d_S}{\ell}\right]^2 . \qquad (1)$$

The assumption has been made that the area of ion emission is $\pi d_S^2/4$. This planar expression has been found to agree well with the maximum beam current capacity per hole for a two-grid accelerator system if the effective acceleration length ℓ_e, is used in place of ℓ, where

$$\ell_e = \left[\ell_g^2 + \frac{d_S^2}{4}\right]^{\frac{1}{2}} . \qquad (2)$$

With this substitution, beam current variations may be expressed in terms of normalized perveance per hole

$$NP/H = \frac{J_B}{V_T^{3/2}} \left(\frac{\ell_e}{d_S}\right)^2 = \frac{\pi \varepsilon_o}{9} \left(\frac{2q}{M_i}\right)^{\frac{1}{2}} . \qquad (3)$$

Equation 3 indicates there is an upper limit to the normalized perveance per hole for a particular propellant. For mercury, the propellant of interest for electric space propulsion, this maximum value is 3.03 x 10^{-9} amp/volt$^{3/2}$. For argon, the test gas used in this study, this maximum value is 6.79 x 10^{-9} amp/volt$^{3/2}$. Normalized perveance per hole $\left(J_B/V_T^{3/2}\right)(\ell_e/d_S)^2$, will be used to describe the ion extraction performance of each grid set investigated.

Ion focusing effects occur in two regions of the accelerator system; between the grids and just downstream of the grids. Ions between the grids tend to follow the electric field lines passing from the screen hole plasma sheath through the accelerator hole. This tendency to follow electric field lines is most evident near the plasma sheath, where the ion velocity is small. The position and shape of the screen hole plasma sheath is crucial to this phase of the ion focusing process because it determines the local accelerating electric field distribution. Both screen hole plasma sheath position and shape depend on the ion current being extracted and the accelerator system geometry. In normal operation the shape of the plasma sheath is similar to that shown in Fig. 1(a). As plasma density increases the sheath moves further into the screen hole to satisfy the requirement of space-charge limited ion current emission from the discharge chamber plasma. The sheath shape becomes flatter and direct ion impingement upon the accelerator grid begins to occur (Fig. 1(b)). Further plasma density increases result in further ion focusing degradation. In practice this high impingement limits the ion current which can be extracted from an accelerator system.

As the focused ions leave the accelerator system, electrons are injected into the beam to maintain a neutral charge efflux. These neutralization electrons spread rapidly throughout the beam producing a neutral plasma. Because of the negative accelerator grid potential, neutralization electrons which approach the accelerator holes are repulsed by electrostatic forces. The result is a neutralization, or equipotential, surface created slightly downstream from the accelerator grid which is at approximately facility ground potential (Fig. 1(a)). Between the accelerator holes and the neutralization surface the ions are decelerating through a region of retarding electric field (Fig. 2). Although the deceleration incurred is less than the acceleration imparted by the grid set, it is still sufficient to defocus the ion trajectories significantly. However, once these ions reach the neutralization surface, electrostatic shielding by the beam plasma nullifies the accelerator grid effect and little additional change in ion trajectories occurs. Ion defocusing decreases as the net-to-total accelerating voltage ratio R, (Fig. 2) increases so it would appear desirable to have R as near unity as possible. In practice however, a value of R = 1.0 cannot be reached because neutralization electrons will backstream through the accelerator holes when the negative accelerator grid potential is too small.

Both regions of ion focusing mentioned above were examined for their contribution to the overall ion beam divergence. Ion focusing between the grids was varied by changing the ion beam current, the accelerator system geometry, and the total accelerating and discharge voltages. Ion defocusing was varied by changing the net-to-total accelerating voltage ratio.

Apparatus and Procedure

For this study, a mildly divergent magnetic field 8-cm diameter electron-bombardment ion source was constructed. Tungsten wire filaments were used as both the main and neutralizer cathode emitters. The magnetic field was derived from a long solenoidal winding extending the length of the discharge chamber, with additional coil windings positioned at the chamber's upstream end. The coil geometry was such that the field at the downstream end was sixty percent that of the upstream end. A cylindrical anode was employed and non-magnetic stainless steel construction used throughout the source. Further design details and operating characteristics for the source are found in Reference [8]. Mercury is the propellant of principle interest for electric space propulsion, but because of the inability to change ion source operating conditions rapidly with mercury it was not used for this study. Argon was chosen as propellant because of its availability and the ease and speed with which flow rates could be set and altered.

The screen and accelerator grids were made from thin flat sheet graphite. The grid aperture pattern used comprised a nineteen hole hexagonal array with a center-to-center hole spacing of 2.54 mm. It was felt this number of holes adequately modelled the adjacent screen hole interactions found in full-size grid systems. Variable grid separation was accomplished by using various numbers of thin mica washers (0.254 mm thick). The grid sets were fastened together with four insulated stainless steel bolts. Alignment of the screen and accelerator grids was accomplished by hand beneath a large illuminated magnifying glass; this straightforward technique was found to produce good data reproducibility. The assembled accelerator system was placed on a masked down discharge chamber, which insured ion extraction from a near uniform plasma. Calculations predicted the greatest spatial variation in discharge chamber plasma density across the 1 cm^2 hexagonal hole array would be less than 5%. Grid separation could be checked with feeler gauges when cold, but while the source was operating and the grids were hot they could only be examined visually. While some grid warpage could occur during operation, the magnitude of this warpage should be small because the grids were made of carbon and the greatest distance between grid supports was less than 2-cm. All source operation was conducted in a 30-cm pyrex bell jar. Average bell jar pressure was 1×10^{-4} torr.

Beam divergence measurements were accomplished using a movable probe rake containing twenty individual Faraday ion current sensors described in Reference [8]. This probe rake was positioned normal to the beam axis and 16.7 cm downstream of the accelerator system. Figure 3 shows the ion source and probe rake in position. The probes were screened and biased to reflect neutralization electrons and low energy charge exchange ions present in the beam plasma. After stable source operation was achieved, the probe rake was centered along the beam axis. Beam current was varied by adjusting the refractory cathode current and hence electron emission and discharge chamber plasma density. Each grid set geometry investigated was operated over a range of increasing emission levels to the maximum beam current obtainable from that grid set. The approach to this maximum was usually characterized by a rapid increase in accelerator grid impingement current and a negligible beam current increase. Ion beam profiles were obtained at selected beam currents leading up to this maximum. Each profile consisted of twenty ion current density measurements, corresponding to the ion current received by each Faraday probe as a function of its

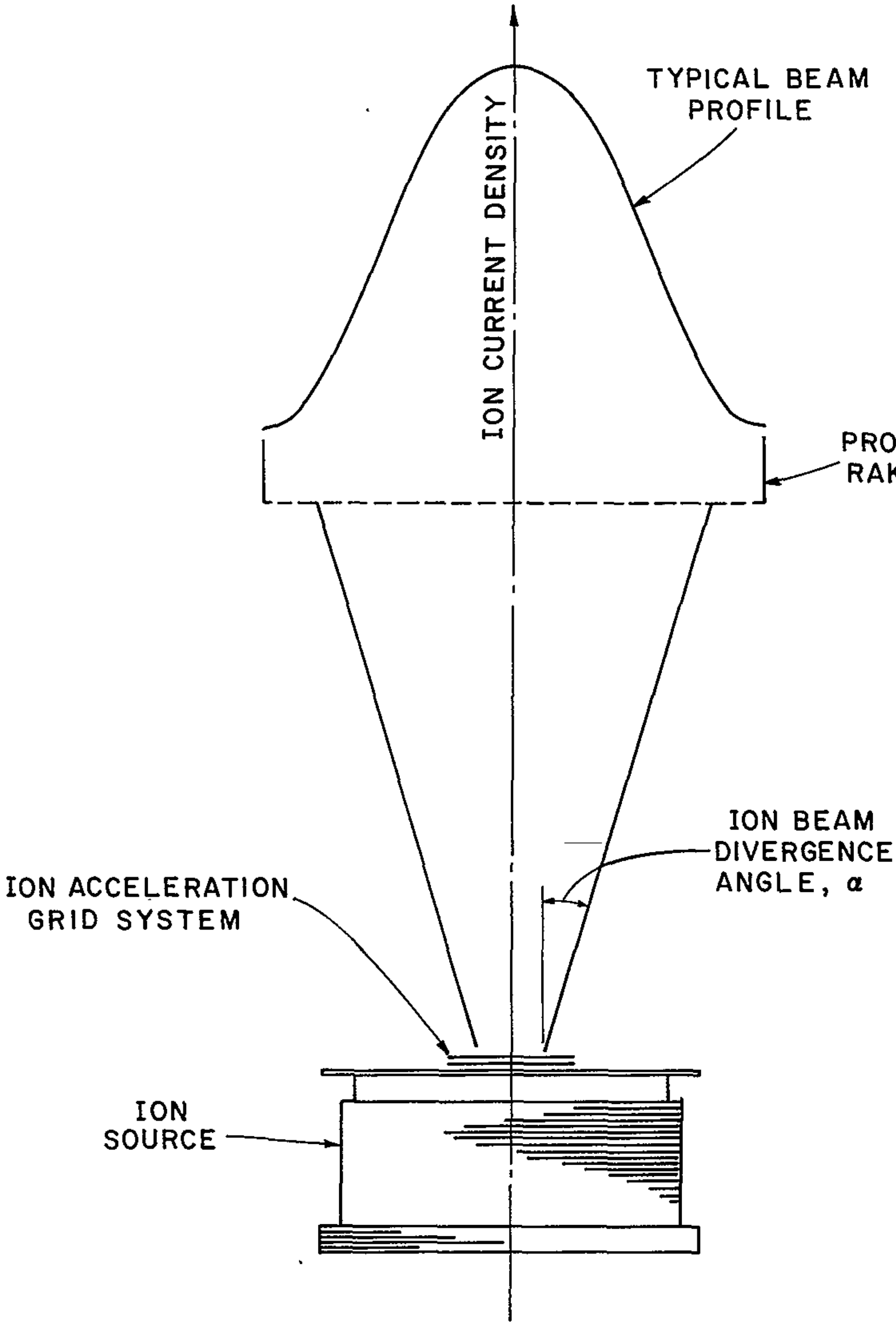

METHOD OF OBTAINING ION BEAM PROFILES

FIGURE 3

position normal to the beam axis. Figure 3 shows a typical ion beam profile. From these profiles ion beam divergence could be quantified by calculating the ion beam divergence angle α, (Fig. 3). The ion beam divergence angle was defined as the truncated cone angle enclosing 95% of the total integrated beam current. Another less obvious parameter for determining ion beam divergence is the ion beam divergence factor f_D, which is of considerable interest for ion thruster applications of electron-bombardment ion sources. The divergence factor is the ratio of the net axial thrust produced by the divergent ion beam to the thrust that would be produced if the ion beam were perfectly collimated. Both ion beam divergence angle and ion beam divergence factor were the calculated parameters (based on experimental measurements) of primary interest to this study. The following equations were used in their determination

$$\alpha = \text{Arctan}\left(\frac{R_\alpha - R_B}{16.7}\right) \quad , \tag{4}$$

$$f_D = \frac{\sum_{i=1}^{77} J_i \; R_i \; \overline{\text{Cos}\,\beta_i}}{\sum_{i=1}^{77} J_i \; R_i} \quad , \tag{5}$$

where

R_α = radius normal to the beam axis defining a cone enclosing 95% of the total integrated beam current,

R_B = ion beam radius at accelerator grid ,

J_i = probe current for the i^{th} probe (an interpolation routine was used to increase the number of probe data points from 20 to 77) ,

R_i = distance from ion beam axis to i^{th} probe ,

β_i = angle formed by intersection of a line extending from the center of the ion source grid set to the i^{th} probe and the ion beam axis.

Results and Discussion

The effect of grid geometry variations on ion beam divergence was determined by independently varying the grid separation distance ℓ_g, accelerator hole diameter d_a, screen grid thickness t_s and accelerator grid thickness t_a. To non-dimensionalize the geometrical grid parameters they were divided by the screen hole diameter d_s, which remained at 2.06 mm throughout this study. The precision of the data obtained was verified by repeatedly testing various grid set geometries at different times with the grids reassembled and realigned for each test. The results of these tests showed a maximum variation in α and f_D of $\pm$ 0.5° and $\pm$ 0.001 respectively. The absolute accuracy of the data is thought to be better than $\pm$ 1.0° for α, and better than $\pm$ 0.002 for f_D. A tabular listing of the experimental results presented graphically in this section can be found in Appendix I.

Figure 4 shows the effect of propellant flow rate variations on ion beam divergence for a grid geometry, the total accelerating voltage, discharge voltage and net-to-total accelerating voltage ratio typical of present mercury ion thrusters[9, 10] and ground-based argon ion sources.[11, 12] An almost five-fold variation in flow rate is seen to alter the grid systems' divergence characteristics to a very minor extent. The small, consistant beam divergence angle decrease with increasing propellant flow rate shown in Figure 4 has been reported previously by Altenburg, et.al.[13] The present data verifies those observations. For very small flow rates

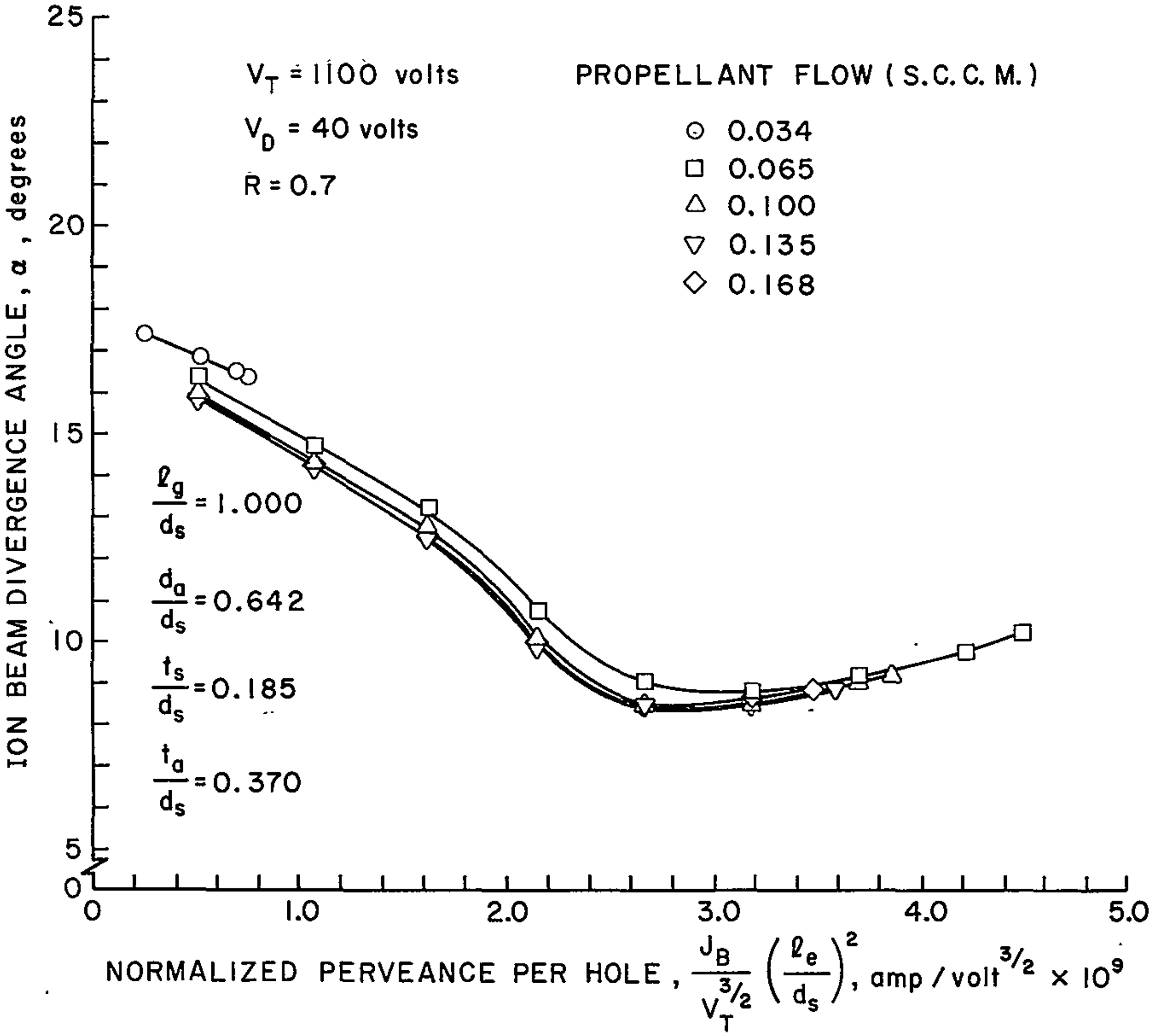

EFFECT OF ARGON FLOW RATE ON ION BEAM DIVERGENCE

FIGURE 4

the discharge became unstable and extinguished before any accelerator system limitation was reached (circles in Fig. 4). For the remainder of the tests reported herein the ion source was operated at the minimum flow rate which would give stable source operation up to the maximum beam current obtainable from the grid set being tested. This resulted in a propellant flow rate which varied from 0.075 to 0.125 Standard Cubic Centimeters per Minute (S.C.C.M.) over the range of grid set geometries and operating conditions investigated. Figure 4 shows these flow rate variations should produce a negligible effect on the ion beam divergence characteristics of a particular grid set geometry.

Figure 4 shows also that there is an optimum perveance, corresponding to an optimum screen hole sheath position and shape, which gives the lowest ion beam divergence angle. This minimum divergence angle defines the accelerator system operating condition most desirable from an ion focusing viewpoint. It is interesting to note that grid set operation at the minimum beam divergence angle is also close to the maximum beam current at which one would prefer to operate. Increasing the beam current beyond this point, thereby allowing the screen hole sheath to become flatter in shape (Fig. 1(b)), results in an increasing fraction of accelerated ions impinging directly upon the accelerator grid. The associated increase in ion sputtering damage seriously degrades accelerator grid lifetime.

Figures 5 through 8 show the beam divergence variations for changes to the grid separation ratio $\frac{\ell_g}{d_s}$, and net-to-total accelerating voltage ratio R. For these data the accelerator hole diameter ratio $\frac{d_a}{d_s}$, screen grid thickness ratio $\frac{t_s}{d_s}$, and accelerator grid thickness ratio $\frac{t_a}{d_s}$, were held constant at values of 0.642, 0.185 and 0.370 respectively. Qualitatively all curve shapes are similar. This similarity in curve shape and the fact that

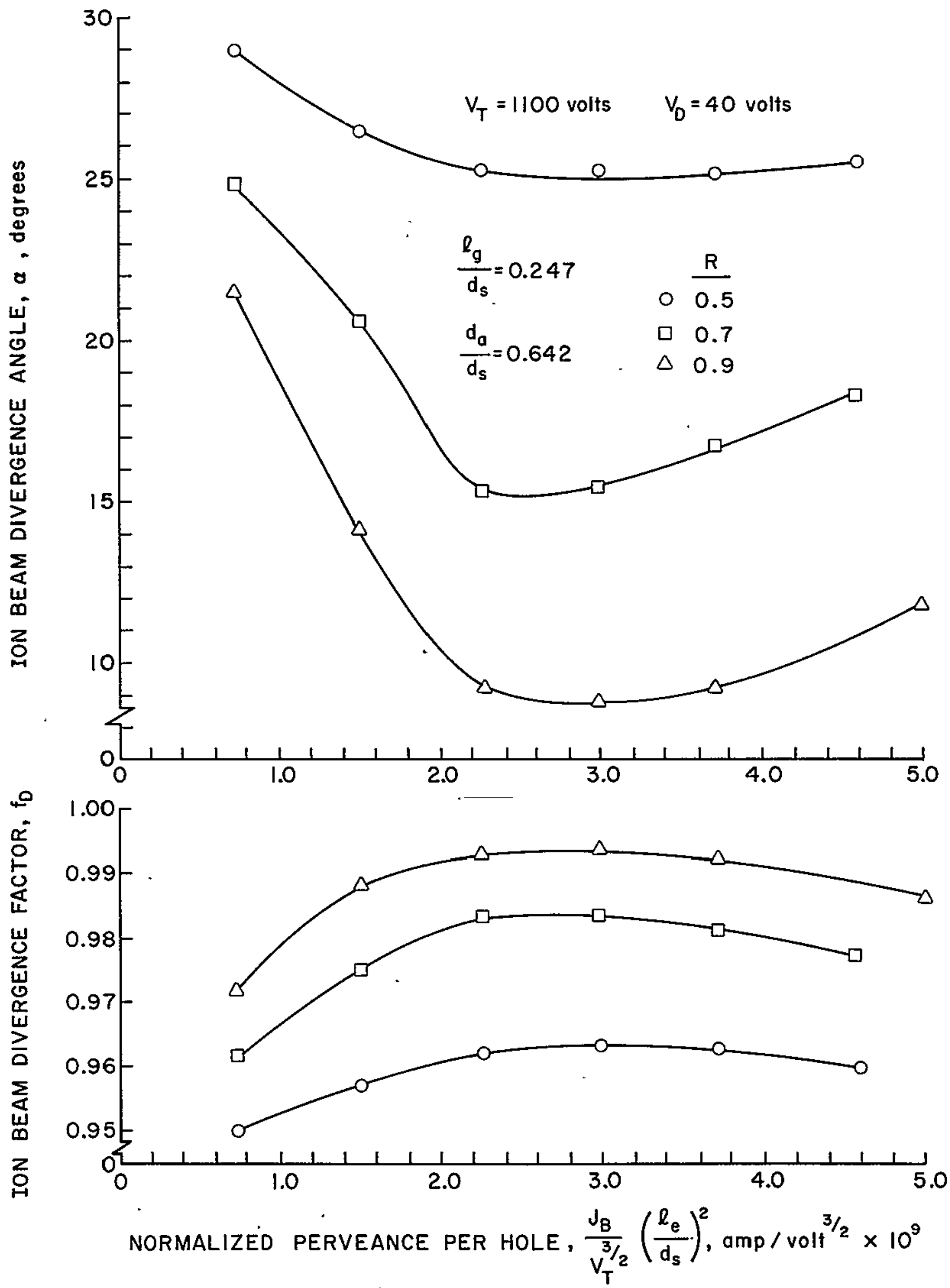

EFFECT OF R ON ARGON ION BEAM DIVERGENCE

(small grid separation ratio , $\frac{\ell_g}{ds}$ = 0.247).

FIGURE 5

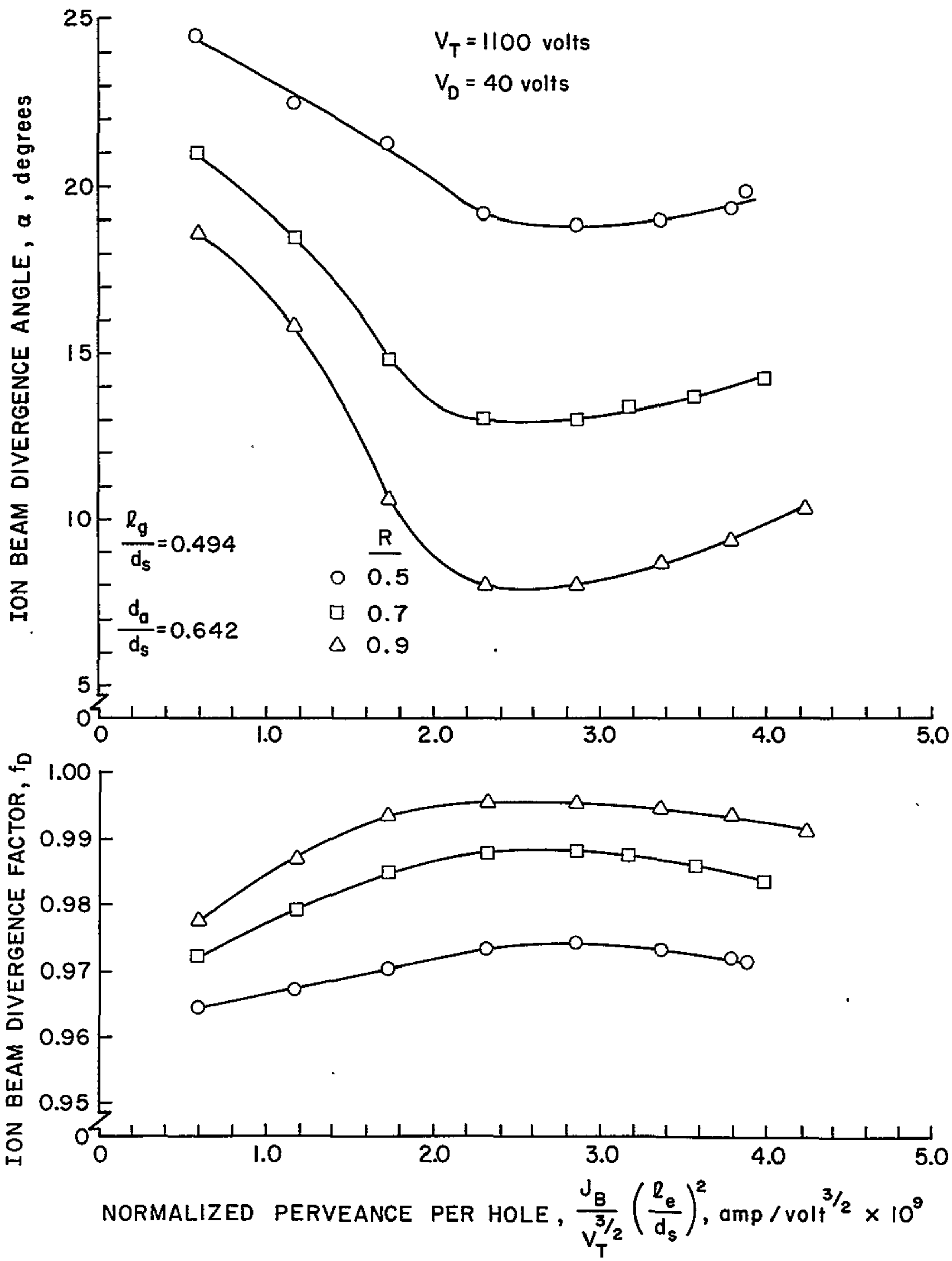

EFFECT OF R ON ARGON ION BEAM DIVERGENCE

(medium grid separation ratio, $\frac{\ell_g}{d_s}$ = 0.494).

FIGURE 6

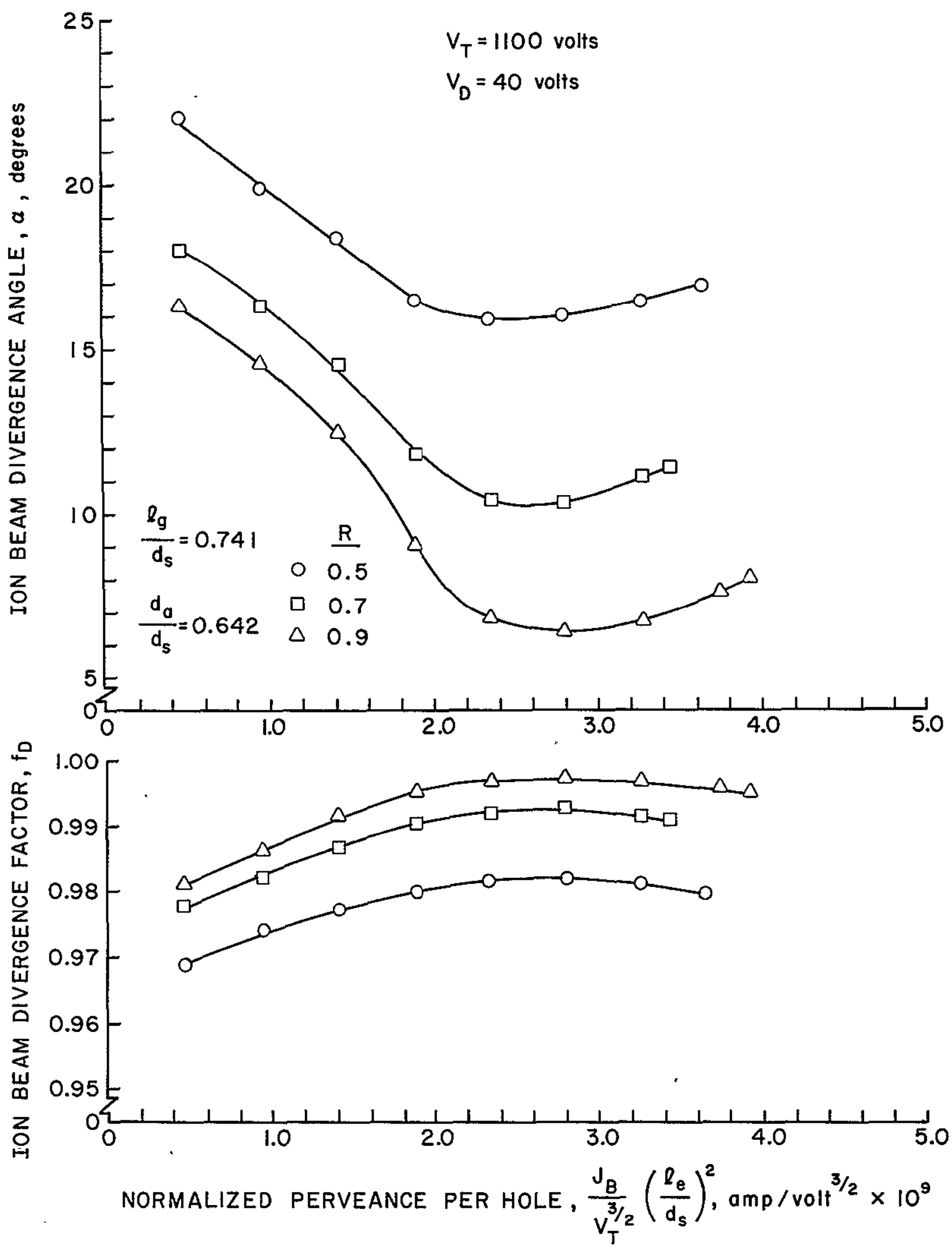

EFFECT OF R ON ARGON ION BEAM DIVERGENCE

(large grid separation ratio, $\frac{\ell_g}{d_s}$ = 0.741).

FIGURE 7

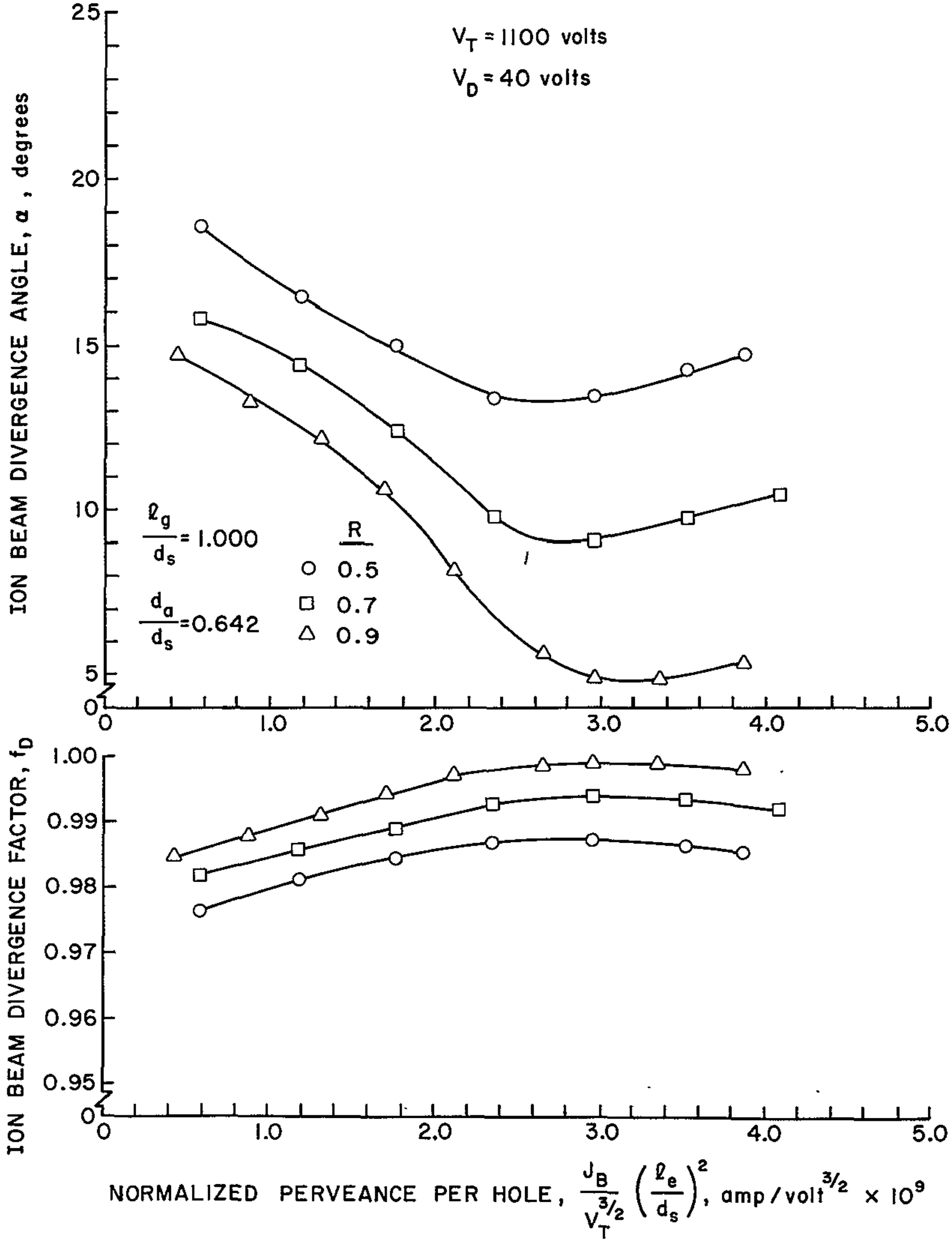

EFFECT OF R ON ARGON ION BEAM DIVERGENCE

(very large grid separation ratio, $\frac{\ell_g}{d_s}$ = 1.000).

FIGURE 8

variations in the maximum normalized perveance per hole* are small indicates the usefulness of normalized perveance per hole as a correlating parameter. Increasing the grid separation ratio for a constant net-to-total accelerating voltage ratio decreases ion beam divergence angles, with corresponding ion beam divergence factor increases. This is presumably a result of the more planar equipotential surfaces associated with the larger grid separation distance. Similarly, increasing the net-to-total accelerating voltage ratio for a constant grid separation ratio decreases overall ion beam divergence. This effect is greatest for the smallest grid separation ratio tested and decreases with grid separation ratio increases. The uniform manner in which net-to-total accelerating voltage ratio variations raise or lower the ion beam divergence angle curves of Figs. 5 through 8, suggests these ion defocusing variations do not affect the ion focusing processes characteristic of each grid separation ratio. Figures 5 through 8 show that large ion beam divergence variations are possible with two-grid accelerator systems. A change in the minimum ion beam divergence angle from 25.1° to 4.9° is observed when going from values of $\frac{\ell_g}{d_s} = 0.247$ and R = 0.5 to $\frac{\ell_g}{d_s} = 1.000$ and R = 0.9.

Figures 9 through 11 show the effect of accelerator hole diameter ratio, screen grid thickness ratio and accelerator grid thickness ratio variations on ion beam divergence. Beam divergence angle changes are observed to be very slight for large variations in these parameters. However, decreasing the accelerator hole diameter ratio substantially decreases the maximum normalized perveance per hole, or beam current,

---

* It is important to realize that constant normalized perveance per hole does not mean constant beam current. If the total accelerating voltage V_T, is held constant, the beam current will increase as the grid separation ratio is decreased (Equation 3).

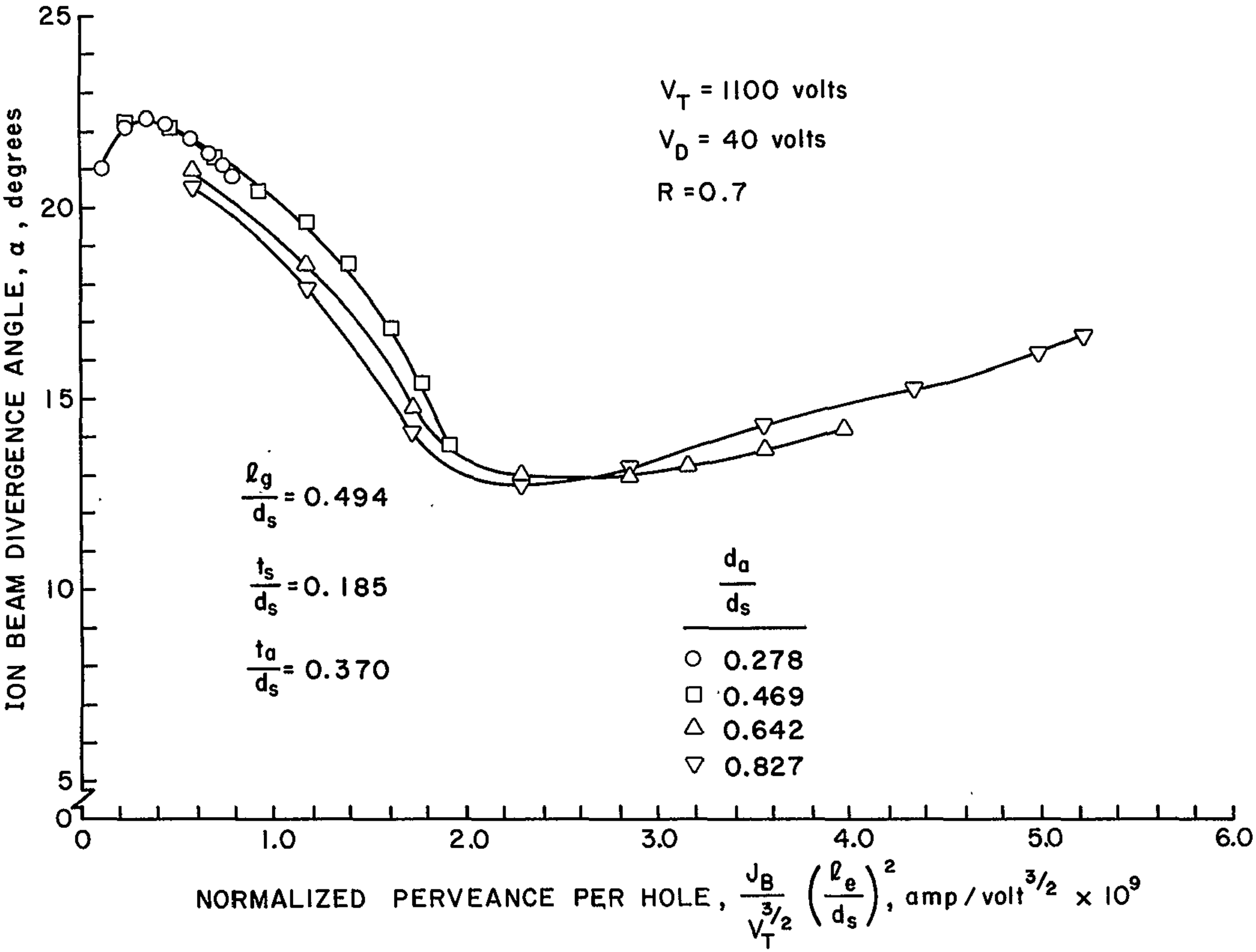

FIGURE 9

EFFECT OF ACCELERATOR HOLE DIAMETER RATIO ON ARGON ION BEAM DIVERGENCE

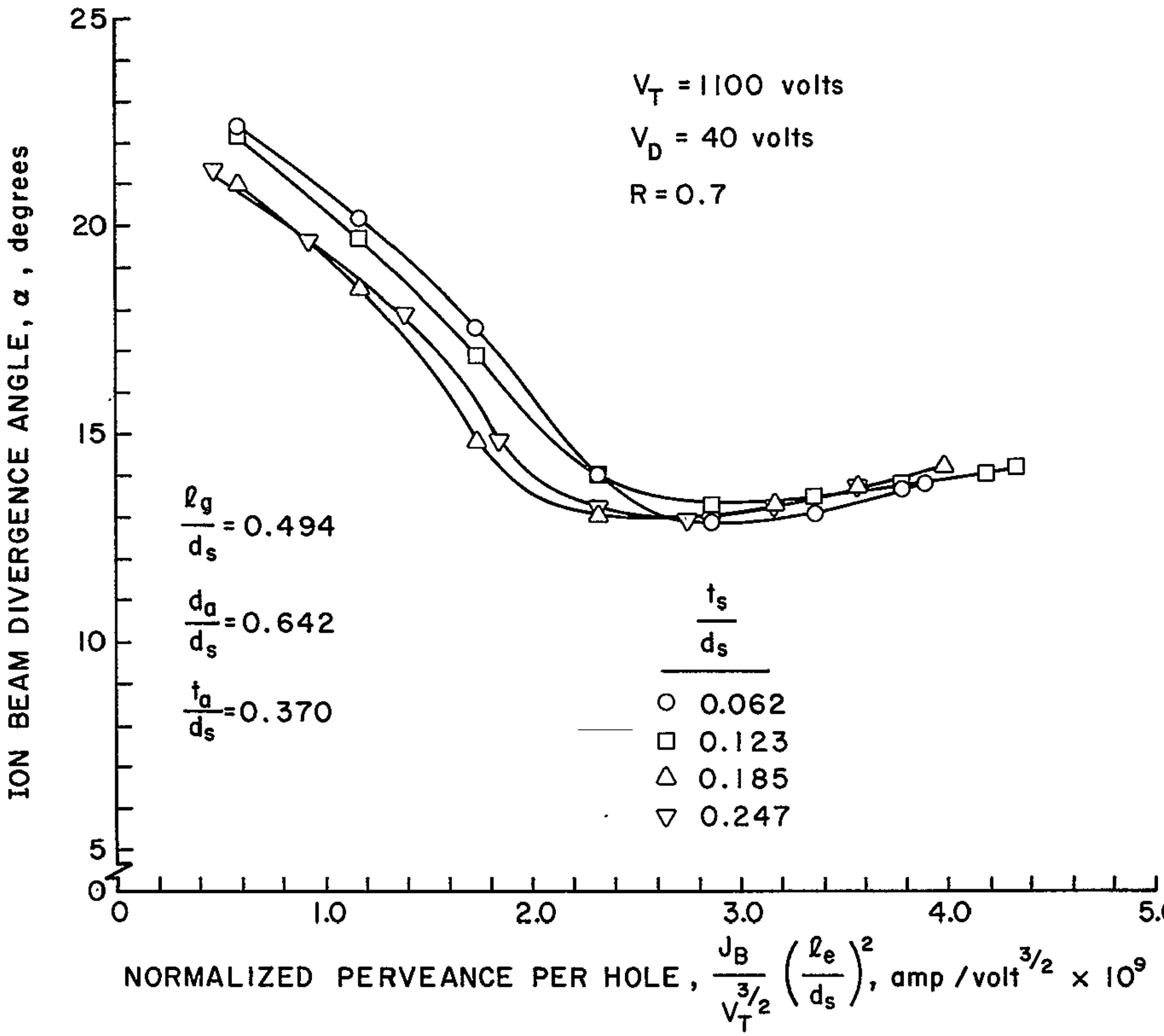

EFFECT OF SCREEN GRID THICKNESS RATIO
ON ARGON ION BEAM DIVERGENCE

FIGURE 10

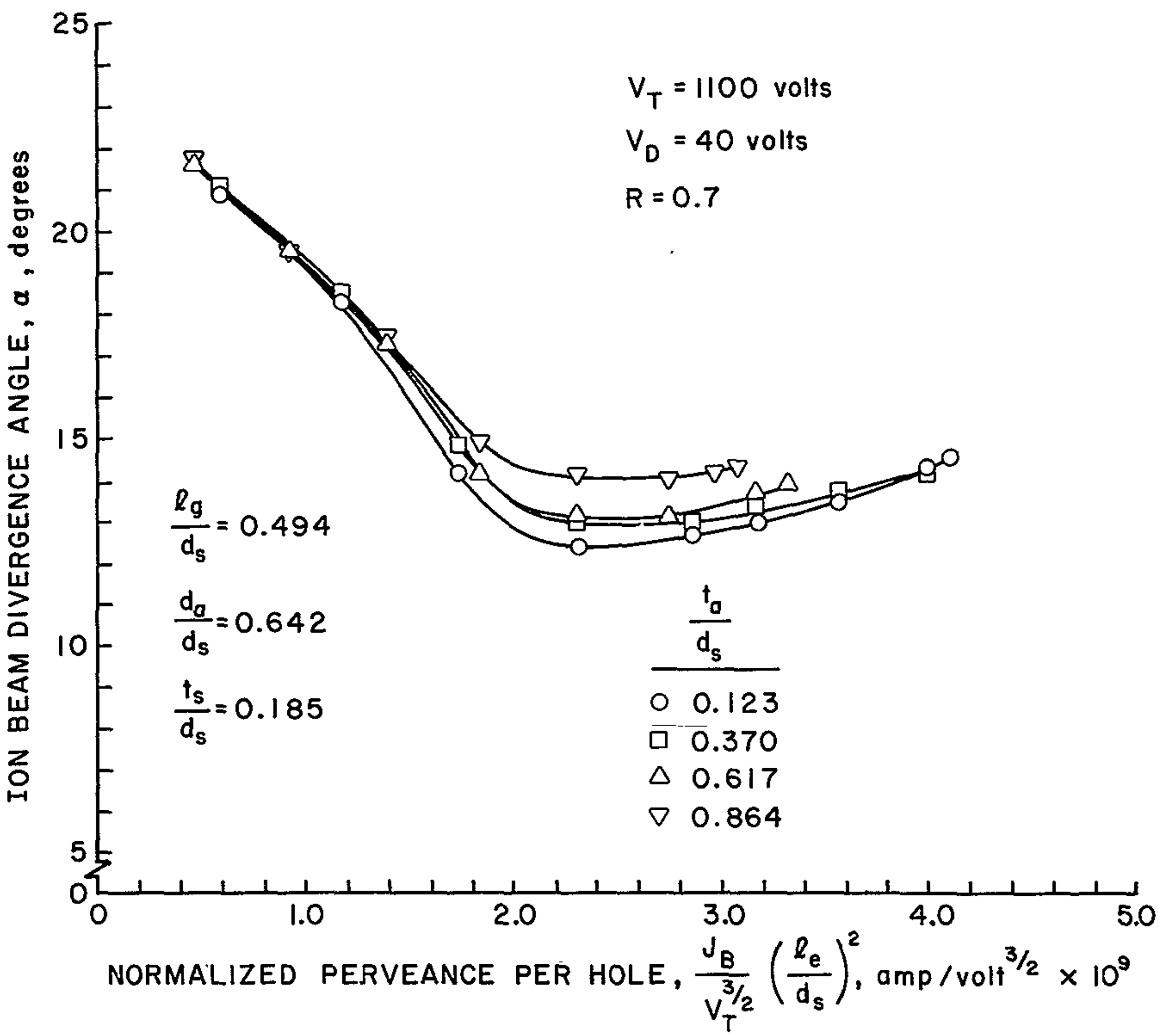

EFFECT OF ACCELERATOR GRID THICKNESS RATIO
ON ARGON ION BEAM DIVERGENCE

FIGURE 11

obtainable from the grid set (Fig. 9). The larger accelerator hole apparently allows the screen hole plasma sheath to penetrate further into the screen hole, with reduced ion focusing (Fig. 1(b)), before an excessive accelerator grid ion impingement current is reached. Larger accelerator holes result therefore in increased beam currents. Of particular interest in Fig. 9 are the results obtained with the smallest accelerator hole diameter ratio tested. Here the beam divergence angle goes through a maximum with increasing beam current. The accelerator grid impingement current observed with this grid set was large at the smallest beam current, went through a minimum as beam current was increased and then rose sharply as the maximum beam current was approached. These characteristics suggest ion trajectory cross-over may be occurring at low beam current levels.[14] If this is occurring the apparent decrease in divergence angle at very low normalized perveances could be caused by an increase in the number of ions leaving the screen hole sheath edge that are impinging directly upon the accelerator grid. In this case the accelerator grid would be acting as a beamlet mask for severe off-axis velocity ions at very small accelerator hole diameter ratios.

The different grid set geometries presented in Figs. 9 through 11 were investigated for the effects of net-to-total accelerating voltage ratio variations also. No significant changes in the shape of the ion beam divergence angle curves, found characteristic to each geometrical grid parameter, were apparent. Rather these curves were simply raised or lowered by a uniform amount, predictable from Figs. 5 through 8, as the net-to-total accelerating voltage ratio was varied.

In summary, Figs. 5 through 11 show that the geometrical grid parameters and net-to-total accelerating voltage ratio act fairly independently of one another in the effect each has on the ion beam divergence characteristics of two-grid accelerator systems. These effects can be summarized as follows:

(i) Ion beam divergence depends most strongly on grid separation ratio (ℓ_g/d_s) and net-to-total accelerating voltage ratio (R) changes.

(ii) The maximum normalized perveance per hole (or beam current) obtainable from a particular grid set depends most strongly on the accelerator hole diameter ratio (d_a/d_s).

(iii) Screen grid thickness ratio (t_s/d_s) and accelerator grid thickness ratio (t_a/d_s) variations result in consistant, but negligible, changes in ion beam divergence and the maximum normalized perveance per hole.

While these trends were obtained for a total accelerating voltage and discharge voltage of 1100 and 40 volts, respectively, the same trends have been reported previously for a total accelerating voltage and discharge voltages of 600 and 40 volts respectively. This indicates their general nature.

Figures 12 through 14 show the effect of total accelerating voltage and discharge voltage variations on ion beam divergence. For these data the net-to-total accelerating voltage ratio was kept at a constant value of 0.7 while the grid geometry parameters remained at the values $\frac{\ell_g}{d_s} = 0.741$, $\frac{d_a}{d_s} = 0.642$, $\frac{t_s}{d_s} = 0.185$ and $\frac{t_a}{d_s} = 0.370$. Increasing the total accelerating voltage (for a constant discharge voltage) or decreasing discharge voltage (for a constant total accelerating voltage) shifts each beam divergence curve to higher normalized perveance per hole values. For example, the normalized perveance per hole at which a beam divergence angle of 15° occurs is larger at V_T = 1500 volts than V_T = 600 volts (for constant discharge

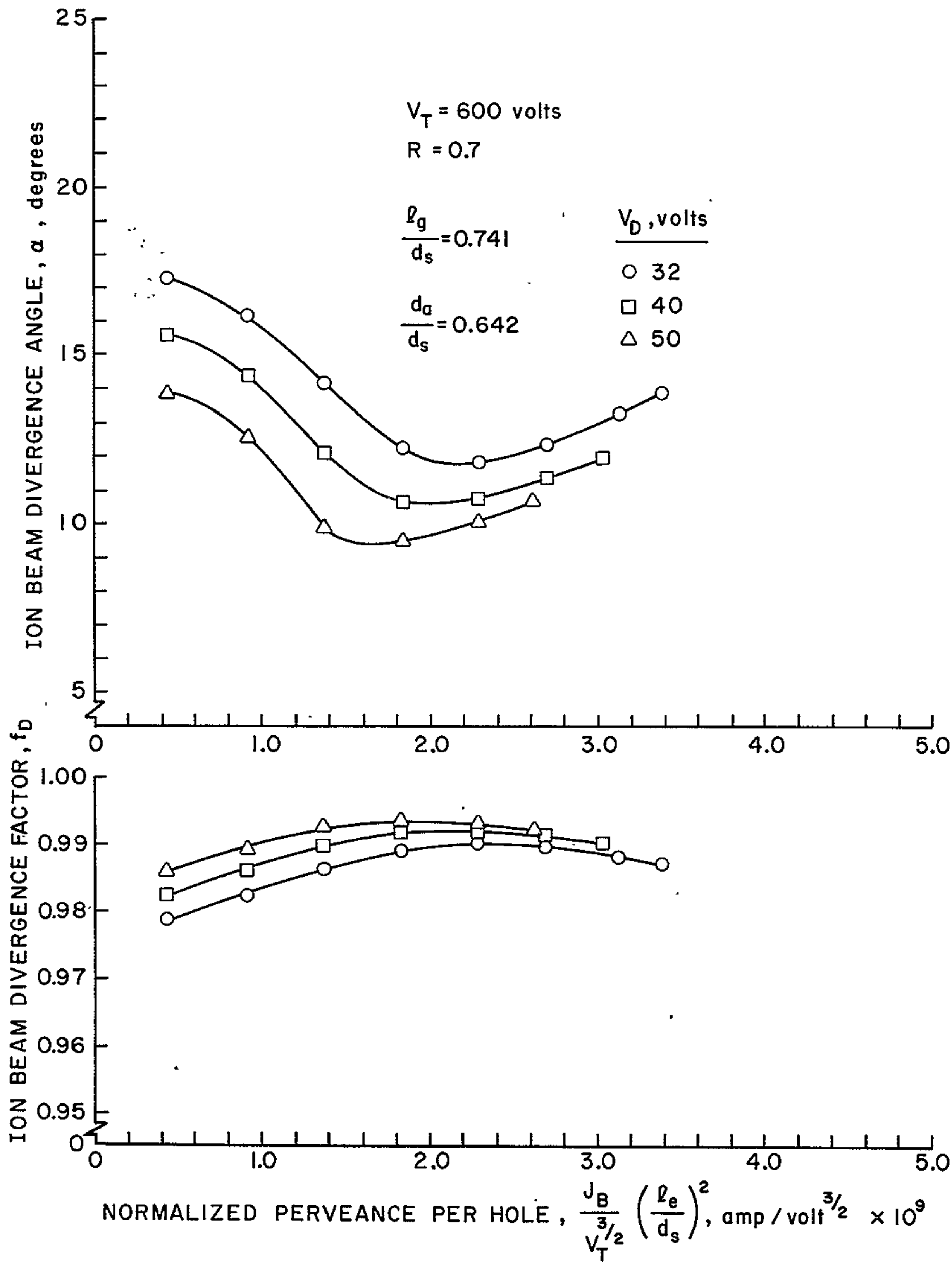

EFFECT OF DISCHARGE VOLTAGE ON ARGON ION BEAM DIVERGENCE
(Total accelerating voltage - 600 volts)

FIGURE 12

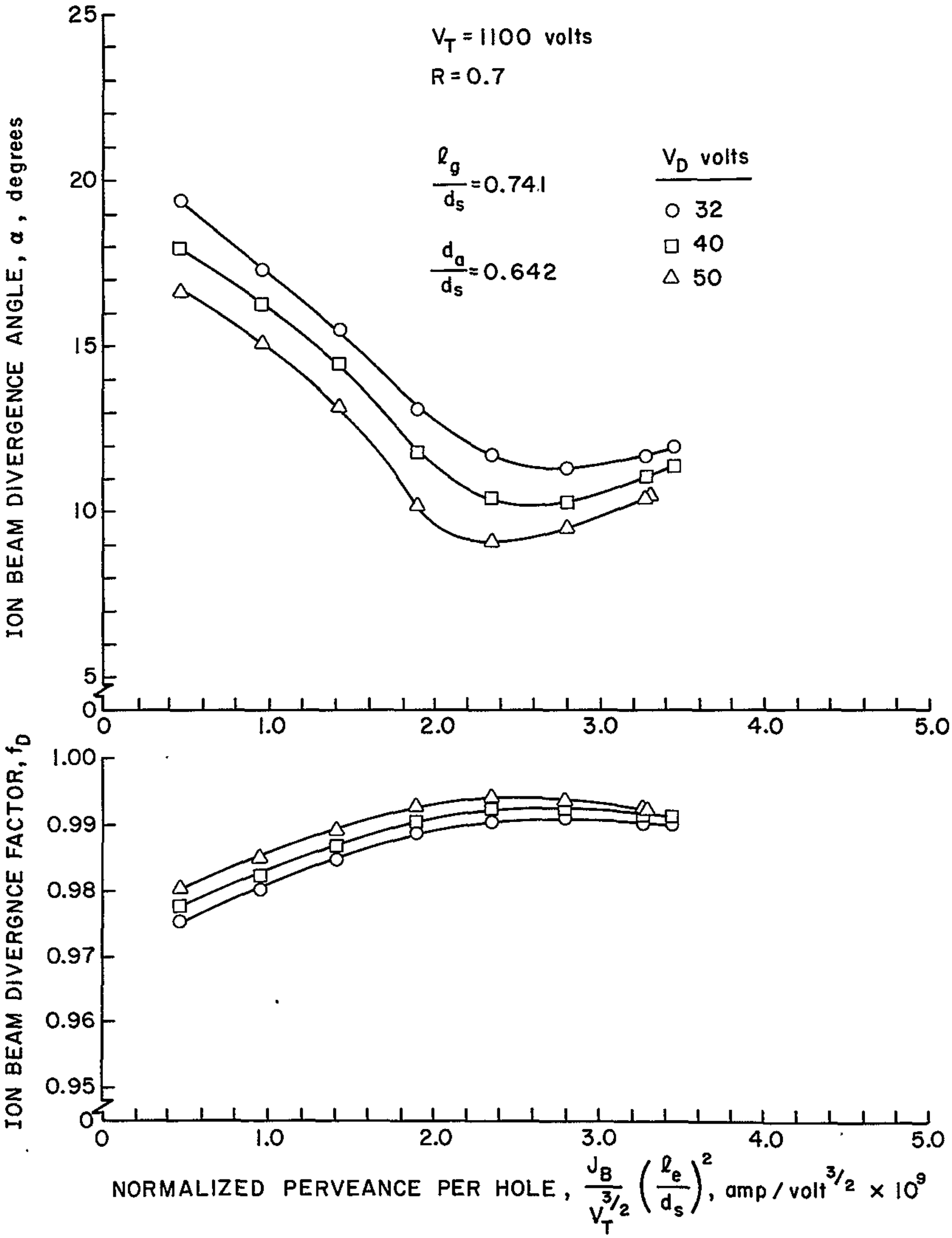

EFFECT OF DISCHARGE VOLTAGE ON ARGON ION BEAM DIVERGENCE
(Total accelerating voltage - 1100 volts)

FIGURE 13

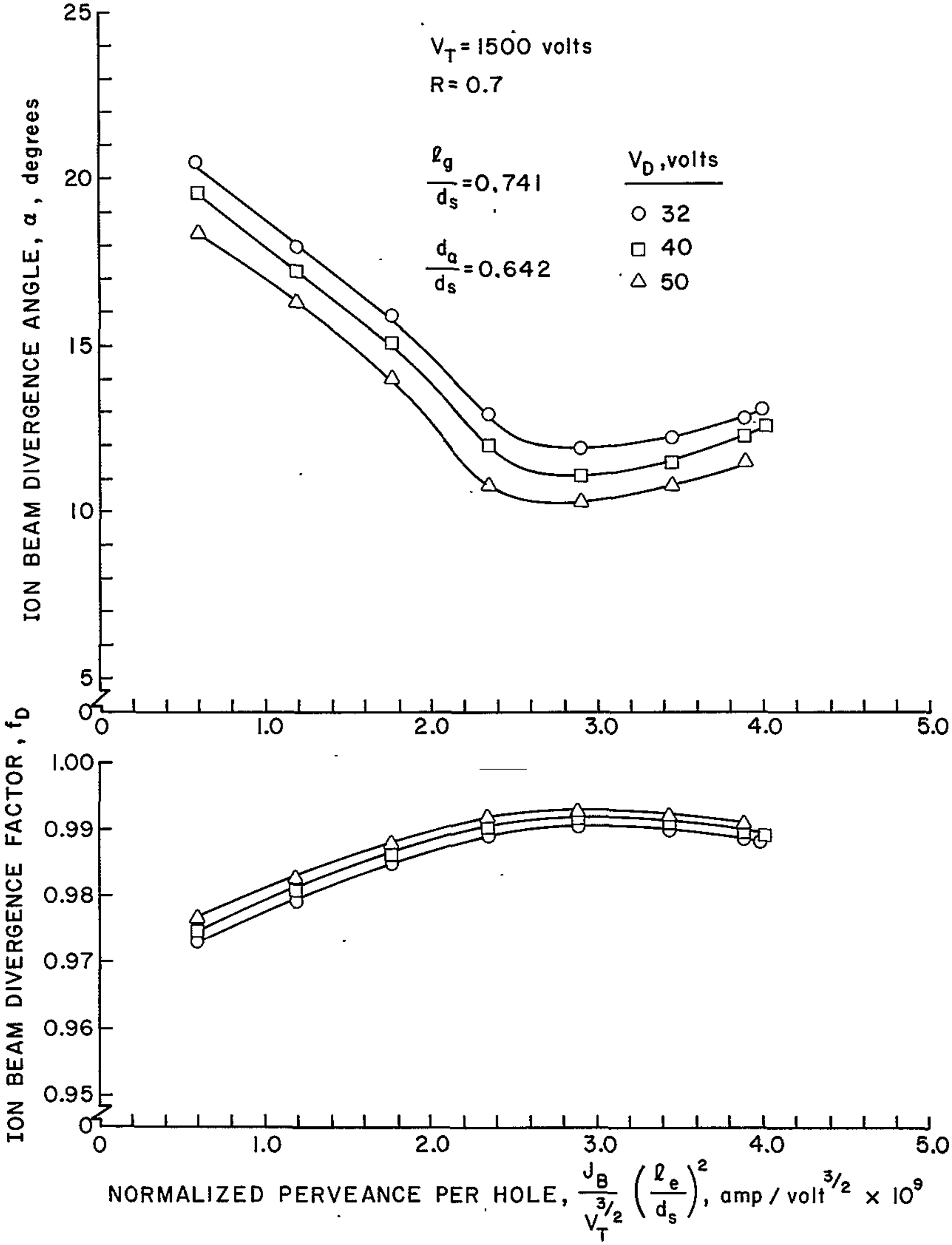

EFFECT OF DISCHARGE VOLTAGE ON ARGON ION BEAM DIVERGENCE
(Total accelerating voltage - 1500 volts)

FIGURE 14

voltage) and is larger also at V_D = 32 volts than V_D = 50 volts (for constant total accelerating voltage).

The changes in the minimum ion beam divergence angle are small, but there is a consistant trend towards increased beam divergence with increasing total accelerating voltage and decreasing discharge voltage. This effect is most pronounced for V_T = 600 volts (Fig. 12) where a 3° average beam divergence angle increase is observed for a discharge voltage decrease from 50 to 32 volts. For higher total accelerating voltages of 1100 and 1500 volts (Figs. 13 and 14) the angular spread caused by discharge voltage variations is less. The slight reduction in maximum normalized perveance per hole as V_D is decreased from 40 to 32 volts for total accelerating voltages of 1100 and 1500 volts (Figs. 13 and 14), is thought to be caused by a discharge power supply limitation when operating at these extreme conditions.

Variations in beam divergence with discharge voltage are not considered to be due to changes in doubly-charged ion densities because these densities should be negligible in this 8 cm argon thruster at discharge voltages below 50 v.[16] Rather discharge and total accelerating voltage variations are believed to alter the sheath shape and position. The manner in which these changes occur to produce the results shown in Figs. 12 through 14 however is still open to conjecture. It can be said though that these changes have less effect on the beam divergence characteristics of a particular grid geometry as the discharge-to-total accelerating voltage ratio is decreased. Figure 15 combines beam divergence data from four different total accelerating voltages using a constant 40 volt discharge. The geometrical grid parameters and net-to-total accelerating voltage ratio remained at the values indicated. Figure 15 shows the beam generally becomes less divergent as the discharge-to-total accelerating voltage ratio

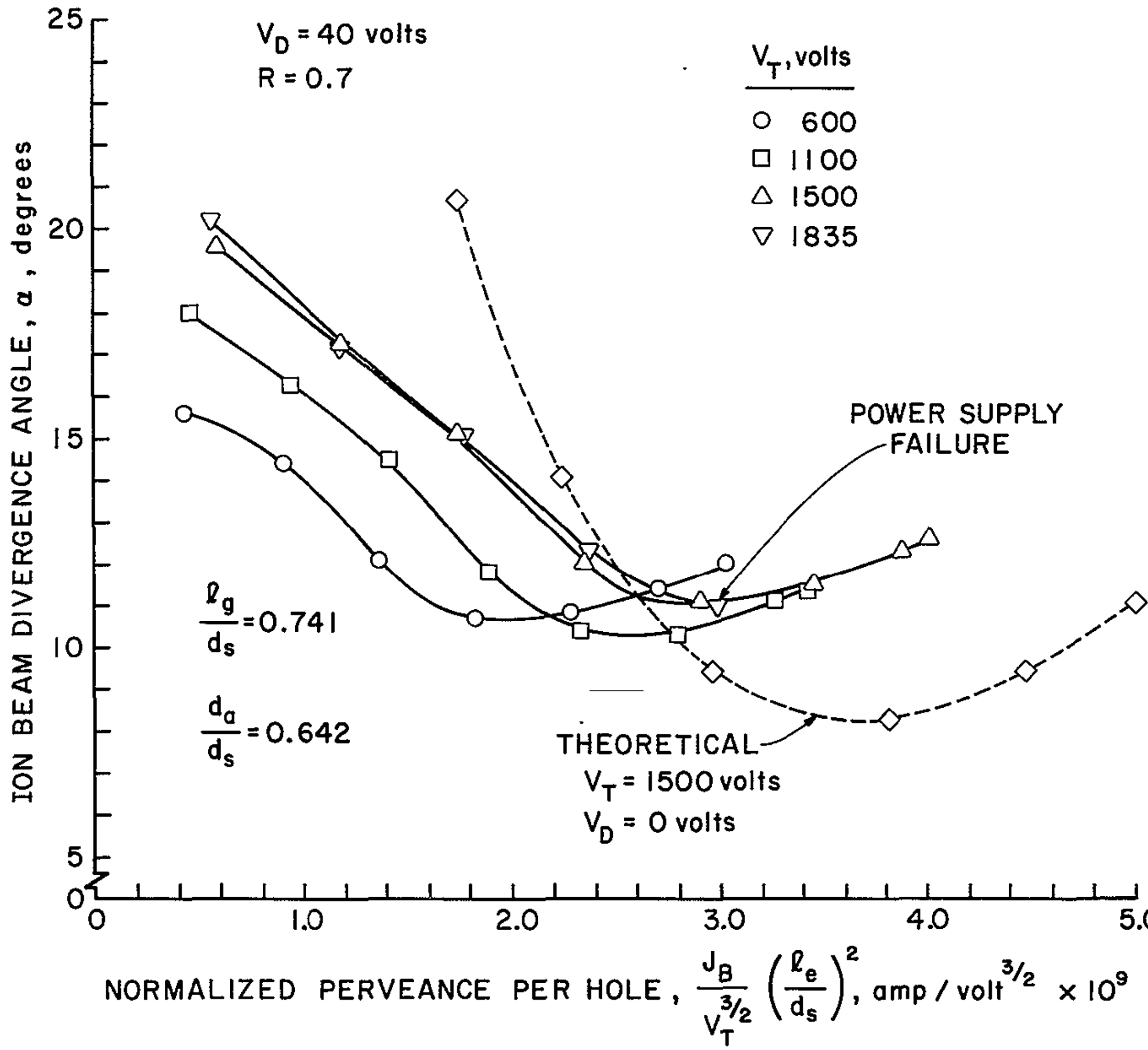

EFFECT OF TOTAL ACCELERATING VOLTAGE ON ARGON ION BEAM DIVERGENCE
(Discharge voltage - 40 volts)

FIGURE 15

is decreased. Increasing total accelerating voltage above about 1500 volts alters ion beam divergence by a negligible amount only. Theoretical results obtained by Kaufman[4] are shown also. These theoretical results were based on a zero discharge voltage and this is believed a major reason for their inability to model the experimental results adequately. Figure 15 indicates closer agreement between experiment and theory as the experimental discharge-to-total accelerating voltage ratio approaches zero.

The data contained in Figs. 12 through 15 show that neither total accelerating voltage nor discharge voltage alone adequately describe the beam divergence variations. From the observed opposite trends that increases in V_T and V_D produce, together with dimensional considerations, the ratio of these two parameters $\frac{V_D}{V_T}$, is believed to be the most important quantity to describe the overall effect. Other grid set geometries (different $\frac{\ell_g}{d_s}$ etc.) were also operated to determine the effect of discharge and total accelerating voltage variations on divergence characteristics. No differences in the voltage induced trends depicted in Figs. 12 through 15 were observed. The only differences apparent were related directly to the grid geometry changes. For instance, a uniform increase in ion beam divergence occurred after decreasing the grid separation ratio from 0.741 to 0.494, but the amount was predictable from the results shown in Figs. 6 and 7.

Correlated Results

In the previous section it was shown that ion beam divergence, from two-grid, multi-aperture accelerator systems, depends primarily on the grid separation ratio $\frac{\ell_g}{d_s}$, net-to-total accelerating voltage ratio R, and discharge voltage-to-total accelerating voltage ratio $\frac{V_D}{V_T}$. These three parameters have been used to correlate the ion beam divergence angle variation for all grid set geometries and accelerator system operating conditions examined during this study. Figure 16(a) shows the result of this correlation. Here the simple Child's Law normalized perveance per hole expression has been modified to include the effect of discharge-to-total accelerating voltage ratio variations. The ion beam divergence angle correlation is seen to lie within a band $\pm$ 1½° (actual degrees) of the indicated line of best fit. The parameter $NP/H_{\alpha_{min}}$ occurring in the beam divergence angle correlation refers to the normalized perveance per hole at the minimum beam divergence angle. It is plotted as a function of the discharge voltage-to-total accelerating voltage ratio $\frac{V_D}{V_T}$, and shown in Fig. 16(b). It was necessary to introduce normalized perveance per hole as a parameter in the ion beam divergence angle correlation because of the decreased effect net-to-total accelerating voltage ratio variations have on ion beam divergence angle at low normalized perveance per hole values (Figs. 5 through 8.). Figures 16(a) and 16(b) allow ion beam divergence angles to be determined for a wide variety of grid geometry and accelerator system operating conditions. However, as mentioned previously, there is an absolute beam current limit, related directly to the accelerator hole diameter ratio, for each grid set geometry. This limit is shown graphically in Fig. 16(c). Figure 16(c) may be interpreted as describing the beamlet diameter ratio at the accelerator hole entrance as a function of the correlated normalized perveance per hole, because the beamlet diameter is approximately equal to the accelerator hole diameter at the maximum normalized perveance per hole (or beam current) condition.

Figures 16(a), 16(b), and 16(c) should be used in the following way. First, the values of J_B, $\frac{\ell_e}{d_s}$, V_D, V_T and R must be known. The value of

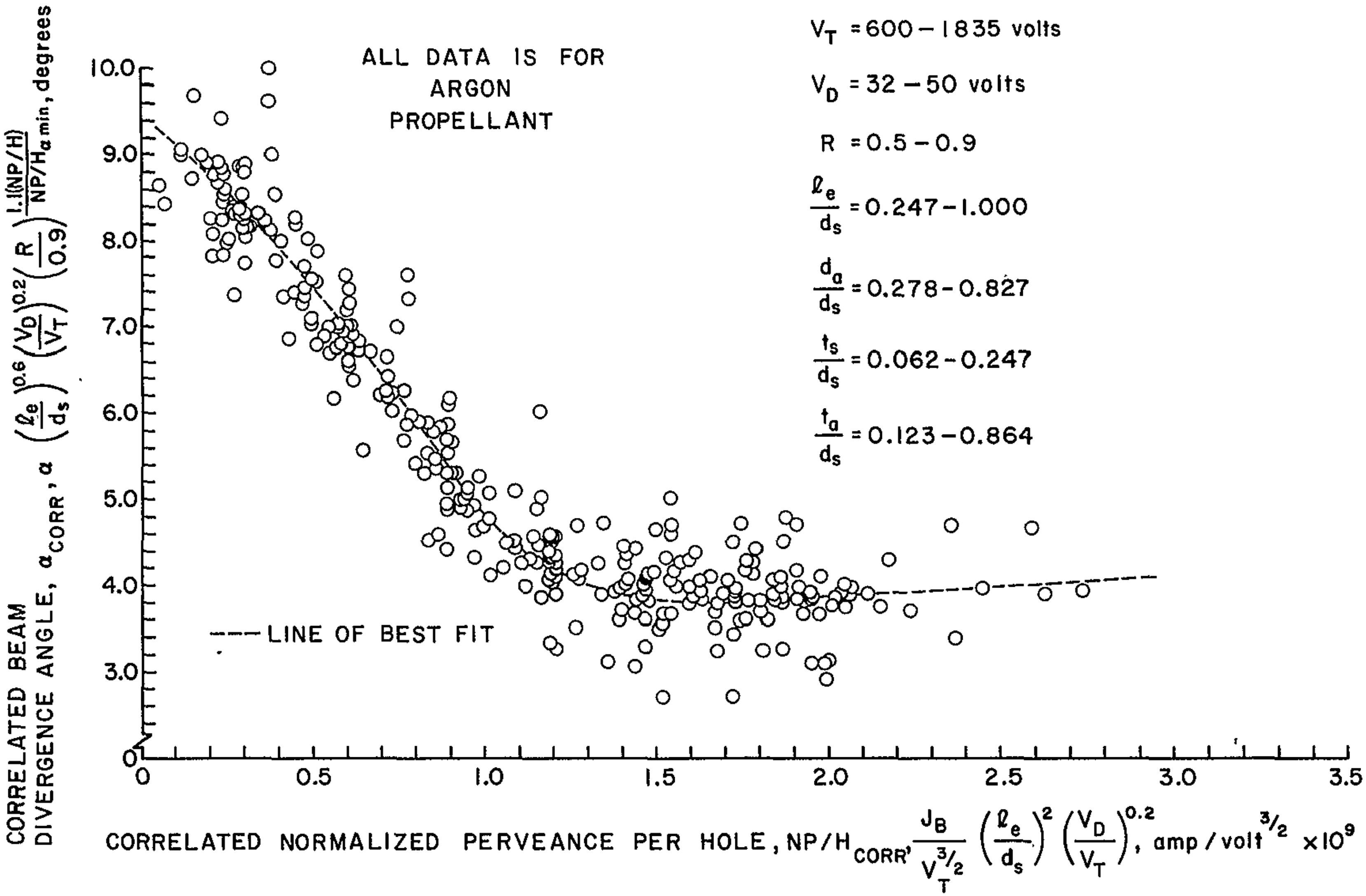

FIGURE 16a

ARGON ION BEAM DIVERGENCE ANGLE CORRELATION

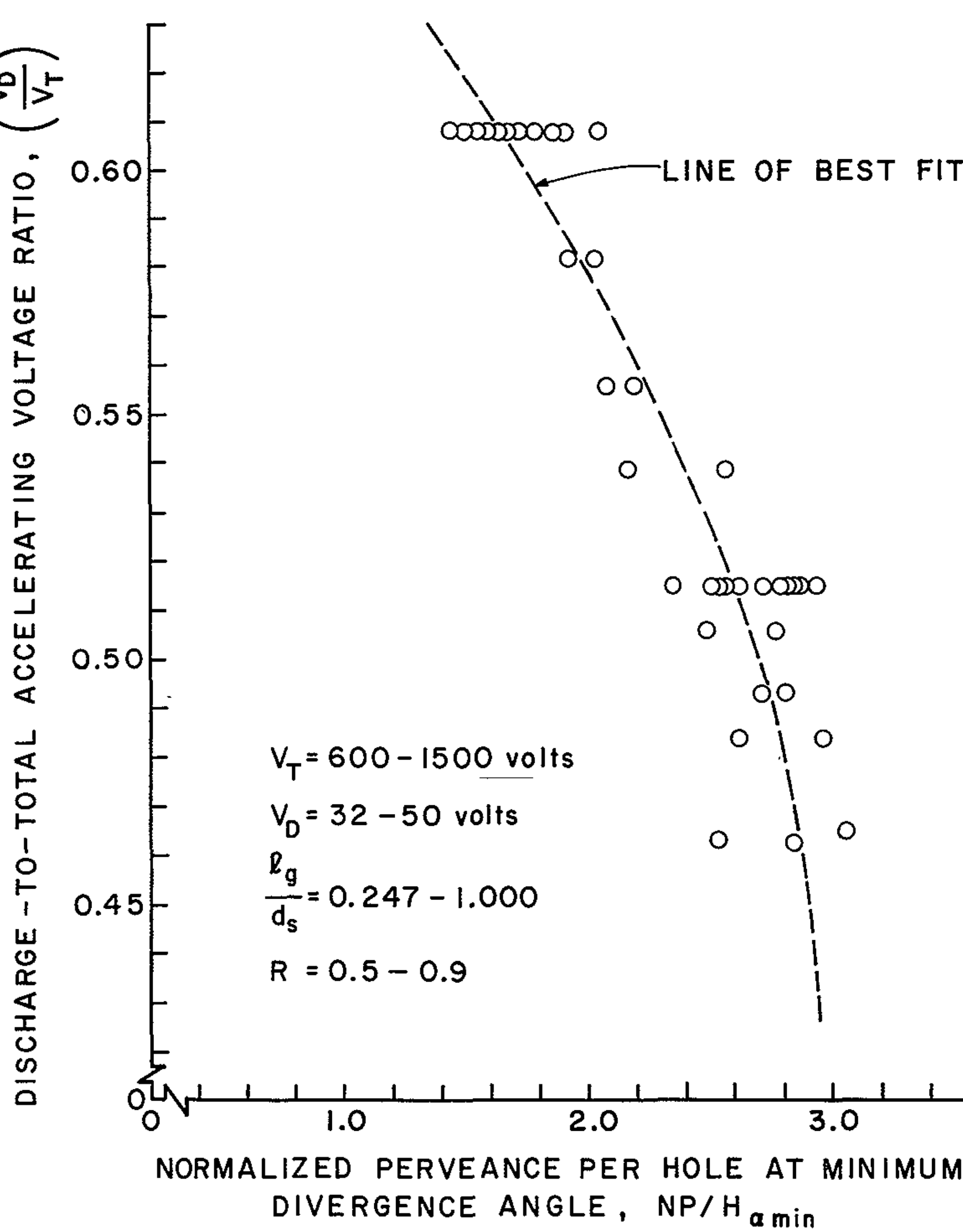

VARIATION IN ARGON NORMALIZED PERVEANCE PER HOLE AT MINIMUM DIVERGENCE $NP/H_{\alpha min}$
WITH DISCHARGE-TO-TOTAL ACCELERATING VOLTAGE RATIO

FIGURE 16b

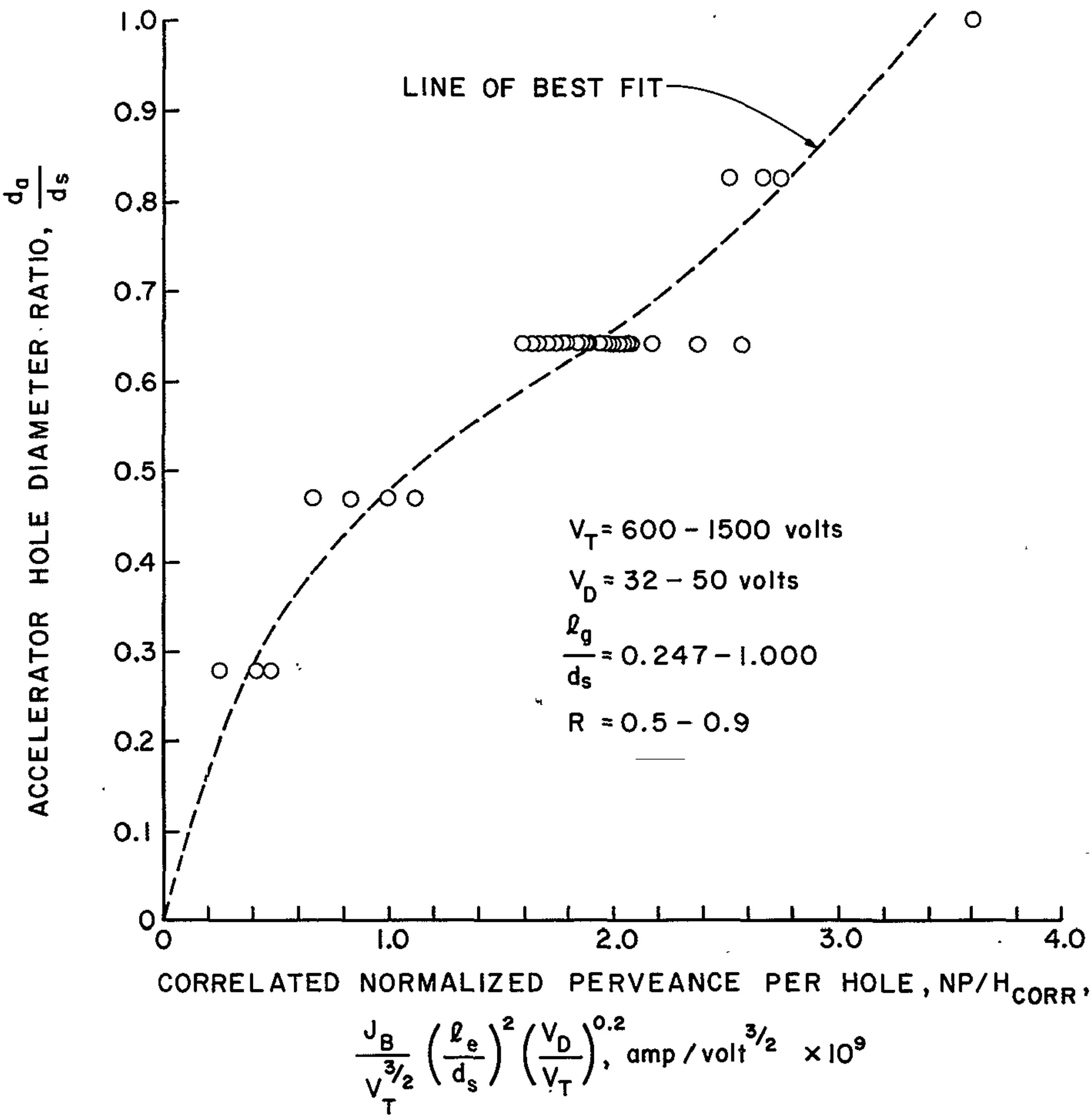

MAXIMUM ARGON NORMALIZED PERVEANCE PER HOLE
VS ACCELERATOR HOLE DIAMETER RATIO

FIGURE 16c

NP/H_{corr} is then calculated and used to obtain the value of α_{corr} from Fig. 16(a). The value of $NP/H_{\alpha_{min}}$ is found from Fig. 16(b) and used to calculate the actual beam divergence angle from the previously found value of α_{corr}. Finally, Fig. 16(c) should be used to determine the minimum value of d_a to attain the desired beam current. To avoid excessive accelerator grid ion impingement this minimum d_a value should be increased by about twenty percent. If accelerator system operation over a range of beam currents is proposed, Fig. 16(c) should be used to determine the value of d_a (by the method outlined above) necessary to attain the maximum beam current desired. The procedure outlined previously will then establish the range of divergence angles to be expected for the beam current operating range.

Figure 17 shows the minimum ion beam divergence angle that can be obtained as a function of grid separation ratio and net-to-total accelerating voltage ratio. A straight line was chosen as a conservative fit to the extrapolated regions which are considered to be good for a first approximation of the minimum beam divergence angle when operating at these extreme conditions. The data shown in Fig. 17 is most accurate for the discharge voltage and total accelerating voltage indicated. However, previous results (Fig. 12 through 15) have shown that varying V_D and V_T either side of 40 and 1100 volts respectively, produced a variation of $\pm 1\frac{1}{2}°$ only in the minimum beam divergence angles given in Fig. 17. Hence Fig. 17 may be used to obtain fairly representative minimum beam divergence angle trends for a wide range of discharge-to-total accelerating voltage ratios.

Screen Hole Size and Propellant Variations

Figures 18 and 19 show the results of varying the two parameters held constant throughout this study, screen hole size and propellant gas.

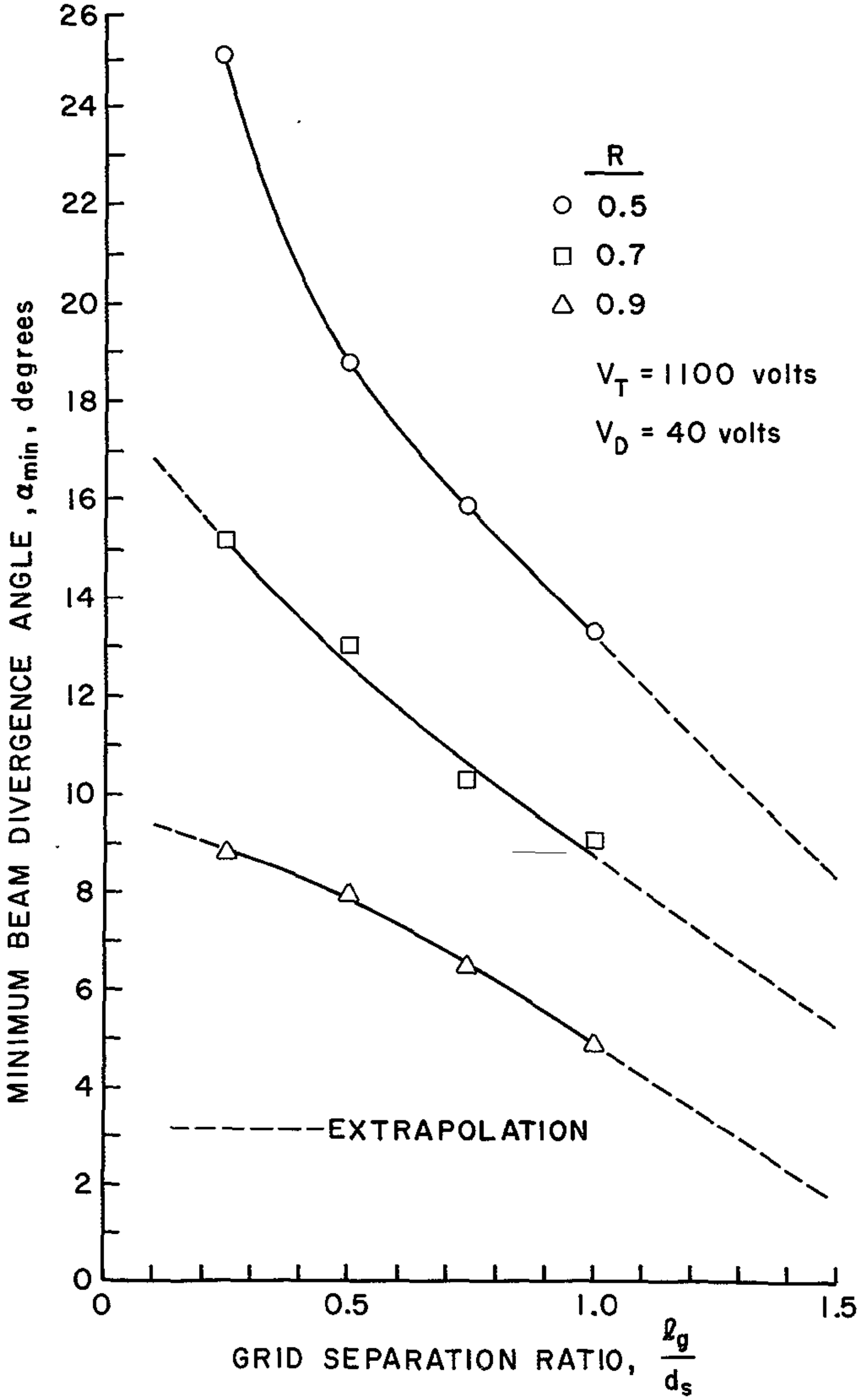

MINIMUM ARGON ION BEAM DIVERGENCE ANGLE VS GRID SEPERATION RATIO
AND NET-TO-TOTAL ACCELERATING VOLTAGE RATIO

FIGURE 17

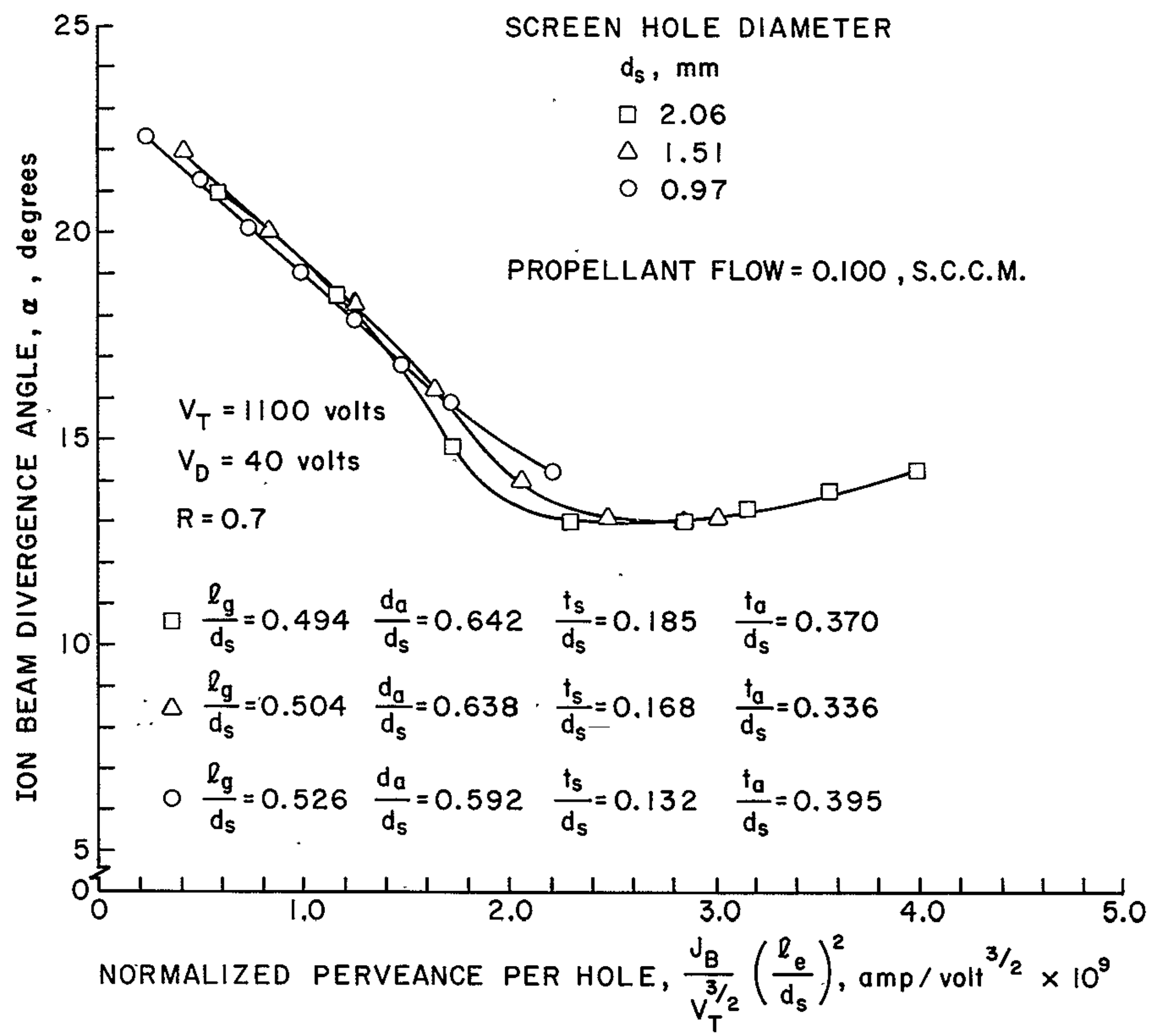

EFFECT OF SCREEN HOLE DIAMETER ON ARGON ION BEAM DIVERGENCE
(similar non-dimensionalized geometrical grid set parameters)

FIGURE 18

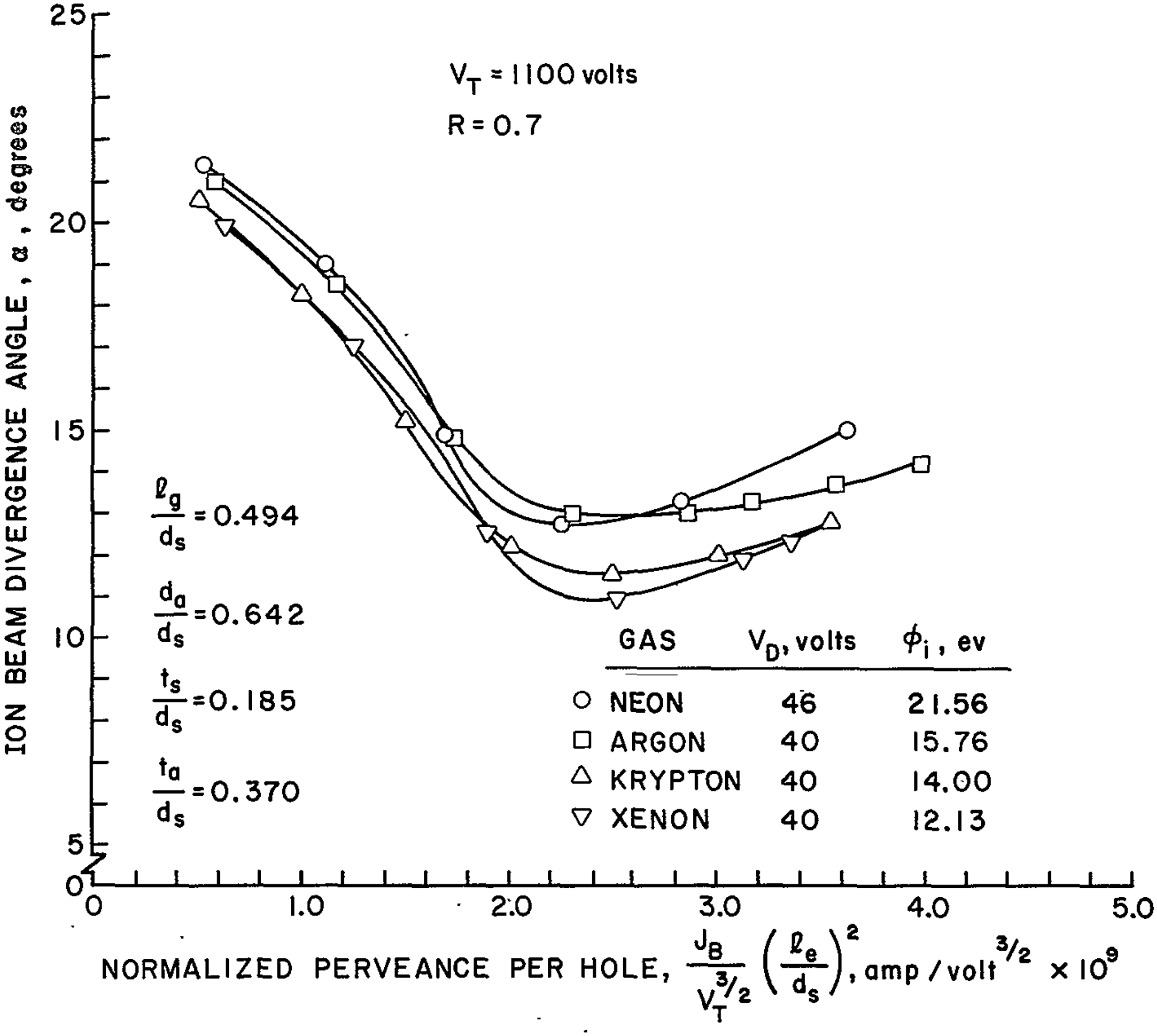

EFFECT OF PROPELLANT GAS ON ION BEAM DIVERGENCE

FIGURE 19

A constant grid aperture array size, similar non-dimensionalized grid geometry parameters and the same argon propellant mass flow rate were used for each screen hole size. Similar discharge chamber neutral number densities with the same grid system geometry were used for the different propellants (an exception was neon which required twice the neutral number density of the other gases, a 46 volt discharge and a discharge chamber magnetic field reduction before a stable discharge plasma could be maintained). Normalized perveance per hole for the different propellants shown in Fig. 19 was corrected to correspond to operation with argon. This was done by multiplying each calculated normalized perveance per hole value (Equation 3) by the square root of the ratio of the propellant atomic weight to the atomic weight of argon, $(\text{at. wt. prop./at. wt. argon})^{\frac{1}{2}}$. The reduction in maximum normalized perveance per hole with decreasing screen hole size has been observed previously with two-grid electron-bombardment ion thrusters.[14] The present data verifies those observations but does not shed new light onto the cause of the effect.

Figure 19 shows the parameter, normalized perveance per hole, correlates successfully the ion beam divergence variation over a range of propellant atomic weight and ionization potential. Figures 18 and 19 show that screen hole size and propellant gas changes do not alter substantially the beam divergence variation found characteristic of a particular grid set. Therefore, the data and correlation parameters presented in this report, while being most accurate for argon, are considered to hold generally for other propellants and screen hole sizes also. For instance, if knowledge of the ion beam divergence characteristics of a particular grid geometry operating with mercury rather than argon propellant are desired, then the following procedure should be used. From Equation (3) the normalized perveance per hole is calculated for the grid set operating condition of interest. This calculated normalized perveance per hole value is multiplied by the square root of the ratio of the atomic weight of mercury to the atomic weight of argon, $(\text{at. wt. mercury}/\text{at. wt. argon})^{\frac{1}{2}} = 2.241$. Now, having corrected the original value of normalized perveance per hole for mercury operation to a normalized perveance per hole value for use with argon, the figures and correlation parameters presented in this report may be used.

Conclusions

A comprehensive experimental investigation of two-grid accelerator systems has been conducted. A wide range of geometrical grid parameters and grid set operating conditions were investigated for their effect on ion beam divergence. Ion beam divergence was found to depend most strongly on grid separation ratio, net-to-total accelerating voltage ratio and discharge-to-total accelerating voltage ratio variations. The maximum normalized perveance per hole (and hence beam current) obtainable from a particular grid set, at a constant discharge-to-total accelerating voltage ratio, was found to depend most strongly on the accelerator hole diameter ratio. Variations to the other geometrical grid parameters have a negligible effect on ion beam divergence. Graphical results were obtained which permit performance predictions in new accelerator system designs. A general divergence angle correlation was developed to permit approximate divergence estimates of present designs. All results contained in this paper are considered of sufficient reliability to allow interpolation between specific experimental results and the use of limited range extrapolations. Although argon was the main test gas used in this study, the results are applicable to other propellants when the correction to normalized perveance per hole has been made (see pages 39-40).

ION BEAM DIVERGENCE CHARACTERISTICS OF THREE-GRID ACCELERATOR SYSTEMS

Graeme Aston

The addition of a third (decelerator) grid to the conventional two-grid accelerator system is known to reduce ion beam divergence.[17] The decelerator electrode is maintained at, or close to, facility ground potential and positioned downstream of the accelerator grid. This fixes the neutralization surface at the decelerator grid potential, resulting in flatter equipotential surfaces between the neutralization plane and accelerator hole than with a two-grid accelerator system. Flatter equipotential surfaces in the ion deceleration region cause less off-axis deflection of the emerging ions. This results in decreased ion beam divergence over that obtained by using a two-grid accelerator system.

The purpose of this study has been to determine those geometrical and operating conditions which affect most strongly the ion beam divergence of three-grid accelerator systems. The two-grid accelerator system studies in the preceding section have shown that screen and accelerator grid thickness and hole diameter changes affect ion trajectories in the ion deceleration region only slightly. Hence, decelerator grid location and geometry and accelerator system operating conditions have been the parameters investigated most thoroughly in this report.

Parameter Definitions

Figure 20 shows a portion of a multiaperture three-grid accelerator system indicating the geometrical parameters used. In the data presented hereafter these parameters will have the following values unless specified otherwise:

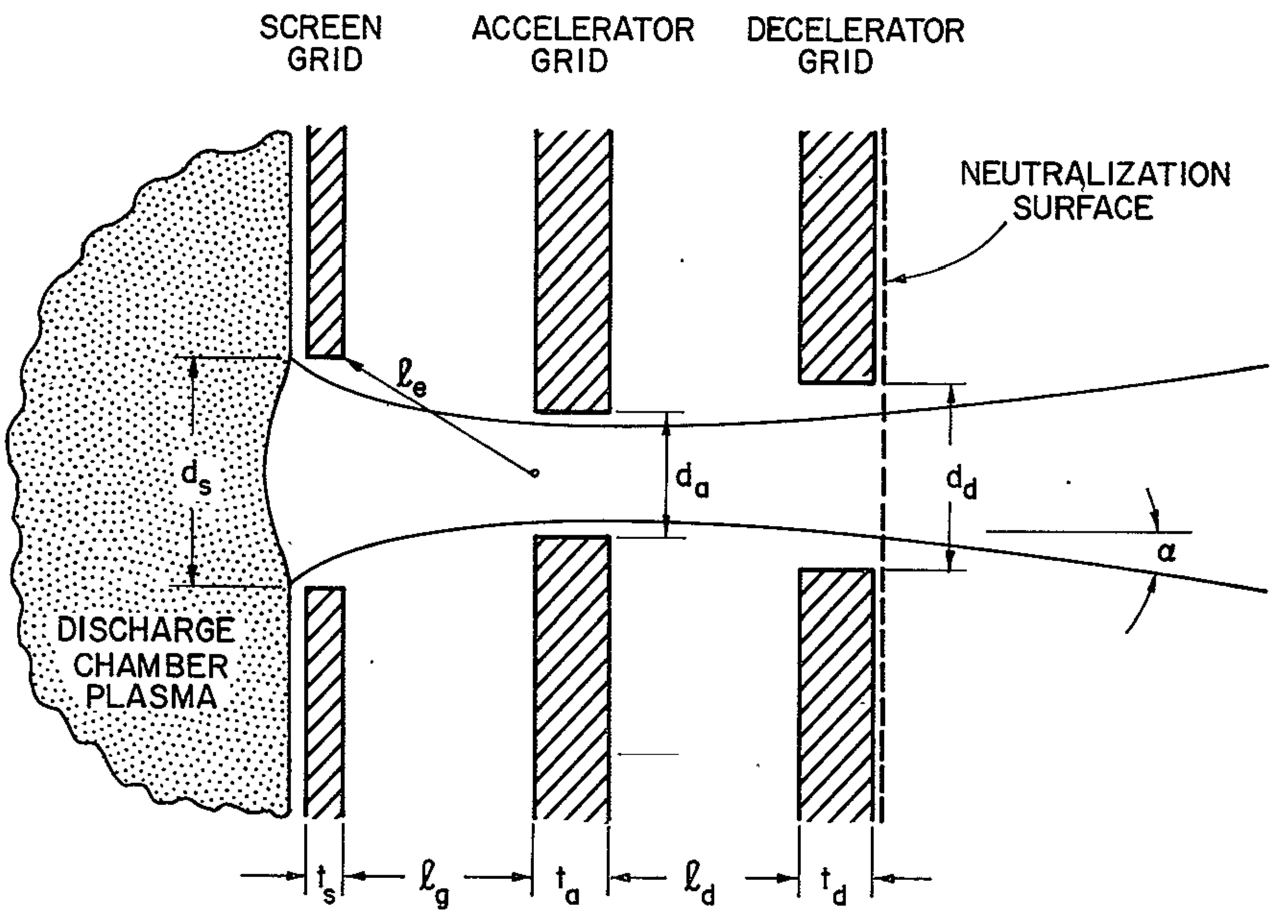

THREE-GRID SYSTEM

FIGURE 20

(i) Screen hole diameter, d_s = 2.06 mm,

(ii) Screen grid thickness ratio, t_s/d_s = 0.185,

(iii) Accelerator grid thickness ratio, t_a/d_s = 0.370,

(iv) Decelerator grid thickness ratio, t_d/d_s = 0.370,

(v) Accelerator hole diameter ratio, d_a/d_s = 0.642,

(vi) Decelerator hole diameter ratio, d_d/d_s = 0.827,

(vii) Total accelerating voltage, V_T = 1100 volts,

(viii) Discharge voltage, V_D = 40 volts,

Perveance is based on the argon propellant ion mass because argon was used in the tests. Results are considered correct for other propellant atoms if perveance values are multiplied by the square root of the ratio of argon atomic mass number (40) to that of the propellant to be used. To modify the data of this section for use with mercury propellant for example perveance values given on the axis of the graphs would be multiplied by $\sqrt{40/200}$ = 0.447. Perveance and other parameters used in this section are calculated as discussed in the preceding section of this report.

Apparatus and Procedure

The apparatus and procedure used for this study were identical to that which has been discussed in the preceding section of this report except for the addition of the decelerator grid. A twelve volt negative bias was placed on this grid to prevent neutralization electrons from reaching its surface. Both accelerator and decelerator grid impingement currents were monitored for each grid set operating condition. The precision with which the ion beam divergence data were obtained is $\pm$ 0.5° for the ion beam divergence angle α, and $\pm$ 0.001 for the ion beam divergence factor f_D. The absolute accuracy of the data is thought to be better than $\pm$ 1° for α, and better than $\pm$ 0.002 for f_D.

Results and Discussion

Figures 21 through 24 show the beam divergence characteristics of a high perveance grid set (close screen-to-accelerator grid separation ratio $\frac{\ell_g}{d_s}$) as the accelerator-to-decelerator grid separation ratio $\frac{\ell_d}{d_s}$ and net-to-total accelerating voltage ratio R are varied over the range of interest. Either increasing the net-to-total accelerating voltage ratio or decreasing the accelerator-to-decelerator grid separation ratio is observed to decrease ion beam divergence. The ion beam divergence becomes less sensitive to these parameters as the net-to-total accelerating voltage ratio approaches unity. Figures 21 and 22 show that reducing the accelerator-to-decelerator grid separation ratio by a factor of two from 0.247 to 0.123 does little to lower the minimum beam divergence angle. This indicates that a limiting beam divergence angle minimum is approached which seems unaffected by further accelerator-to-decelerator grid separation ratio reductions beyond a $\frac{\ell_d}{d_s}$ value of 0.2 (for this particular grid set).

The beam divergence angle reductions at low normalized perveance seen in Figs. 21 through 24, result from direct ion impingement upon the decelerator grid--a condition that results in decel grid erosion and probably makes operation at low perveance impractical. This reduction in divergence angle at low perveance appears to occur because the beamlet ions impinging upon the decelerator grid at low beam current levels are those which have the greatest off-axis velocity components. By intercepting these ions the decelerator grid acts as a beamlet mask which reduces the beam divergence angle at low beam current levels. Evidence of the high decelerator impingement at low perveance is shown in Figure 25. Here accelerator and decelerator

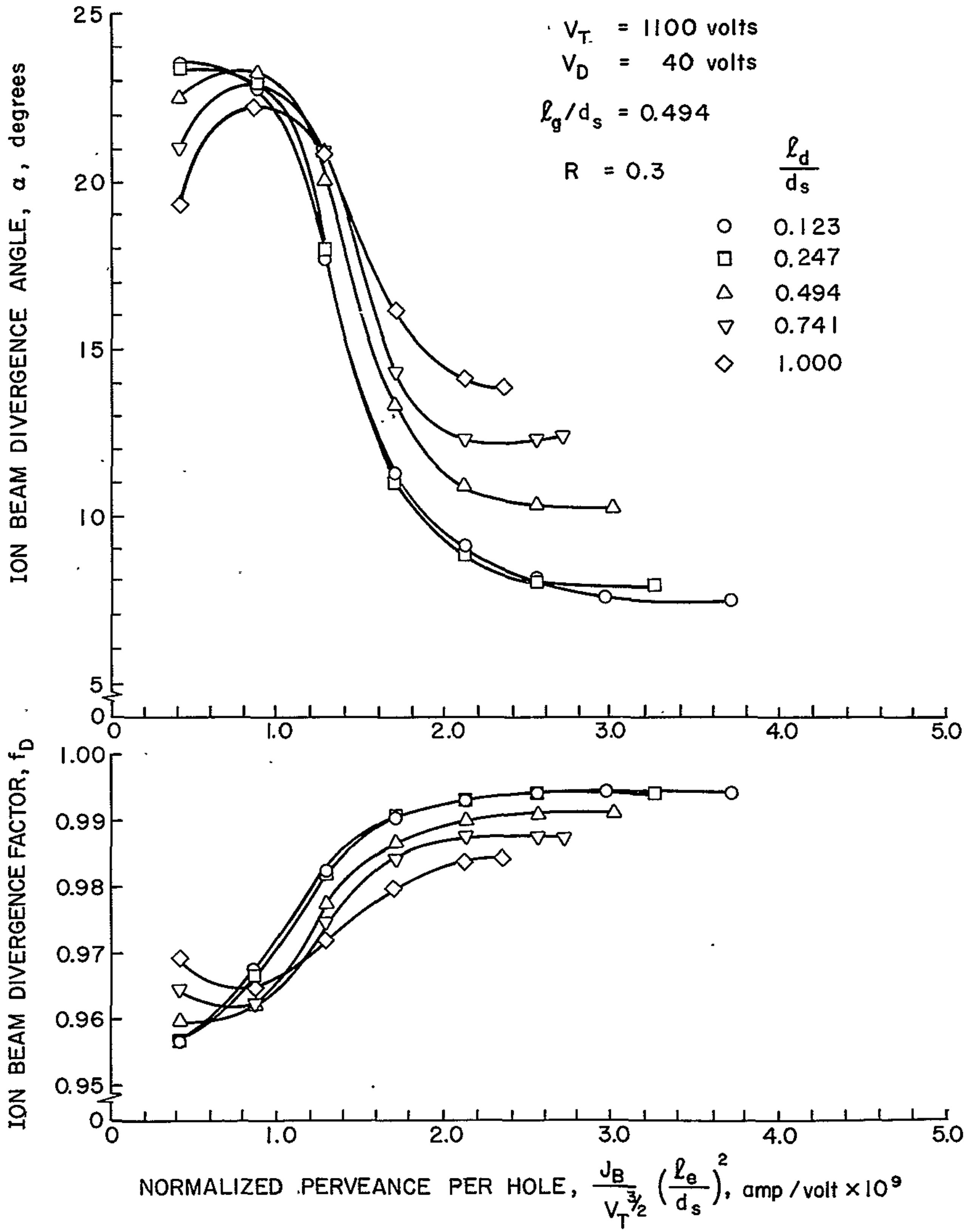

EFFECT OF DECELERATOR GAP RATIO ON DIVERGENCE
R = 0.3, ARGON

FIGURE 21

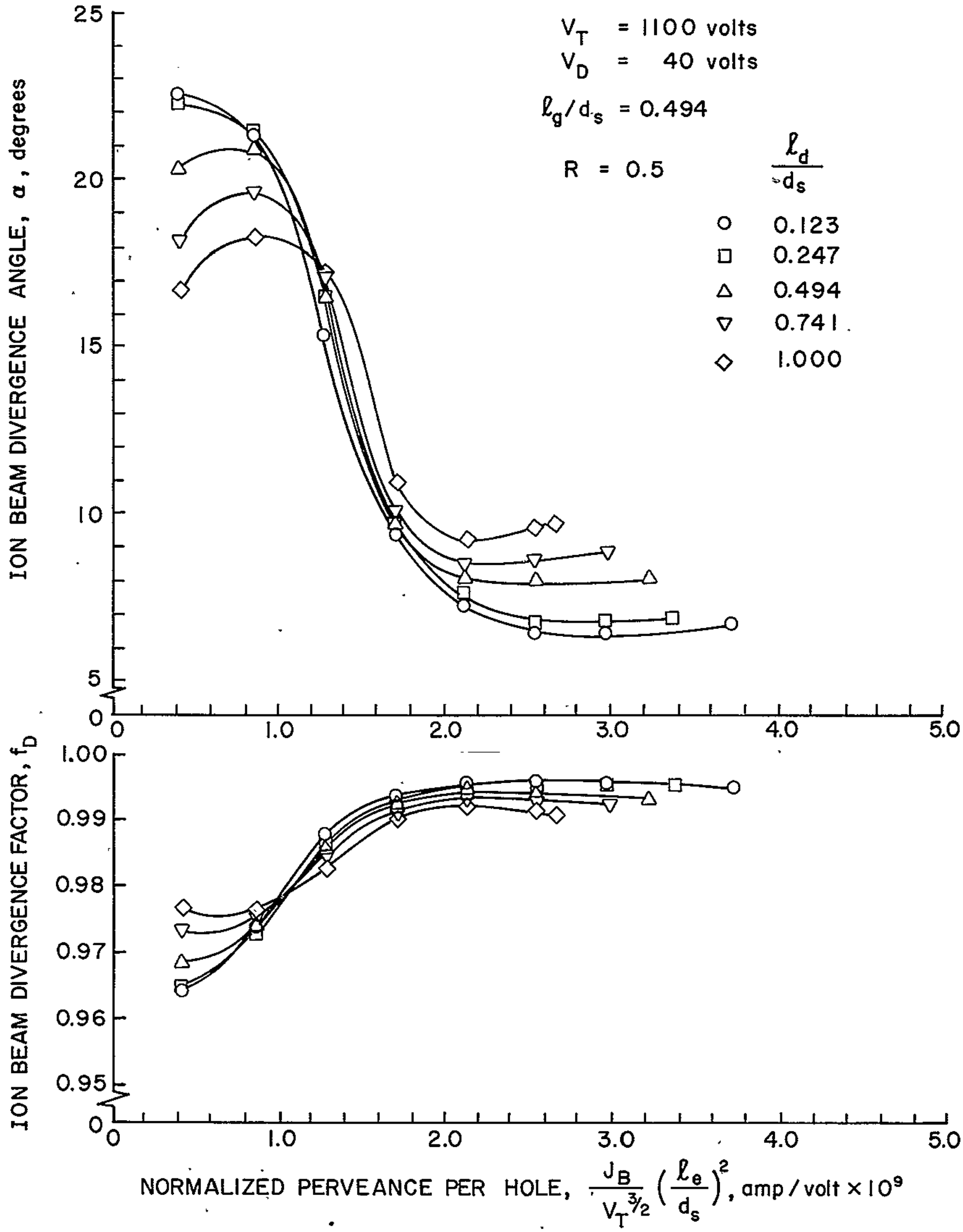

EFFECT OF DECELERATOR GAP RATIO ON DIVERGENCE
R = 0.5, ARGON

FIGURE 22

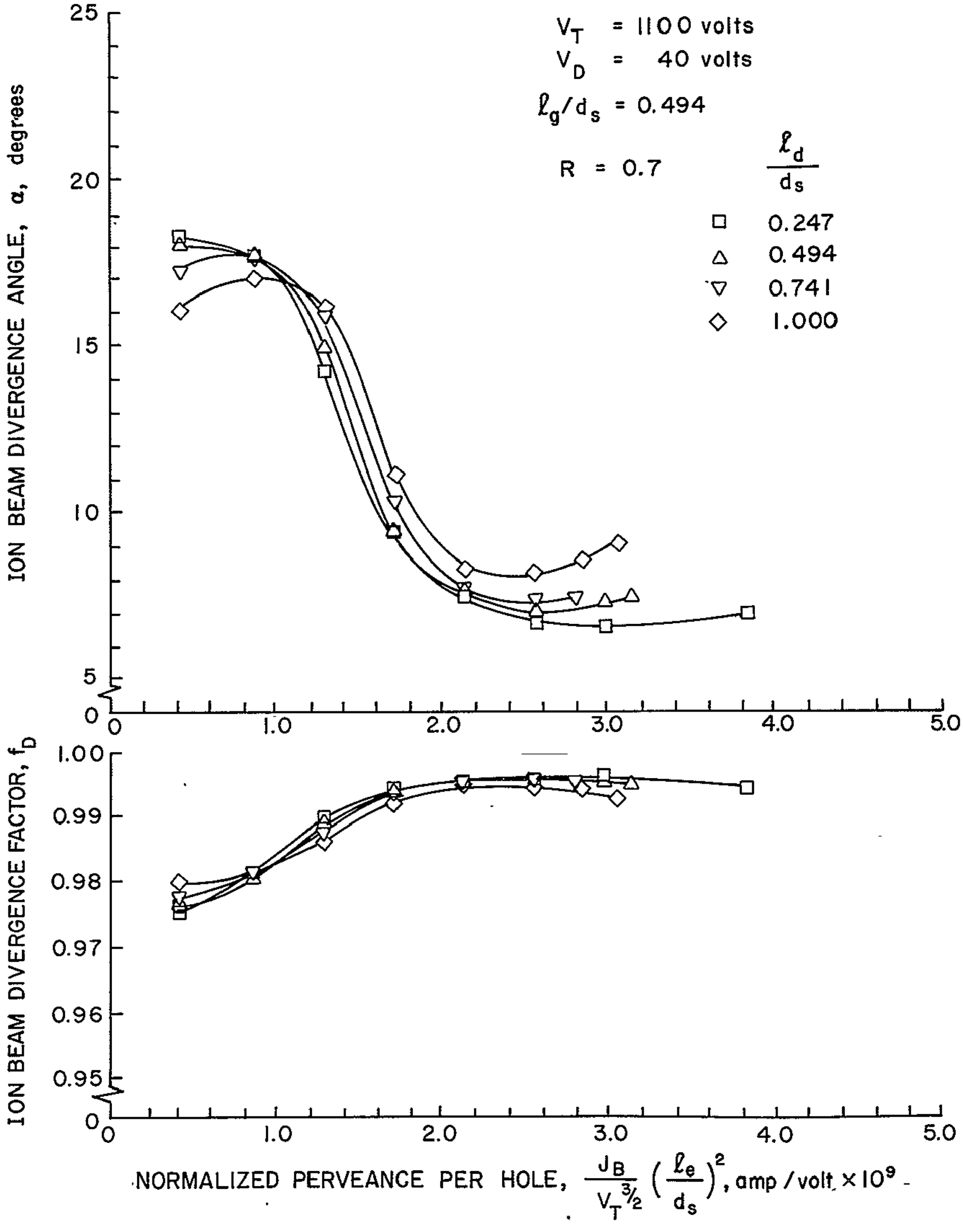

EFFECT OF DECELERATOR GAP RATIO ON DIVERGENCE
R = 0.7, ARGON

FIGURE 23

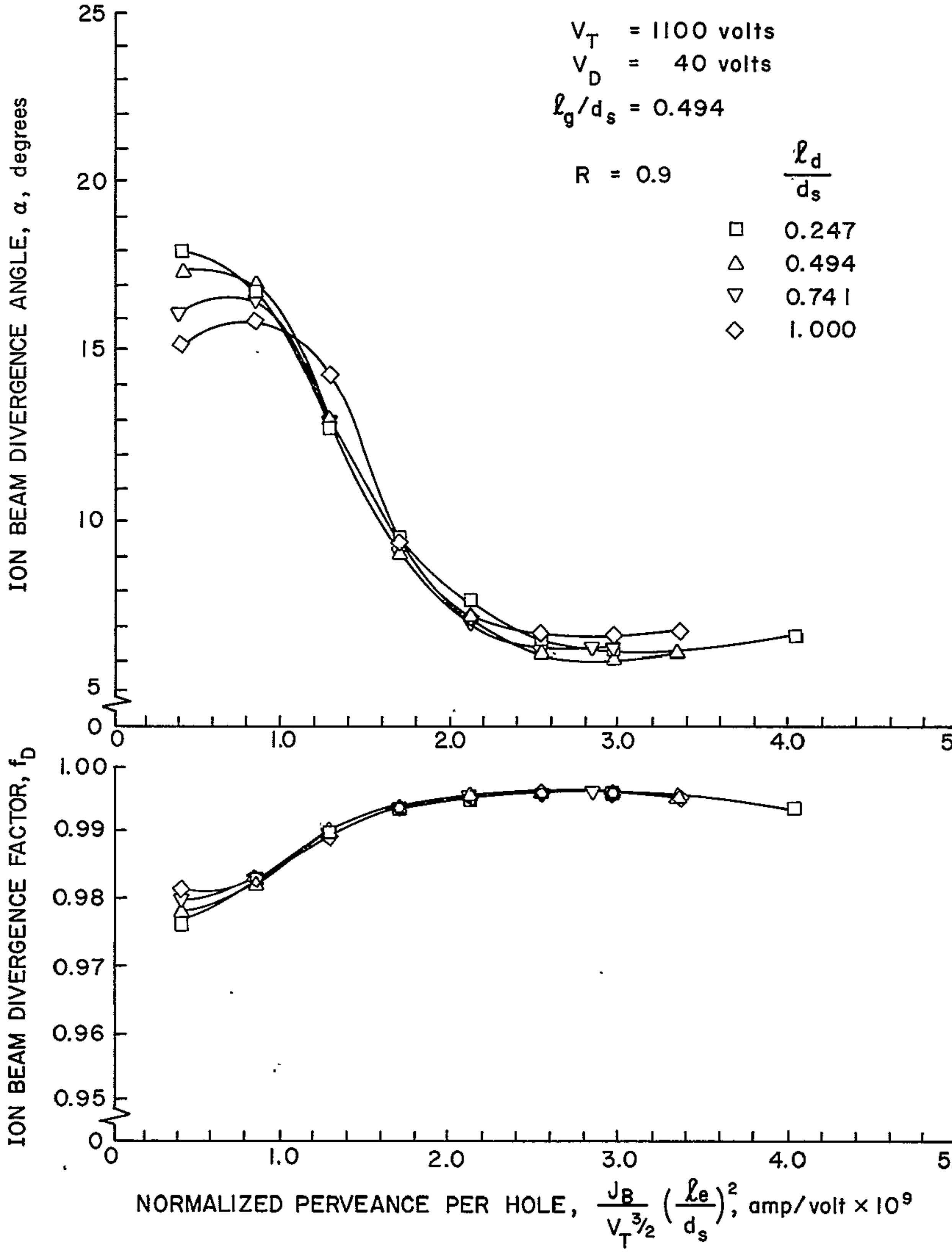

EFFECT OF DECELERATOR GAP RATIO ON DIVERGENCE
R = 0.9, ARGON

FIGURE 24

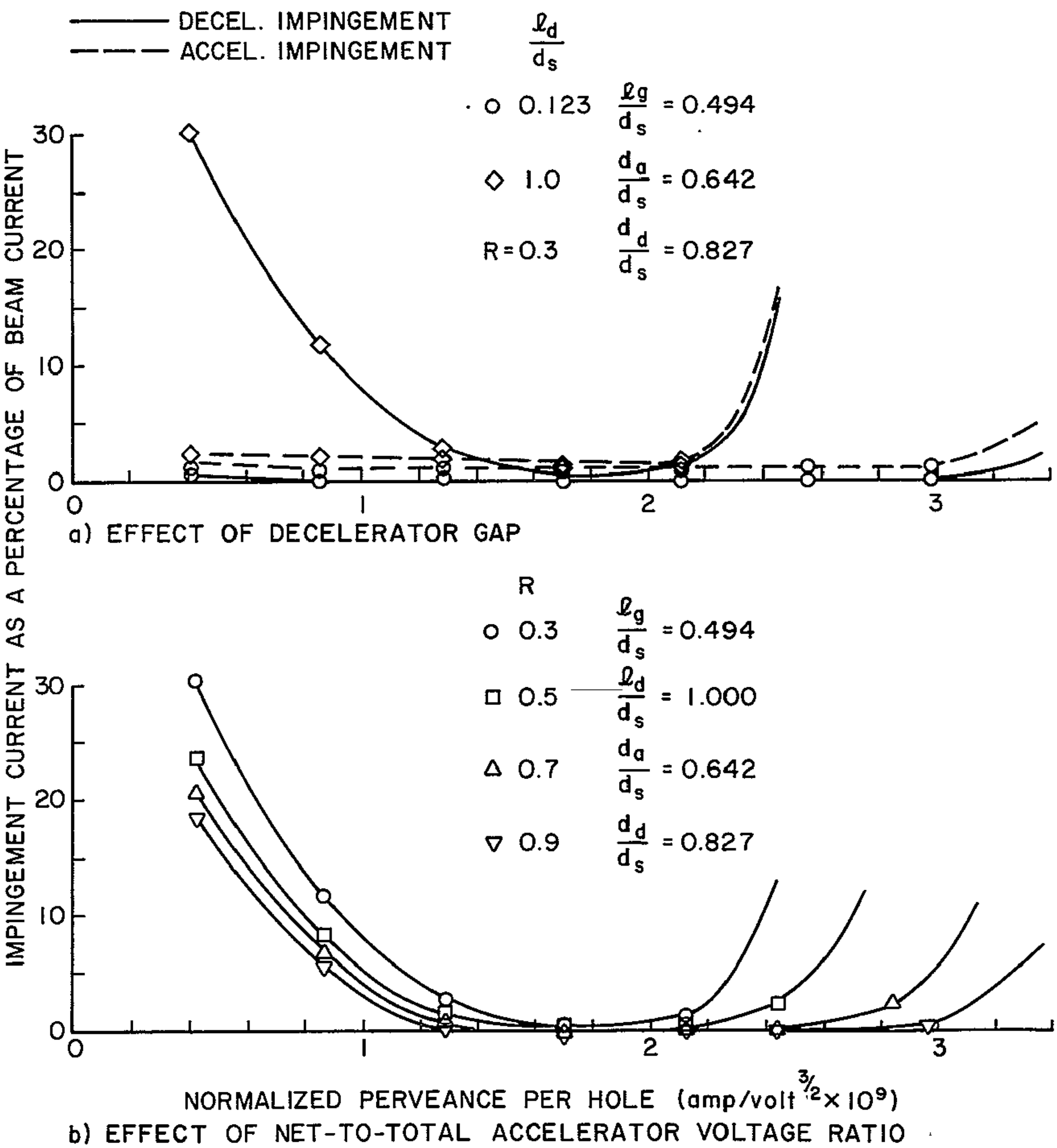

IMPINGEMENT CURRENT FOR STANDARD
THREE-GRID SET, ARGON

FIGURE 25

impingement currents, expressed as a percentage of beam current are plotted against normalized perveance, for the extreme cases of accelerator-to-decelerator separation presented in Fig. 21. At low beam currents (low normalized perveance) the decelerator grid impingement current is high. As beam current increases the decelerator grid impingement current drops quickly to a minimum value and then increases as the maximum beam current for that particular grid set is approached. By contrast, the accelerator grid impingement current increases slowly with beam current until the maximum beam current is approached, where it too increases sharply. Decelerator impingement is observed to increase sharply with an increase in accelerator-to-decelerator grid separation ($\frac{\ell_d}{d_s}$) (Figure 25a). Figure 25b shows the decelerator grid impingement current variation as a function of the net-to-total accelerating voltage ratio. Variations to the net-to-total accelerating voltage ratio, for a given grid set geometry, are seen to affect the decelerator grid impingement current less strongly than accelerator-to-decelerator grid separation ratio changes.

Figure 26 is a plot of minimum beam divergence angle obtained from Figures 21 to 24 against net-to-total accelerating voltage ratio, with accelerator-to-decelerator grid separation ratio as a parameter. A two-grid accelerator system divergence angle curve is also shown for comparison. Significant beam divergence angle reductions for three-grid accelerator systems over two-grid accelerator systems are apparent, even for a relatively high net-to-total accelerating voltage ratio of 0.7. Extrapolating the two and three-grid minimum divergence angle curves of Fig. 26 shows that they cross at a net-to-total accelerating voltage ratio of about unity. Figure 27 compares minimum beam divergence angle results obtained experimentally to those obtained theoretically by Kaufman.[4] Qualitative agreement

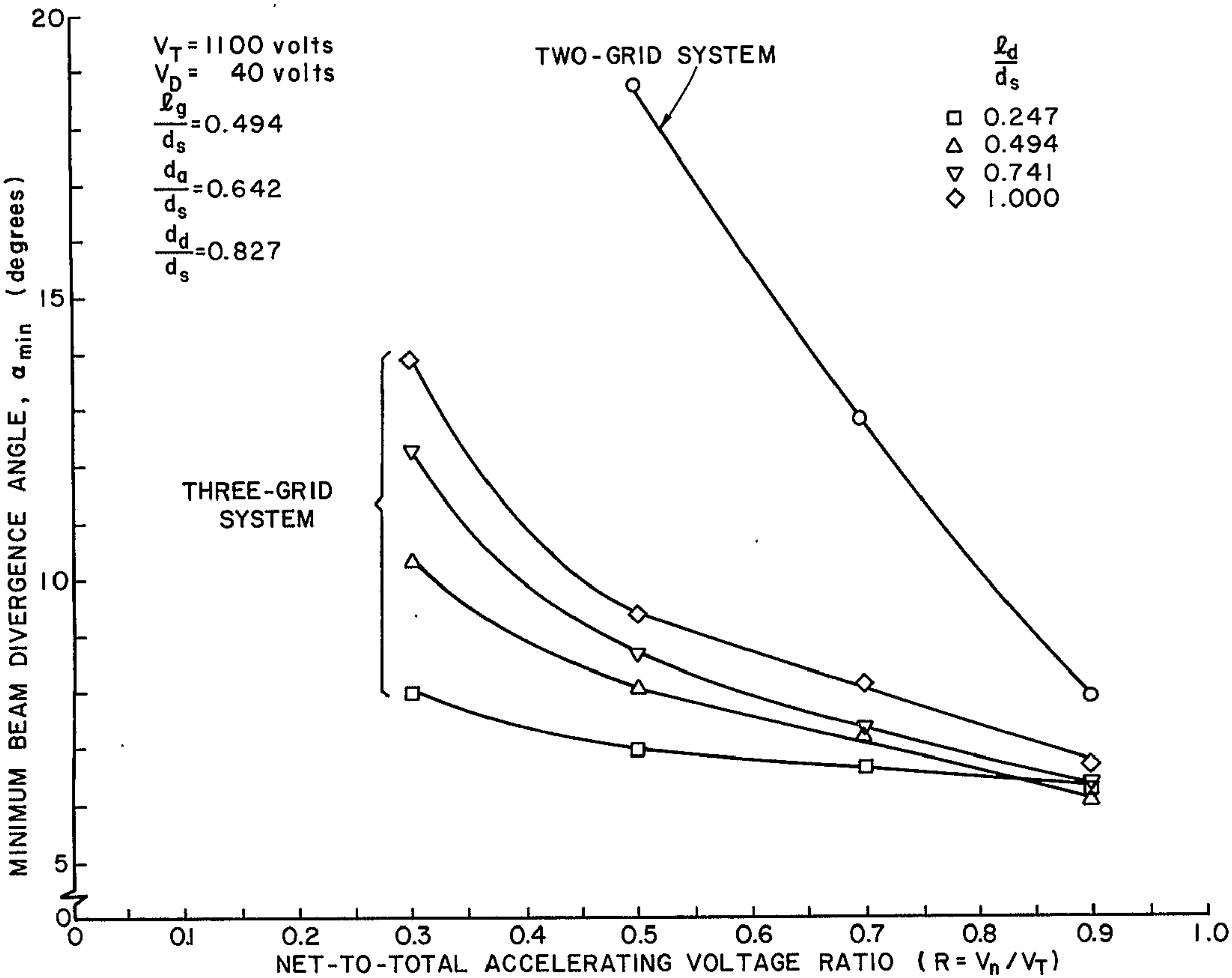

EFFECT OF NET-TO-TOTAL ACCEL VOLTAGE RATIO
ON MINIMUM DIVERGENCE OF TWO AND THREE-GRID ARGON SYSTEMS

FIGURE 26

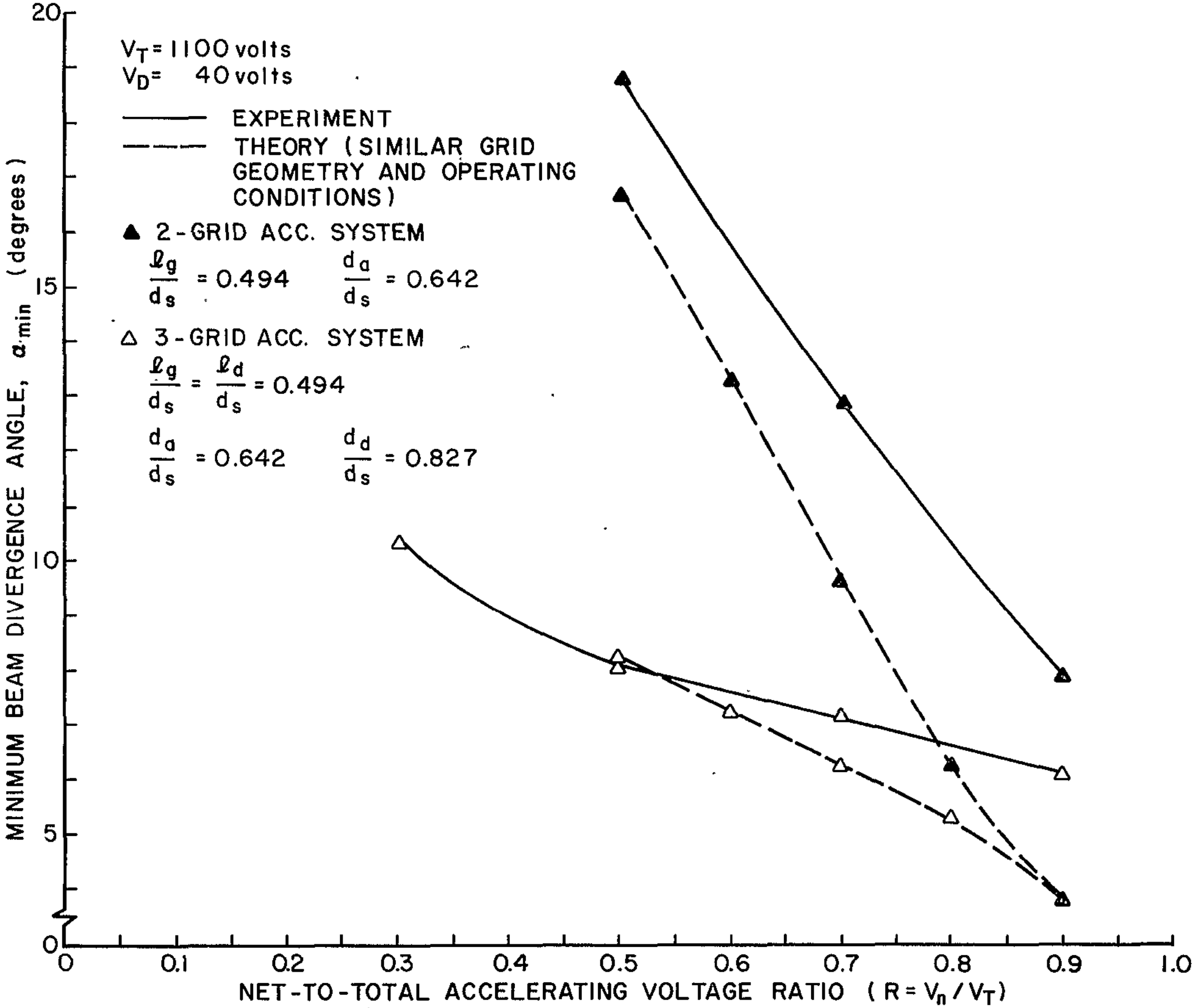

FIGURE 27
COMPARISON OF THEORY AND EXPERIMENT
TWO AND THREE-GRID SYSTEMS

between theory and experiment is seen to be good, but the experimental results do show a more substantial reduction in divergence angle associated with the substitution of three for two-grid accelerator systems than the theory predicts.

Perhaps the most striking difference between the results of Figs. 21 through 24 and two-grid data contained in the preceding section lies in the very sharp approach to the minimum divergence angle for three-grid accelerator systems. Typically, the operation of three-grid systems at, or near, the minimum beam divergence angle is restricted to a very narrow normalized perveance (or beam current) range. Unfortunately, this problem is most severe for low net-to-total accelerating voltage ratios, where three-grid accelerator systems have their greatest focusing advantage and hence greatest potential use. Although, as was previously mentioned, only negligible focusing gains are realized by reducing the accelerator-to-decelerator grid separation ratio ℓ_d/d_s from 0.247 to 0.123, Figs. 21 and 22 do show a significant increase in the minimum divergence angle operating range is achieved by doing this. Successful three-grid operation would require accurate placement of the accelerator system operating condition at the minimum beam divergence angle operating point. Failure to do this would result in accelerator system operation on the steeply varying portion of the divergence angle curve. Here, small beam current fluctuations would result in large beam divergence angle variations; a condition which could result in low integrated thrust unless the ion source were beam current regulated.

Figure 28 shows the results of preliminary tests designed to determine the best decelerator hole size and accelerator-to-decelerator grid separation ratio for a given screen and accelerator grid geometry. For these

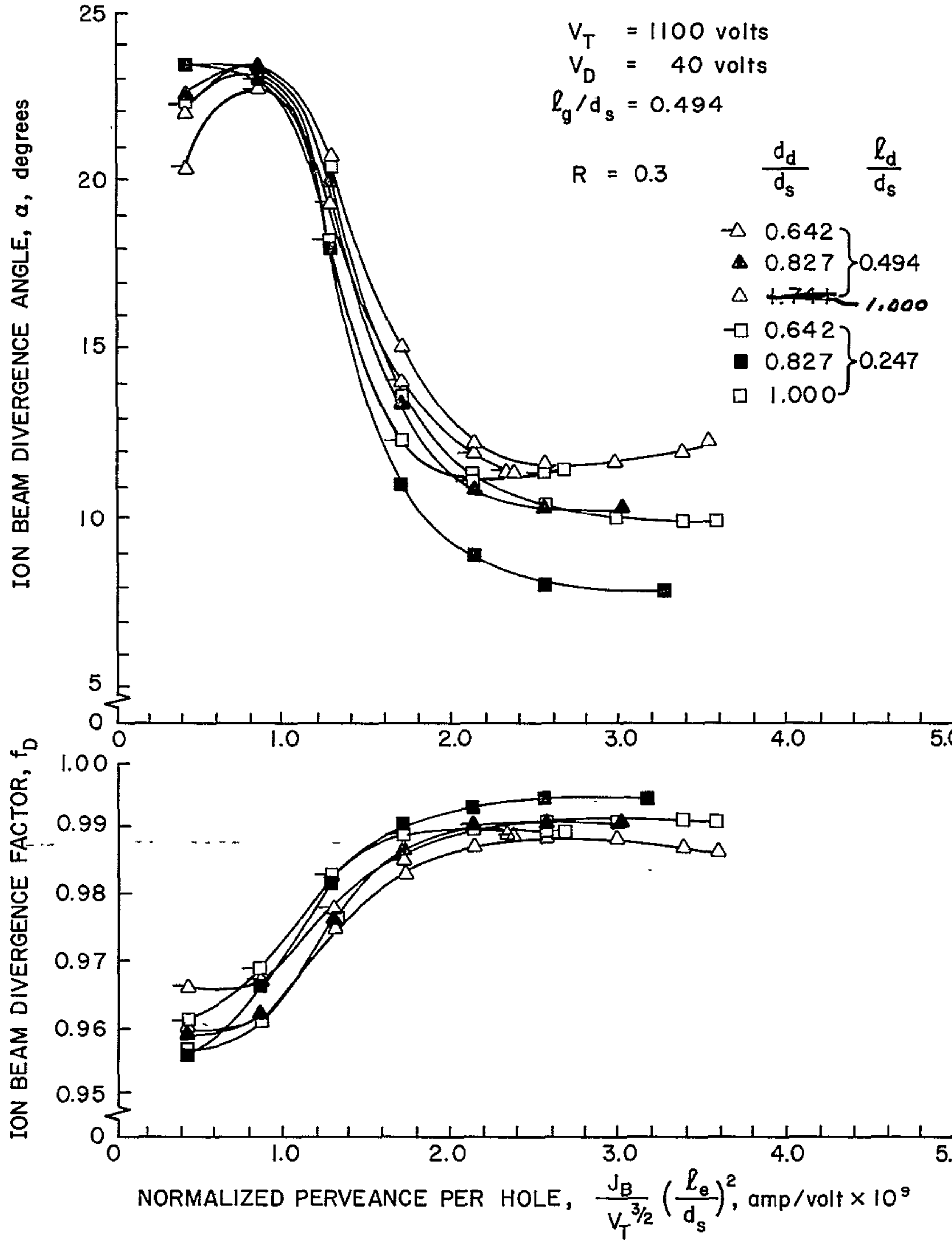

EFFECT OF DECEL GRID HOLE DIAMETER ON
ARGON ION BEAM DIVERGENCE

FIGURE 28

tests a decelerator hole diameter ratio of d_d/d_s = 0.827, and accelerator-to-decelerator grid separation ratio of ℓ_d/d_s = 0.247, gave the lowest ion beam divergence. Figure 29 shows that significant decelerator grid impingement occurs as the decelerator hole size approaches the accelerator hole size. For equal accelerator and decelerator hole sizes the decelerator grid impingement current is unacceptably high. These initial results indicate that low beam divergence and low decelerator grid impingement currents for three-grid accelerator systems require that the decelerator hole diameter be about twenty percent larger than the accelerator hole diameter (and the decelerator grid be as close to the accelerator grid as possible, as was pointed out earlier). Further work is being done to validate these accelerator system design criteria for a larger range of grid geometries and operating conditions than those shown in Fig. 28.

It should be noted that small negative decelerator grid impingement currents were observed whenever the beamlet diameter was substantially less than the decelerator hole diameter. This occurs for large decelerator hole diameter ratios, small accelerator-to-decelerator separation ratios and large net-to-total accelerating voltage ratios. These negative decelerator grid impingement currents are thought to be a result of secondary electrons produced by direct ion and charge exchange ion impingement upon the accelerator grid. The secondary electron currents are always present but they are measureable only when the ion impingement upon the decelerator grid approaches zero. These negative decelerator grid impingement currents were small, being at most 0.2% of the beam current.

Figure 30 shows the beam divergence characteristics of a low perveance, good focusing grid set (large screen-to-accelerator grid separation ratio ℓ_g/d_s), as the accelerator-to-decelerator grid separation ratio ℓ_d/d_s, is

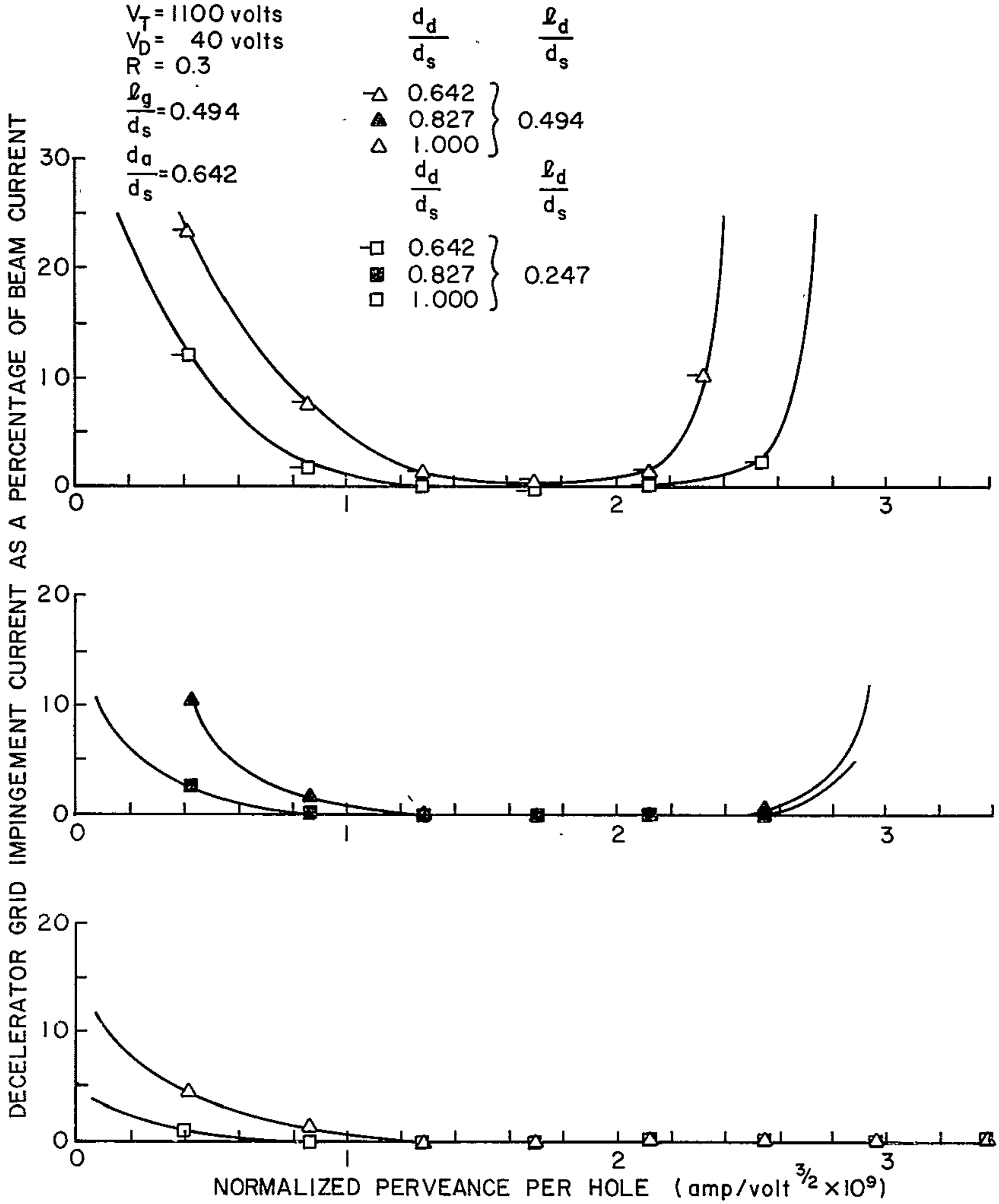

EFFECT OF DECEL GRID HOLE DIAMETER ON IMPINGEMENT

FIGURE 29

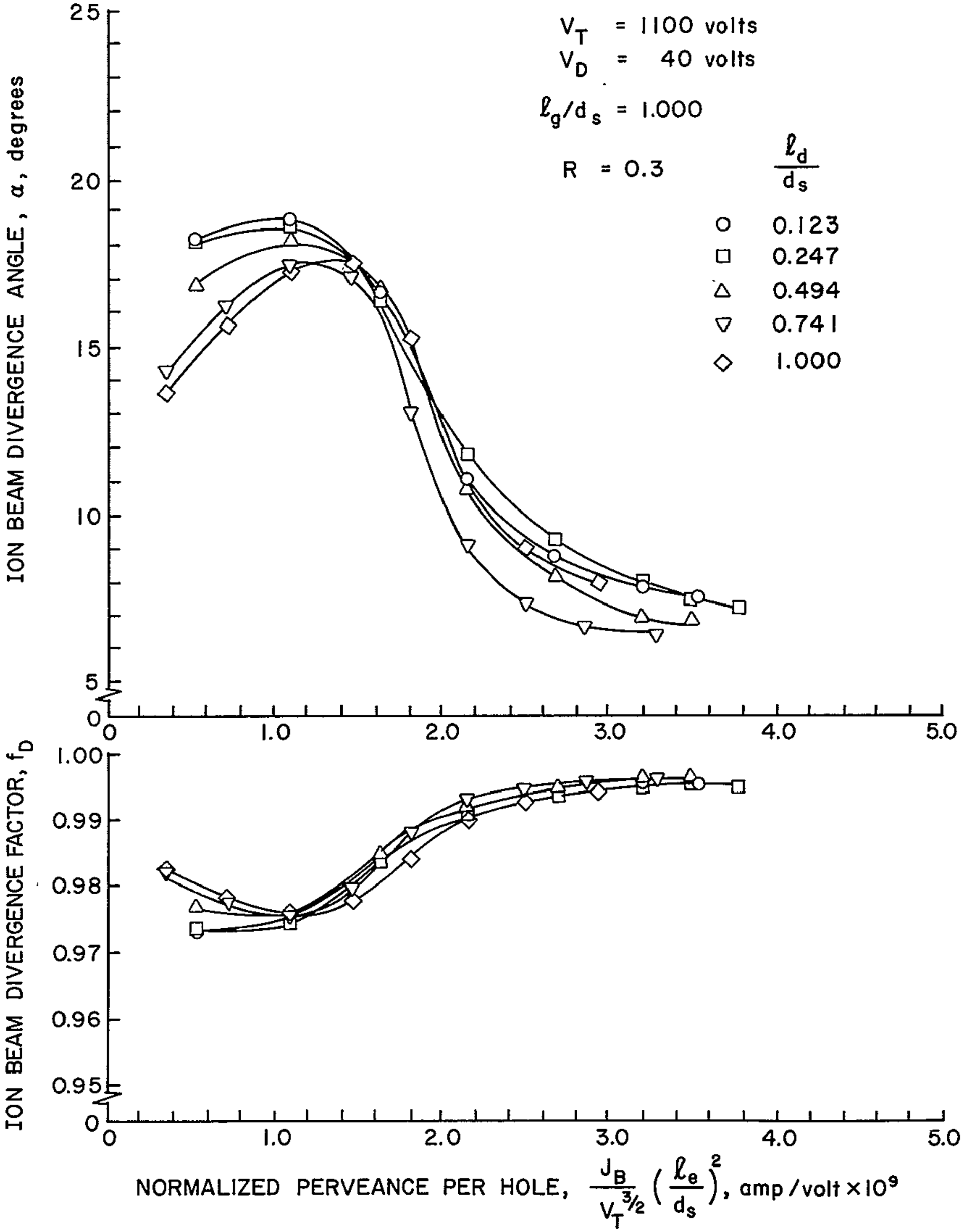

EFFECT OF DECEL GRID GAP ON ARGON
ION BEAM DIVERGENCE-LARGE ℓ_g/d_s

FIGURE 30

varied for a constant net-to-total accelerating voltage ratio of 0.3. Comparing Figs. 21 and 30 shows some striking differences. The most notable being that the minimum beam divergence angle in Fig. 30 occurs not for the minimum accelerator-to-decelerator grid separation ratio, as in Fig. 21, but for a rather large accelerator-to-decelerator grid separation ratio of about 0.7. There is no obvious reason why this should occur. Figure 30 does show that accelerator-to-decelerator grid separation ratio changes have only a minor effect on the minimum beam divergence angle magnitude. From Figs. 21 through 24 one would expect the ratio ℓ_d/d_s to have an even smaller effect as the net-to-total accelerating voltage ratio is increased.

It is possible that at an accelerator-to-decelerator grid separation ratio of about 0.7 the equipotential surfaces between the screen and accelerator grids adopt an optimum shape which results in the lowest off-axis velocity components for ejected ions and that this could effect the lowest divergence angles. However, it should be noted that an accelerator-to-decelerator grid separation ratio of 0.741 did not correspond to a minimum in decelerator grid impingement current. Decelerator grid impingement current for the grid sets of Fig. 30 increased with accelerator-to-decelerator separation ratio in the same manner as those of Fig. 21. Further work is being done on the large screen-to-accelerator grid separation ratio grid set of Fig. 30, to determine the minimum ion beam divergence angle possible with high net-to-total accelerating voltage ratios.

Conclusion

The use of three-grid accelerator systems in place of two-grid accelerator systems offers significant improvements in ion beam focusing. These improvements are greatest for low net-to-total accelerating voltage ratios and they should be negligible at a net-to-total accelerating voltage ratio of about 1.0: For a small screen-to-accelerator grid separation ratio, ion beam divergence decreases with decreasing accelerator-to-decelerator grid separation ratios and increasing net-to-total accelerating voltage ratios. This effect becomes small and is masked by second order focusing effects for a large screen-to-accelerator grid separation ratio. Decelerator grid impingement current increases sharply as either the accelerator-to-decelerator grid separation ratio is increased or the decelerator hole diameter is reduced to the size of the accelerator hole diameter. Net-to-total accelerating voltage ratio variations do not affect decelerator grid impingement current as much as either of the parameters mentioned above. Initial results indicate that low beam divergence and low decelerator grid impingement currents for three-grid accelerator systems require that the decelerator grid be as close to the accelerator grid as possible and the decelerator hole diameter be about twenty percent larger than the accelerator hole diameter. Ion source beam current regulation is desirable when using three-grid accelerator systems to insure continued accelerator system operation over the narrow beam current range at which the minimum beam divergence angle occurs.

KEEPER ELIMINATION STUDY

The major motivation for eliminating the keeper is the simplification associated with the removal of this electrode, its power supply and controls from a thruster system. In order to determine whether its elimination would degrade thruster performance, stability and/or operating and start up reliability a 15 cm SERT II thruster, equipped with high perveance dished grids, was tested in a mode where the keeper could be readily switched in or out electrically. This facilitated direct comparison of thruster start up and operation with and without the keeper.

Test Description

A SERT II thruster[18] equipped with high perveance small hole accelerator grids (67% open area screen and 24% open area accel) was used for this test. It was modified so the cathode was isolated electrically from the thruster body. Further, it was connected to the required power supplies in the manner shown in Figure 31, through the switch "S", which was installed so the keeper could be isolated from or connected to its power supply, while the thruster was operating. High voltage tickler electrodes were not used to facilitate start up during any of the tests. During normal thruster operation the switch "S" in this figure is closed and the resistor "R" is an open circuit. Start up is achieved in this "conventional keeper" configuration by biasing the keeper a few hundred volts positive of the cathode to establish the keeper-cathode discharge.

To test the effect of keeper elimination the switch "S" was opened so the keeper floated and, while it was still present in the thruster, it did not participate in the discharge process. Further the resistance of "R"

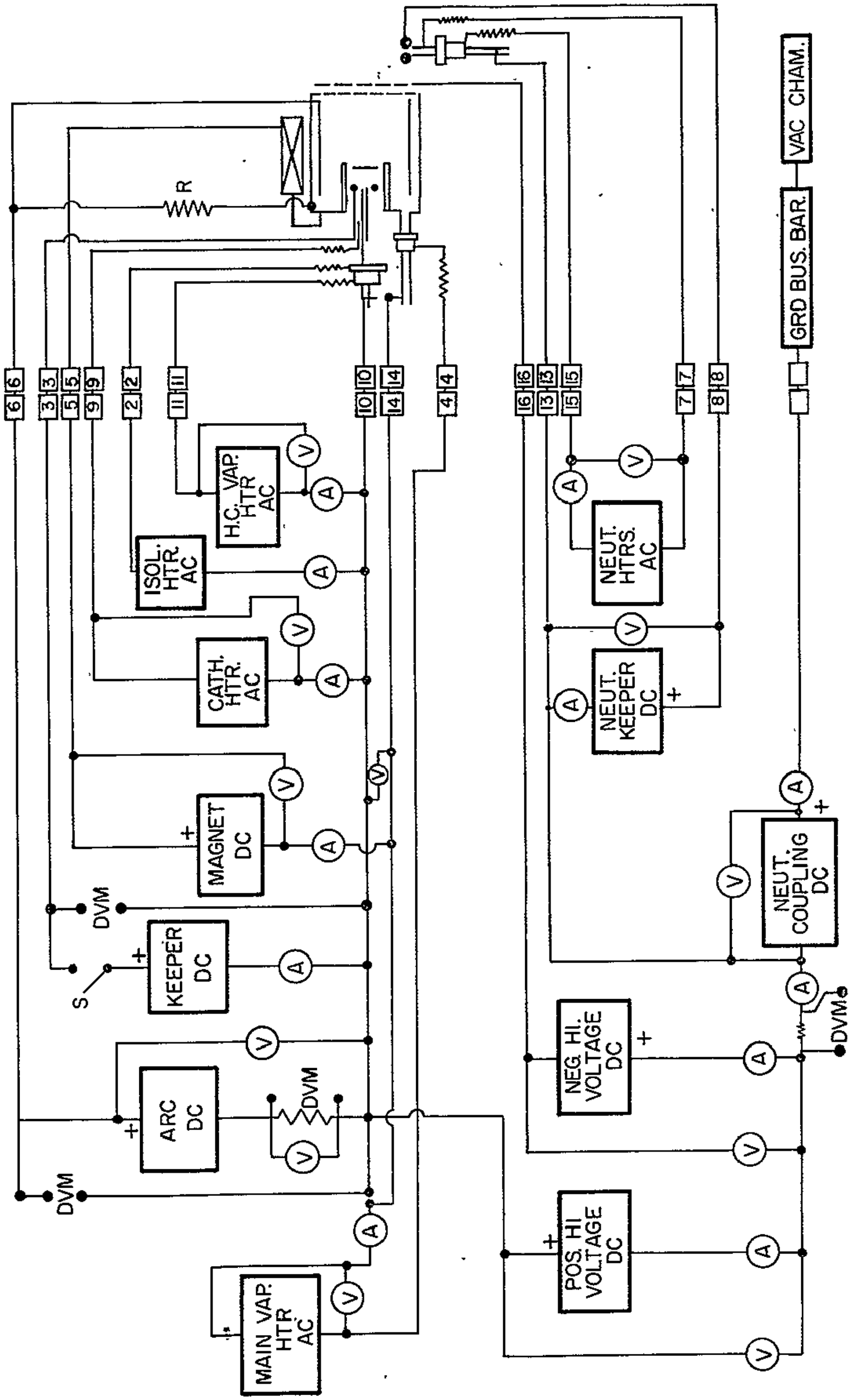

POWER SUPPLY SCHEMATIC

FIGURE 31

was set at 100 Ω so start up could be achieved in the manner suggested by Kaufman, et al.[12] With the thruster arranged in this configuration and the discharge extinguished, the entire thruster body, the screen grid and the cathode pole piece are biased to anode potential through the resistor "R". Anode potentials of 60 V were generally sufficient to effect start up although 100 V was required on one occasion. After start up the cathode couples to the thruster body, screen grid and cathode pole piece through the plasma thereby inducing a voltage drop across "R". The current to these thruster surfaces is sufficiently small that this voltage drop (the potential difference between the surfaces and the cathode) is of the order of several volts. The value of the resistor "R" was varied during the test and, while it would be preferred to use a higher resistance to minimize losses in the resistor, it was found that with higher resistances the discharge would extinguish and not restart until the high voltage was turned off. With a 100 Ω resistor installed the thruster ran stably and started reliably.

Because only electrical alterations were required to shift between the two operating configurations, this change could be accomplished quickly and variations in start up and operating characteristics of the thruster due to propellant flow rate changes were eliminated.

The Effect of the Keeper on Performance

Figure 32 shows a typical comparison of the potentials of various thruster surfaces as a function of discharge current for the thruster operating 1) in the conventional way (at 0.3A keeper current) and 2) with the keeper disconnected. With the keeper disconnected it floats and provides an indication of the plasma potential in the cathode discharge

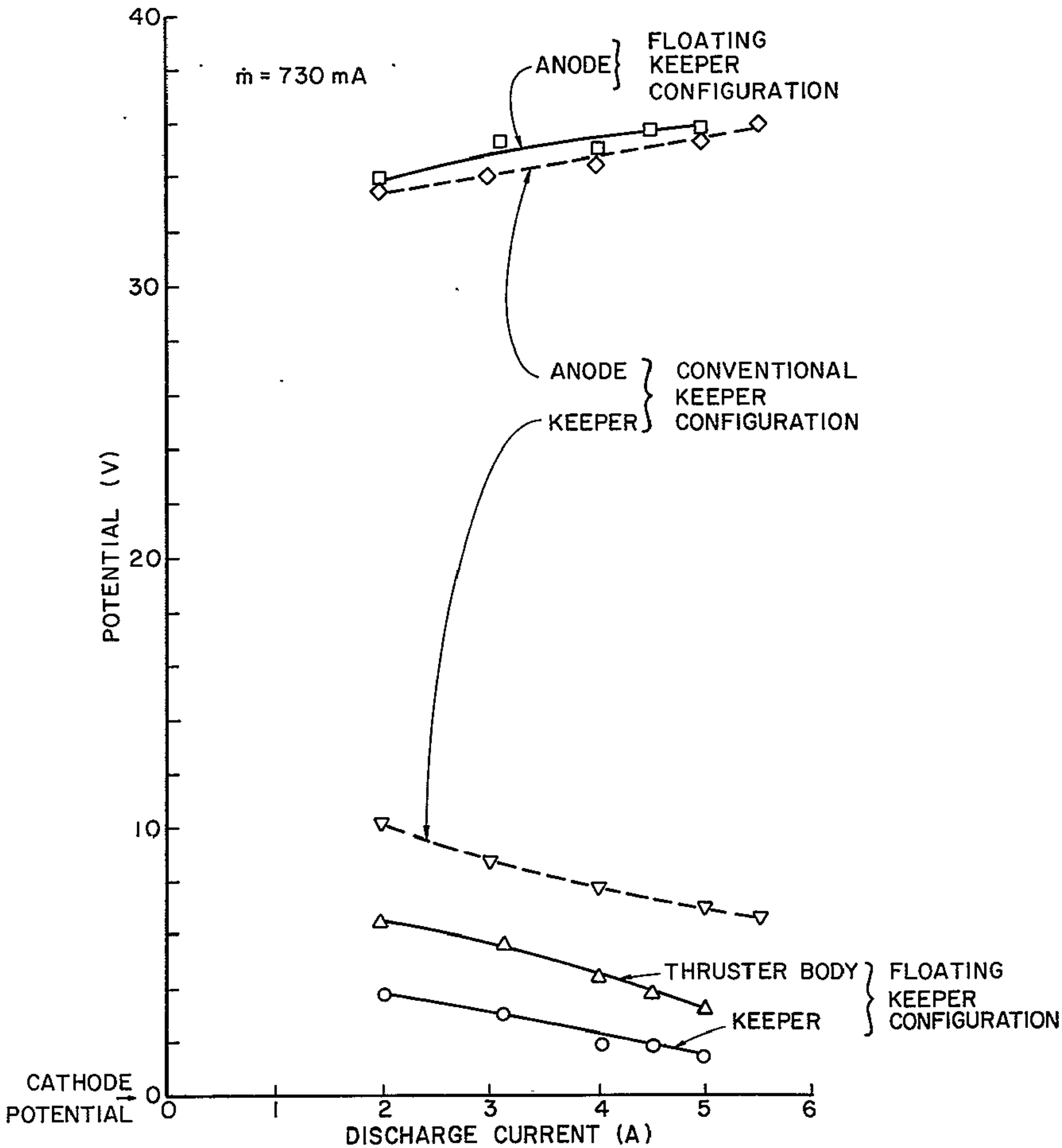

EFFECT OF KEEPER ON THRUSTER POTENTIALS

FIGURE 32

region. Figure 32 shows therefore that in the "keeper floating" configuration the keeper-to-anode potential difference is greater than it is in the "conventional keeper" configuration. At a given anode potential therefore primary electrons will acquire more energy as they pass into the main discharge region in the "keeper floating" configuration. In addition Figure 32 shows that the thruster body operates positive of the cathode in the "keeper floating" configuration. One would expect a reduction in the ion sputtering damage of the screen grid, baffle and other thruster body-potential surfaces to accompany this change for the following reason. An increase in the potential of the thruster body relative to the anode potential implies a reduction in the plasma-to-body potential difference. This in turn implies a reduction in the energy of the ions which strike the body-potential surfaces and hence a reduction in the associated damage.

Figures 33 and 34 show the effect of eliminating the keeper on the discharge loss-propellant utilization plots for the two total flow rate cases of 730 mA (full flow) and 435 mA (throttled flow). The solid symbols on each curve correspond to operation at a 35 V discharge voltage. The performance penalty associated with the "floating keeper" configuration is observed to be negligibly small for both flow rates. It is interesting to note that part of the power going to the thruster bypasses the discharge chamber through the resistor "R" in the "floating keeper" configuration. This corresponded to discharge loss of 20 eV/ion at the solid symbol operating point of Figure 33. If a switching circuit were employed which connected the thruster body to the anode when the discharge extinguished, in place of the resistor "R", this loss could presumably be eliminated. This should result in a lowering of the "floating keeper" curve by approximately 20 eV/ion.

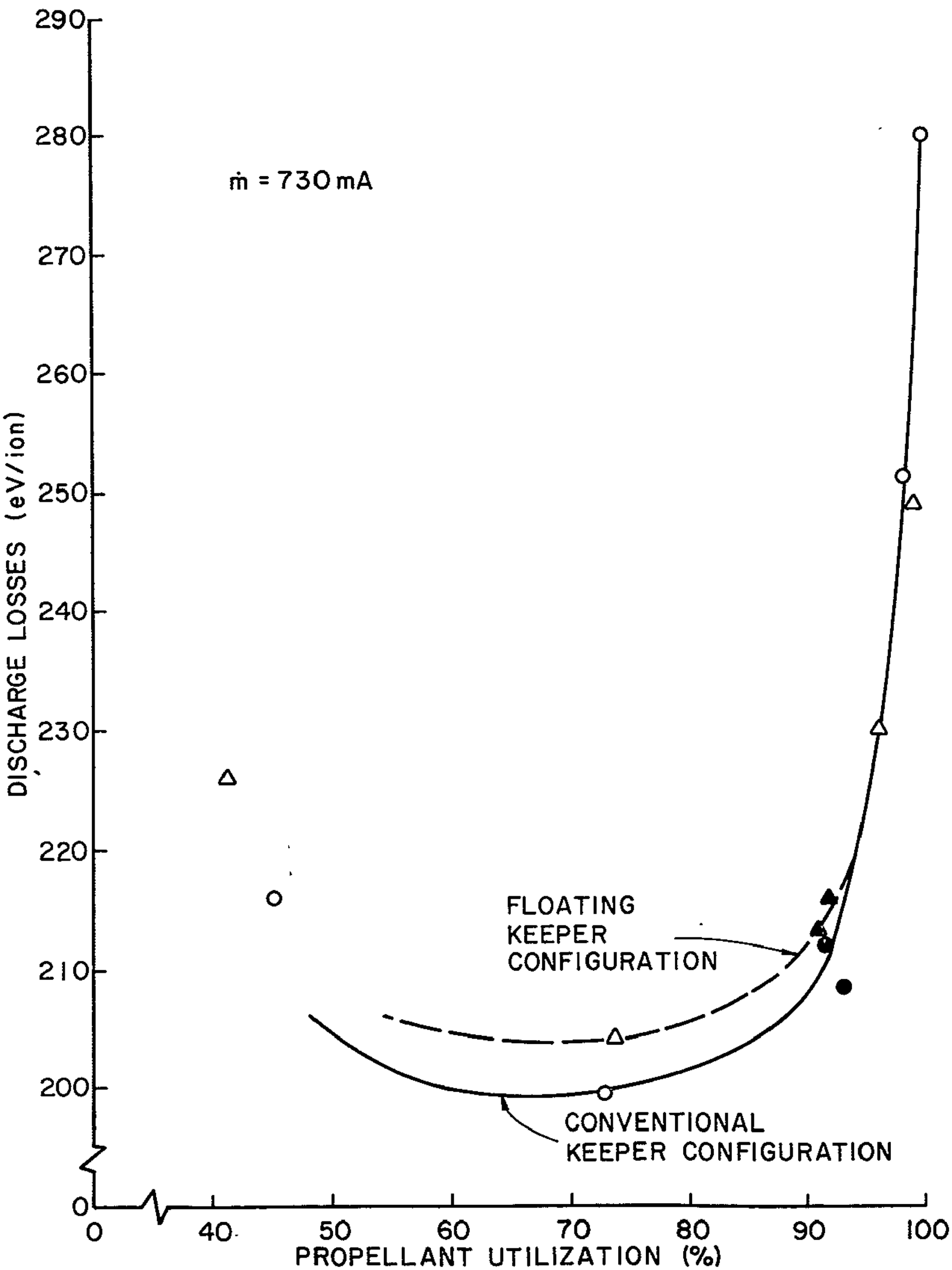

EFFECT OF KEEPER ON PERFORMANCE
15 cm SERT II THRUSTER

FIGURE 33

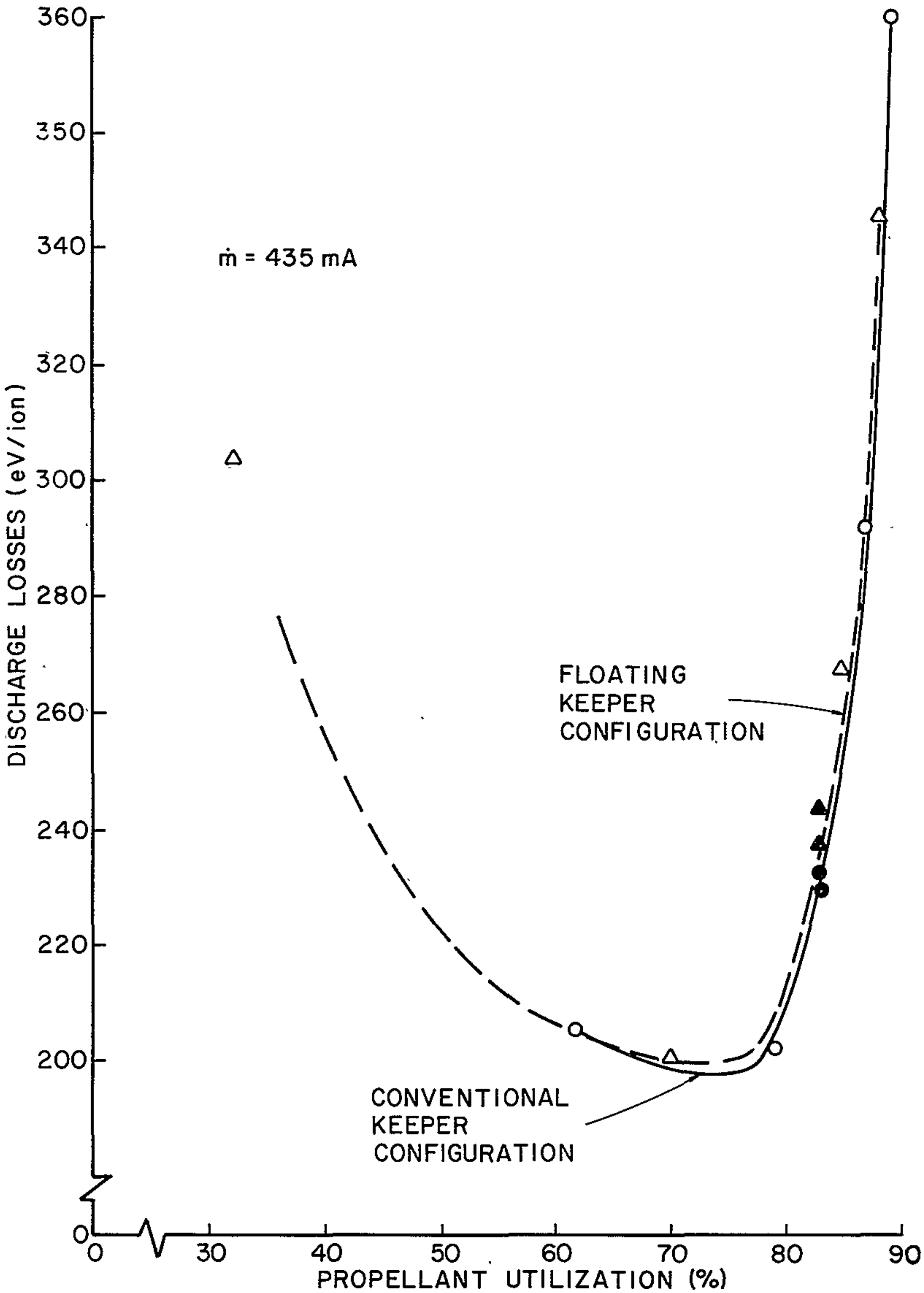

EFFECT OF KEEPER ON PERFORMANCE
THROTTLED 15 cm SERT II THRUSTER

FIGURE 34

Doubly-to-singly charged ion density ratios were also measured using an E x B momentum analyzer during these tests. They suggested slightly higher doubly charged ion densities for the "floating keeper" configuration. Unfortunately the momentum analyzer was found to be giving irreproducible results shortly after these tests and the results are therefore considered unreliable and they are not presented here.

Conclusion

The application of a 100 Ω resistor between the anode and thruster body of a 15 cm mercury ion thruster provides sufficient coupling between these two components to facilitate thruster start up at normal anode voltages without the aid of a keeper. Operation in this configuration causes no significant degradation in thruster performance or stability and it results in a biasing of the thruster body and screen grid above cathode potential. This biasing should have the beneficial effect of reducing ion sputtering damage.

MERCURY HOLLOW CATHODE STUDIES

Dan Siegfried

The operating temperature in and voltage drop across the orifice region of a hollow cathode are very important parameters which have been shown to affect the operational lifetime of the cathode. Prediction of this temperature and voltage drop as a function of cathode geometry and operating conditions requires a knowledge of the operating mechanism of the cathode and a model of energy transfer in the orifice region. At present the degree of understanding of these phenomena is limited. There have been numerous parametric studies[19, 20,21] of hollow cathodes and Bessling[22] has proposed a theoretical model of the cathode, but verification of the model as well as an understanding of the basic physical processes taking place in the cathode is still incomplete. Finally, Krishnan[23] has tested and modelled the physical processes occurring in a large diameter argon hollow cathode driven by a pulse line. The applicability of his collision model to this smaller mercury device remains to be verified. The objective of this study has been therefore to gain a better insight into the physical processes of hollow cathode operation and the applicability of these models by using Langmuir probes to map plasma properties upstream and downstream of the cathode orifice plate. A comparison of these experimental results with those predicted by the models in describing the cathode phenomena observed has also been initiated.

Apparatus and Procedure

All tests were conducted on a hollow cathode composed of a 2% thoriated tungsten orifice plate electron-beam welded to a 6.35 mm diameter tantalum tube. The orifice plate was 1.22 mm thick with a 0.75 mm diameter orifice on its centerline. The cathode contained a rolled tantalum-foil insert coated with chemical R-500 and was mounted in the operating structure shown in the cutaway sketch of Figure 35. Langmuir probes were mounted upstream and downstream of the orifice on the centerline of the assembly. They could be moved axially over a 0 to 25 mm distance from the orifice plate during cathode operation. The upstream probe entered the rear of the cathode fixture through a feedthrough fixed to the cathode body. In order to minimize leakage of mercury vapor past the probe the feedthrough was made approximately 8 probe diameters long and the probe-to-feedthrough clearance was held to about .05 mm.

Probes were constructed using quartz tubing drawn to a close fit around the tungsten electrode. Based on the initial testing, it was determined that the upstream probe electrode should be .25 mm diameter wire flush with the end of the quartz insulator and the downstream electrode should be .63 mm wire exposed for a length of approximately 1.0 mm. Using these probes, voltage-current traces were recorded at various positions upstream and downstream of the orifice plate. These measurements were recorded for anode currents ranging from .5 to 9.0 amps and mercury flow rates of 100 and 150 mA. Both spot and plume modes of operation were observed at these flow rates.

After a portion of the testing had been completed it was found that improved resolution could be obtained using much finer electrodes and drawing the quartz tubing to $\sim$.5 mm diameter for $\sim$ 5 mm behind the exposed portion of the electrode. For these tests the exposed electrode wire was .075 mm diameter by .25 mm long for the upstream probe and .125 mm diameter by 1.0 mm long for the downstream probe. Using these probes, data were

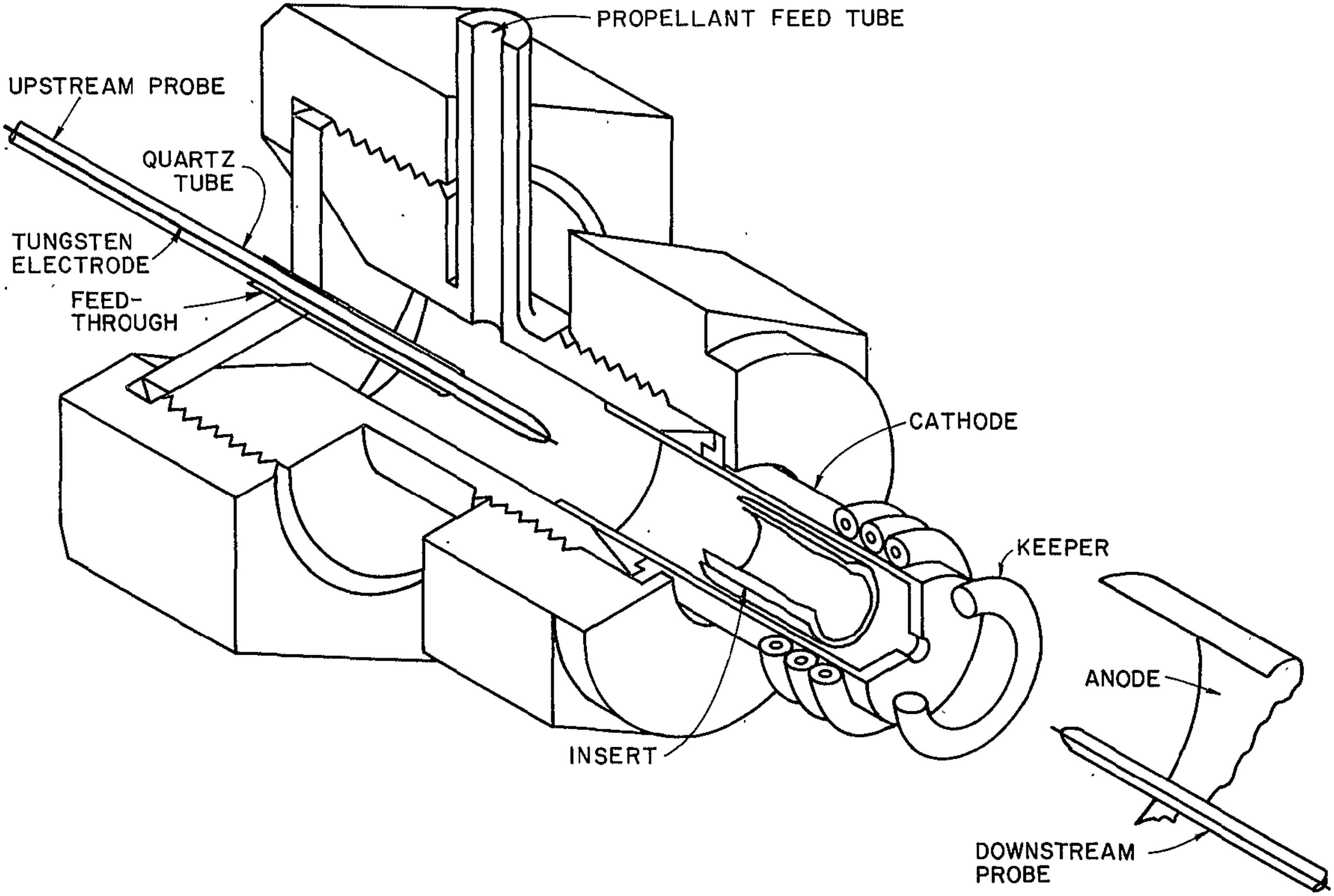

HOLLOW CATHODE TEST CONFIGURATION

FIGURE 35

recorded at a 100 mA flow rate for both 2.0 A (plume mode) and 6.0 A (spot mode) discharge currents. For all tests the keeper current was held constant at 0.3 A. Langmuir probe traces were analyzed in all cases using the technique proposed by Beattie.[24]

Experimental Results

Discharge current-voltage plots for the two flow rates investigated are shown in Figure 36. The regions of spot and plume mode operation are also indicated. The plasma properties pertaining to the currents and operating modes of Figure 36 are shown in Figures 37 through 40. These data were all obtained from measurements with the larger diameter probes mentioned under "Apparatus and Procedure." The curves are notable in that they show magnitudes of plasma properties, their variation with position and changes in the plasma associated with transitions between the spot and plume modes. For example it can be seen that in the spot mode at both flow rates the electron density profile is independent of the discharge current. In the plume mode however reductions in discharge current induce a corresponding reduction in electron density. The electron temperature and most plasma potential profiles also appear to be more strongly affected by discharge current in the plume mode. Downstream of the orifice in the highly luminious plume mode, both the plasma potential and the electron temperature increase with increasing discharge current. When the discharge switches from the plume to the spot mode, the curves for these properties drop significantly and change shape. This drop is illustrated by comparing the 3.0 A and the 7.0 A curves for the 100 mA flow rate case (Fig. 37) or the 5.0 A and 2.0 A curves for the 150 mA flow (Fig. 39). The 7.0 A and 5.0 A currents represented the lowest current levels for stable operation in the spot mode (see

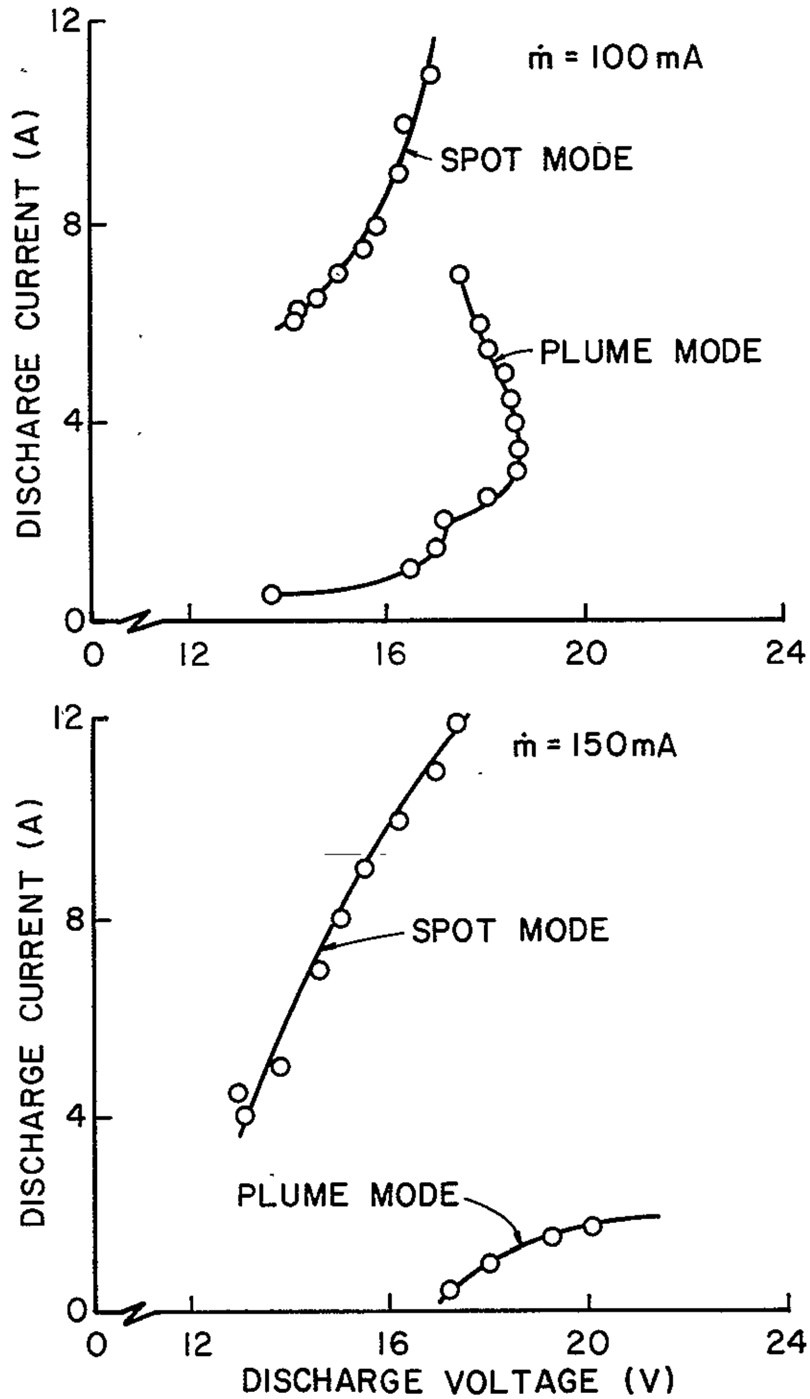

VOLTAGE-CURRENT CHARACTERISTICS

FIGURE 36

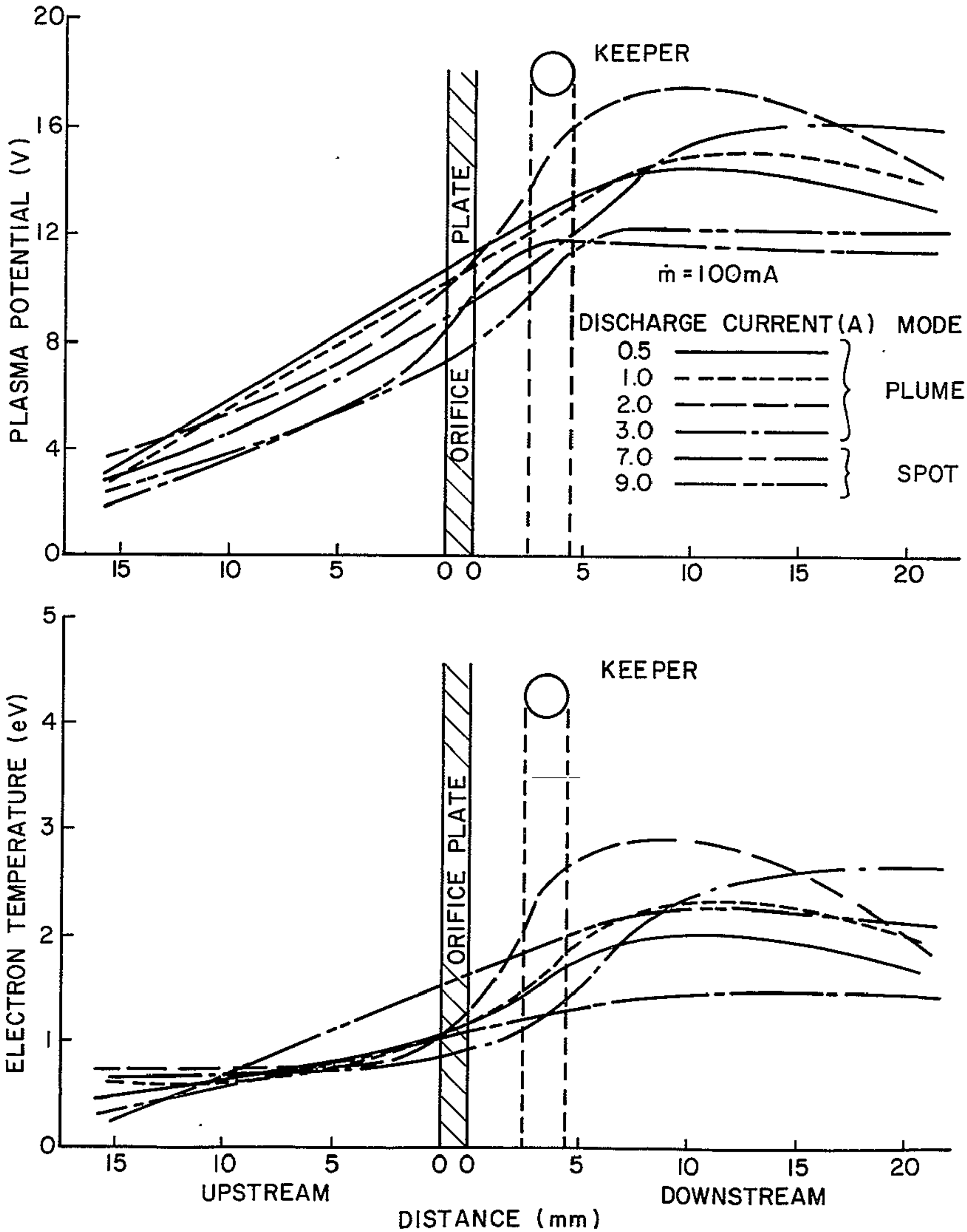

CATHODE PLASMA POTENTIAL AND ELECTRON TEMPERATURE PROFILES
100 mA FLOW RATE

FIGURE 37

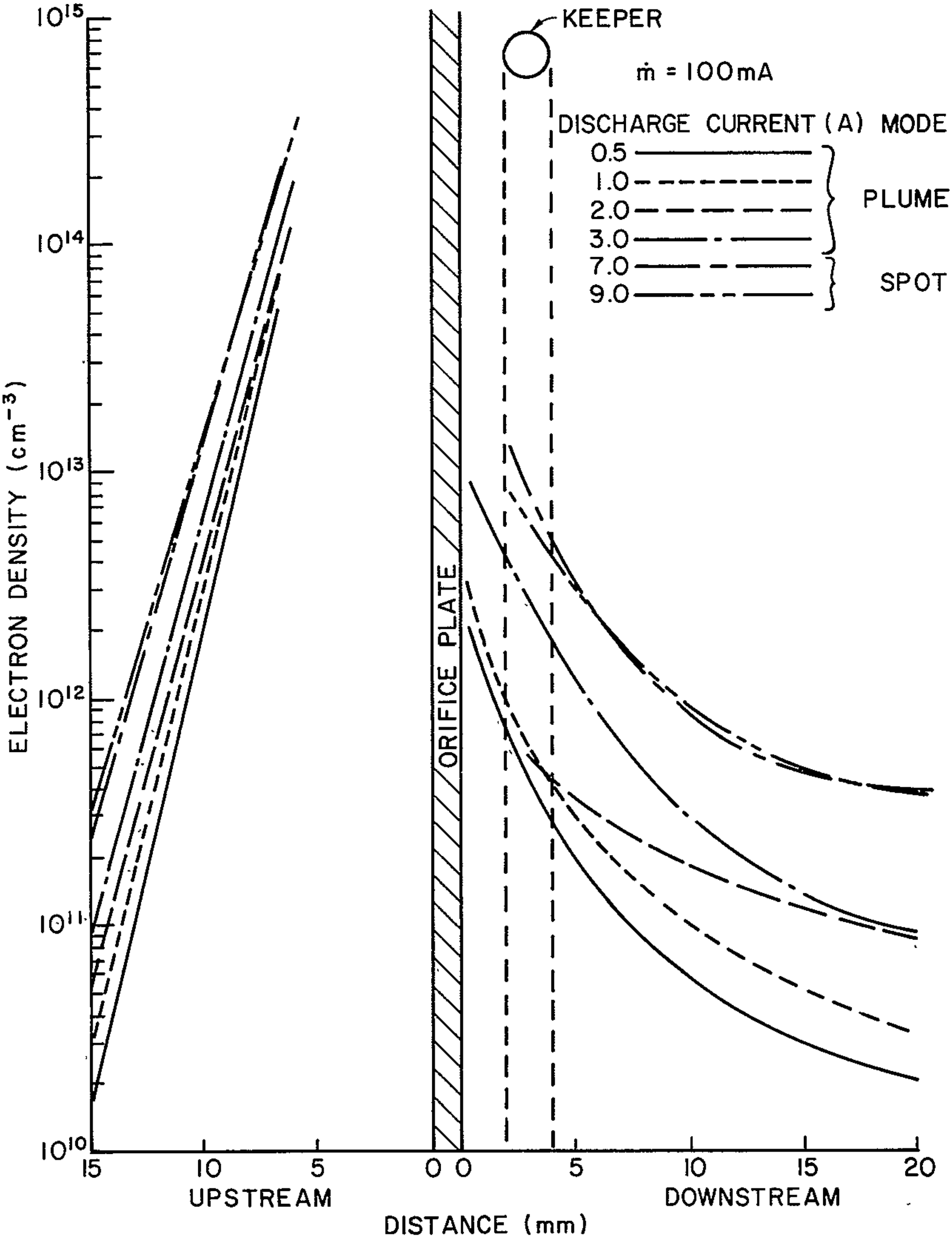

CATHODE ELECTRON DENSITY PROFILES-100 mA FLOW RATE

FIGURE 38

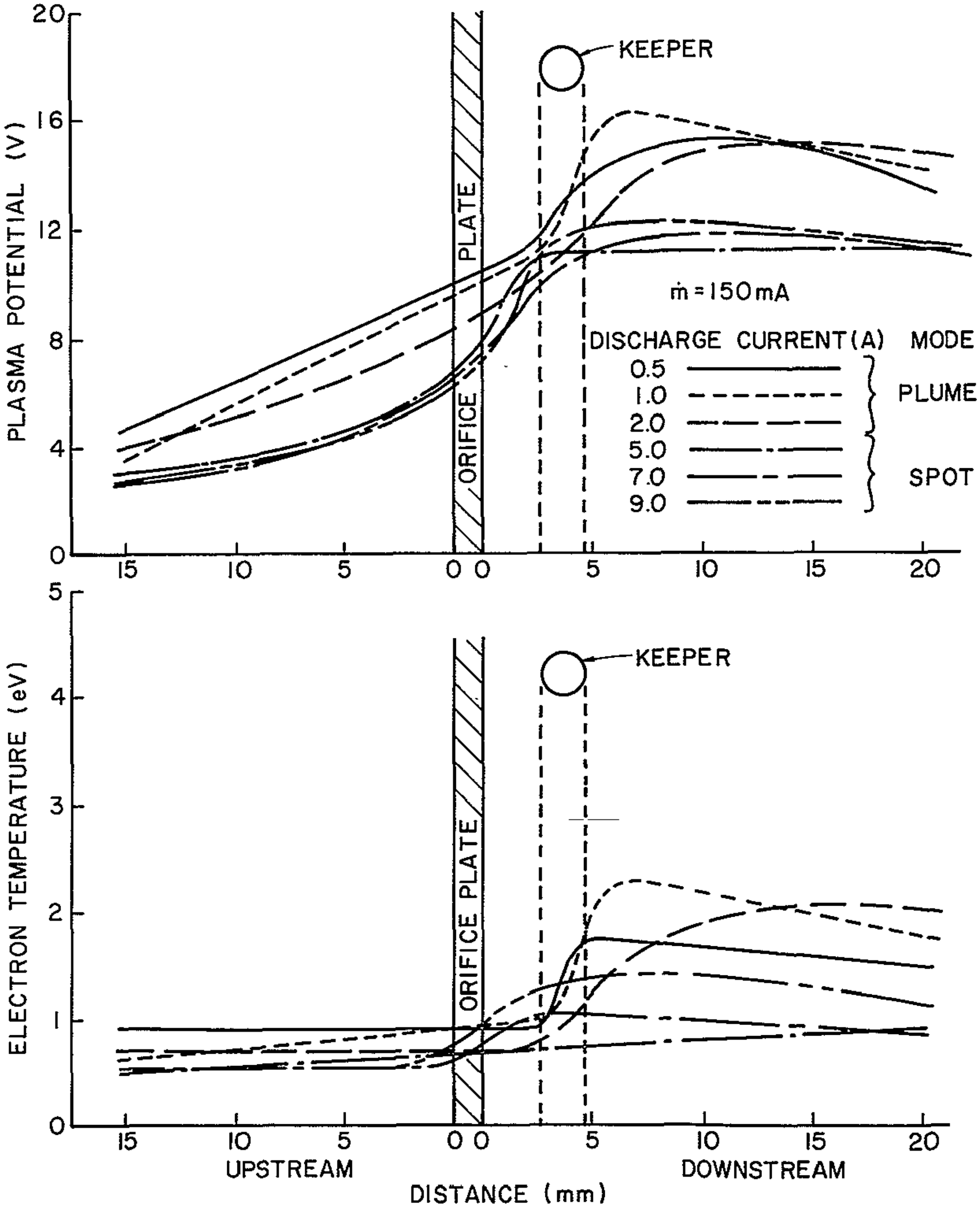

CATHODE PLASMA POTENTIAL AND ELECTRON TEMPERATURE PROFILES
150 mA FLOW RATE

FIGURE 39

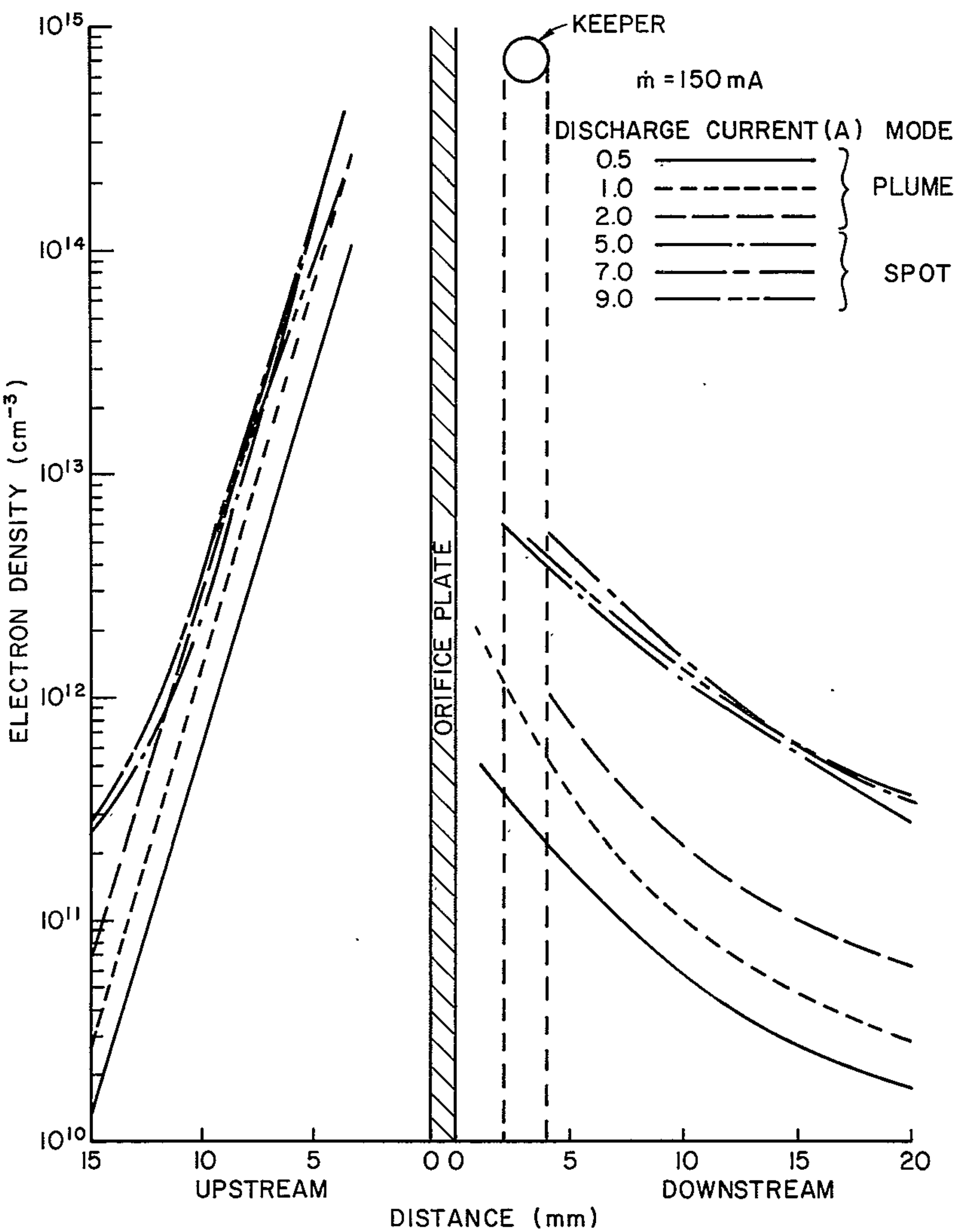

CATHODE ELECTRON DENSITY PROFILES-150 mA FLOW RATE

FIGURE 40

Figure 36) and visually corresponded to a very intense spot at the orifice with very little luminosity present away from this spot. As the discharge current is increased above this value, the plasma potential and electron temperature (Figs. 37 and 39) again increase in what appeared to be direct proportion to the intensity of the radiation from the spot.

It should be noted that it was not possible to probe the region from about 4 mm upstream of the orifice to 1 or 2 mm downstream for either mode due to the very high electron density in that region, so the curves can only be estimated there. The data scatter on the electron temperature is about .25 eV and on the plasma potential about one volt except for the 0.5 A and 1.0 A cases where it is higher. The data scatter for the electron density is less than an order of magnitude on the semi-log scale plots.

The fact that the plasma potential increases from a location some 15 mm upstream of the orifice and for some distance downstream of the orifice, as shown in Figures 37 and 39, is significant. The electron collision rate must be very high throughout the region to sustain this potential gradient. Because electron temperature is not increasing proportionately over the same region it appears that energy transferred to the electrons as they pass through this potential gradient must be lost through the collisions or by radiation.

Plasma property results measured using the smaller diameter Langmuir probes mentioned under "Apparatus and Procedure" are shown as solid lines and data points in Figures 41 and 42 for the plume mode and Figures 43 and 44 for the spot mode. These plots are very similar to the corresponding ones made with the larger probes, Figures 37 through 40, except that the steep gradients in the plasma potential and electron temperature in the region 5 to 10 mm downstream of the orifice in the plume mode were not

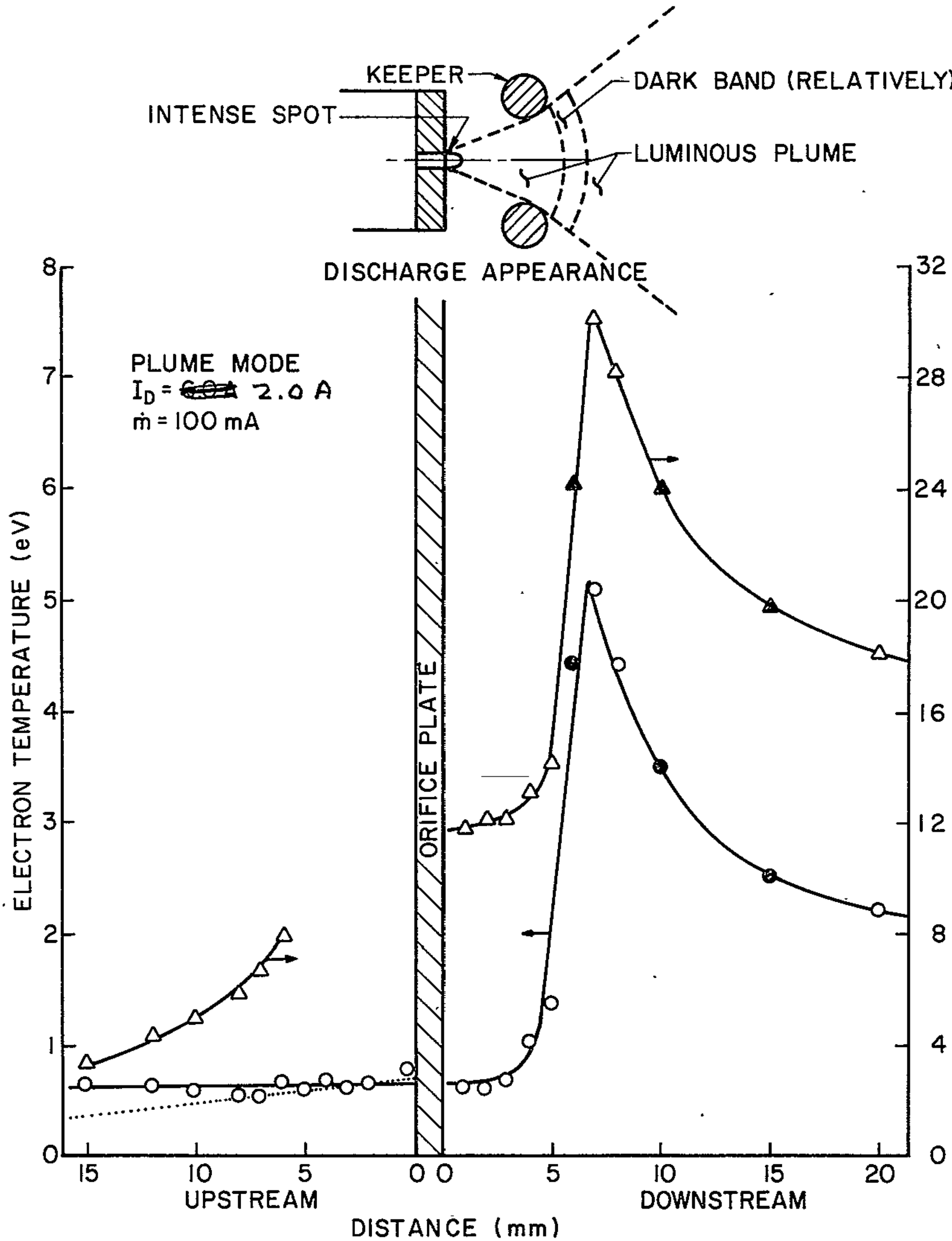

CATHODE PLASMA POTENTIAL AND ELECTRON TEMPERATURE PROFILES
PLUME MODE

FIGURE 41

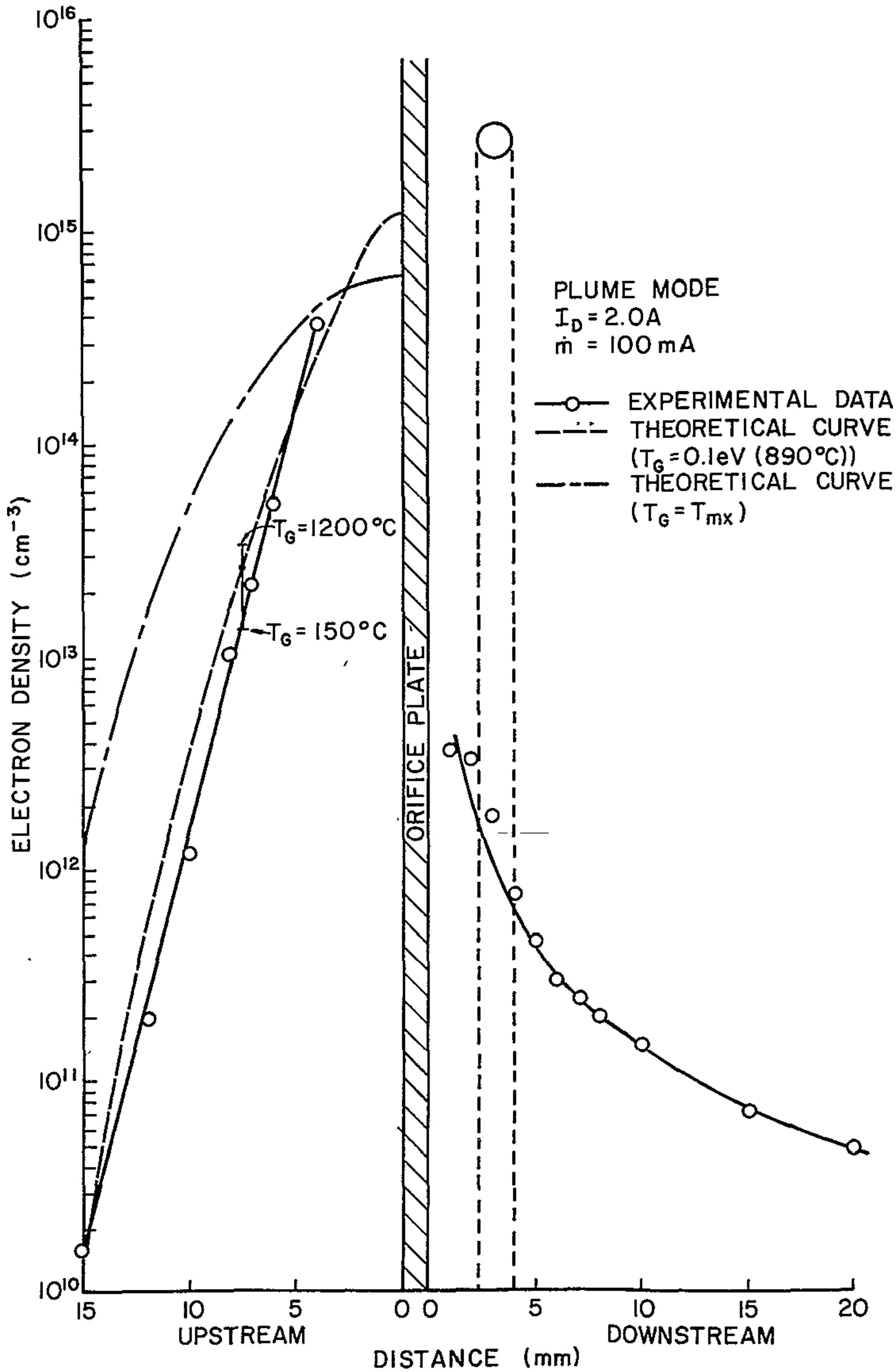

CATHODE ELECTRON DENSITY PROFILES
PLUME MODE

FIGURE 42

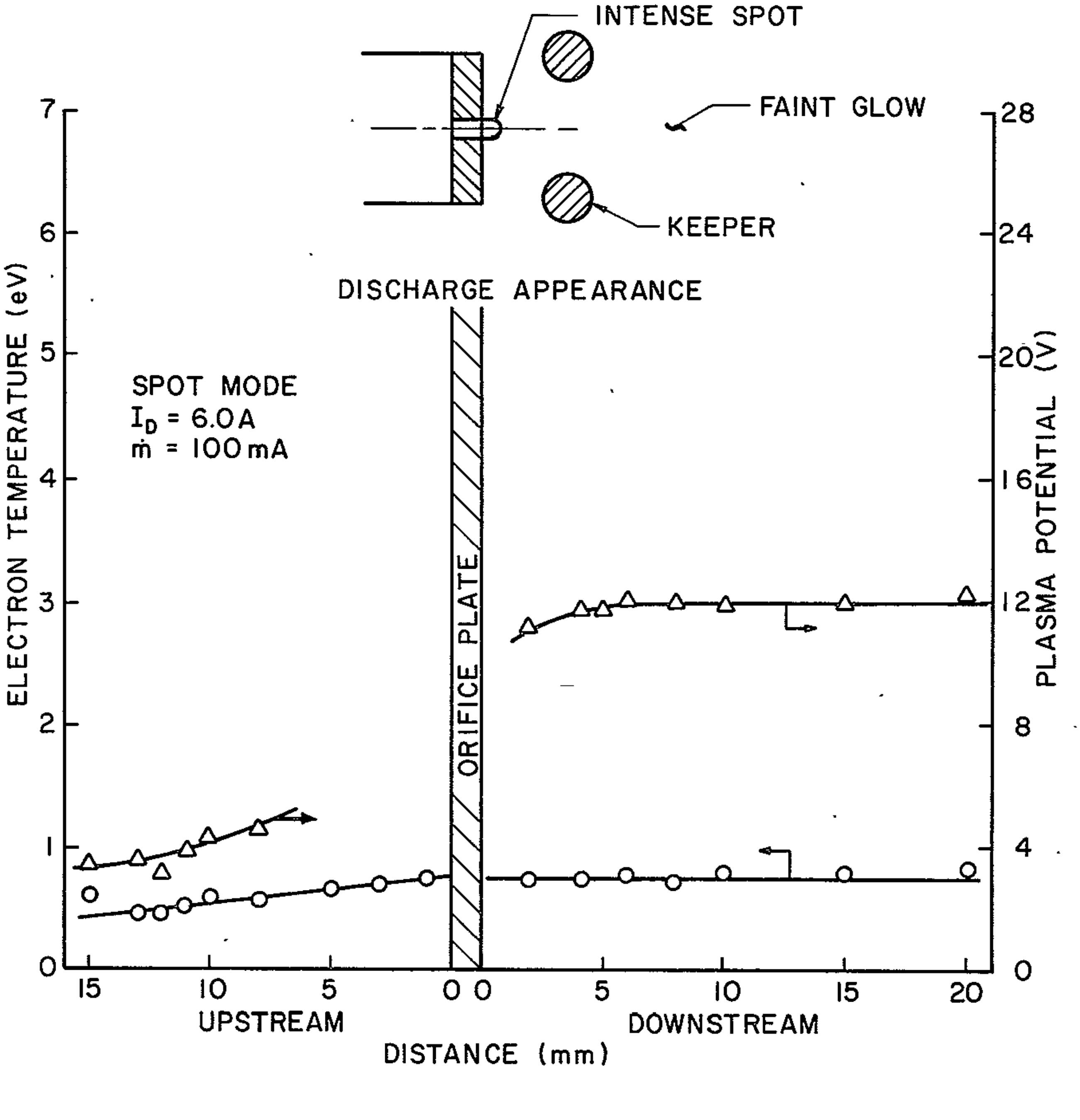

CATHODE PLASMA POTENTIAL AND ELECTRON TEMPERATURE PROFILES
SPOT MODE

FIGURE 43

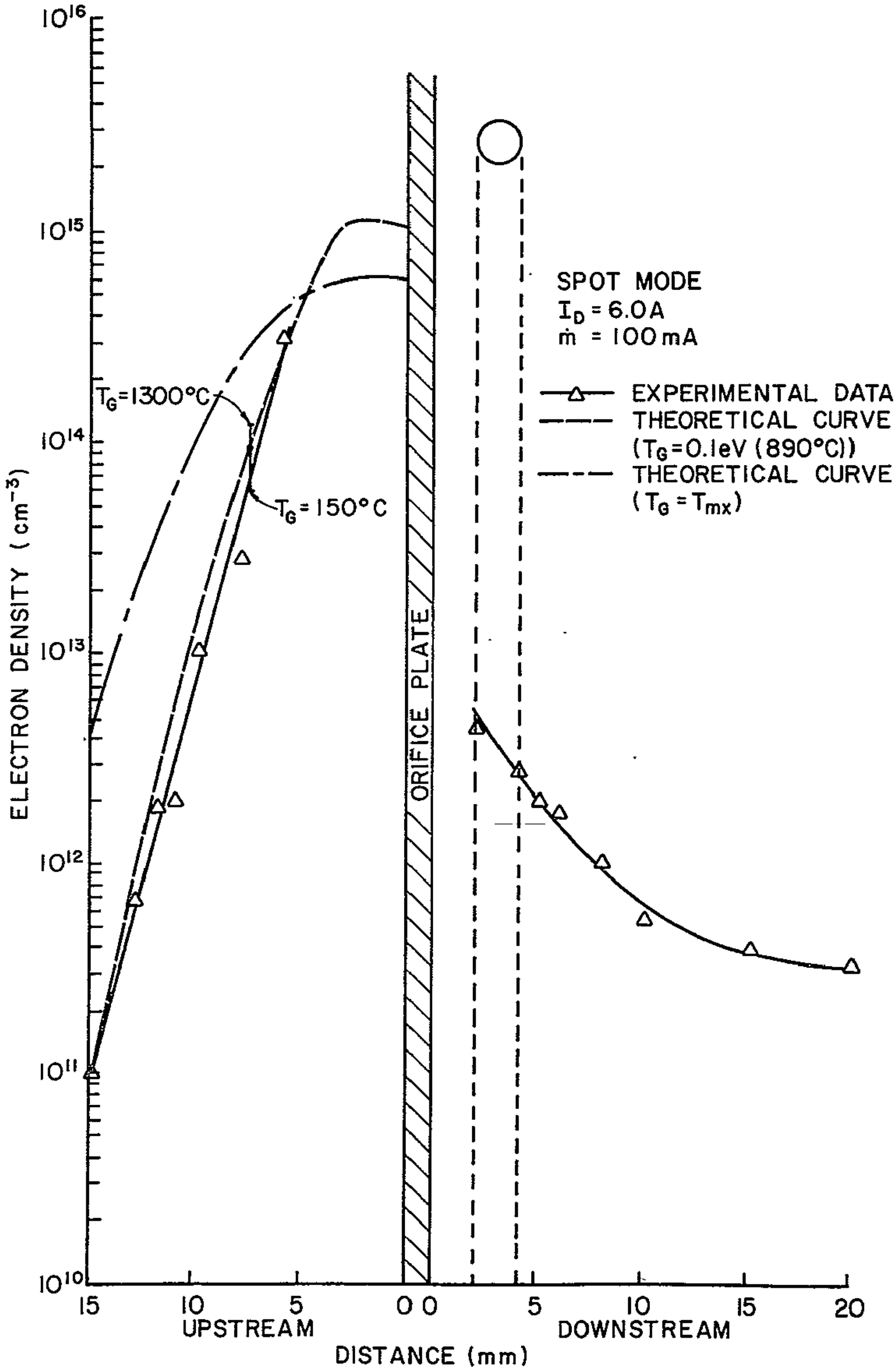

CATHODE ELECTRON DENSITY PROFILES
SPOT MODE

FIGURE 44

readily discernable from the large probe data. The presence of this spike was, however, suggested in the earlier data by a few stray data points in this region that were originally attributed to data scatter. The better resolution of the smaller probe allowed the more accurate mapping of this region.

The steep electron temperature and plasma potential gradients in Figure 41 apparently correspond to an electron free-fall region where the electrons are free to be accelerated through a potential difference of about 20 V without significant collisional interaction. That this is occurring is born out both by visual observation of the discharge and analysis of the probe traces. Observation in the plume mode showed a dark band followed by a region of more intense luminosity as shown in Figure 41. At a discharge current of 2.0 amps this band was located about 5 mm downstream of the orifice. Neither the dark band nor the spikes in plasma potential and electron temperature were present in the spot mode. It should be noted that the intense spot was present in both modes (Figures 41 and 43). It was slightly larger and noticeably more intense in the spot mode.

Computer analysis of the Langmuir probe traces indicated that near the peak in the plasma potential in the plume mode curve (Fig. 41), about 30% of the electrons were monoenergetic (primary) and that the energy of this electron group was about 19 eV. This agrees well with the $\sim$20 V rise in plasma potential which takes place between 1 and 6 mm downstream of the orifice. Electrons passing through the free-fall region would have sufficient energy to cause the luminosity seen immediately downstream of the dark "free-fall" region where inelastic exitation reactions are presumably occurring. The presence of collisions is indicated in the plasma property data by the decrease in the primary fraction and the eventual randomization of electron energies toward a Maxwellian distribution of about 2 eV as the electrons diffuse away from the free-fall region (dark band) shown in Figure 41.

The solid symbols on the electron temperature and plasma potential curves are questionable data points (Figure 41). The computer analysis of the associated Langmuir probe traces suggested no primary electrons were present, and then indicated rather large errors were brought on by a pure Maxwellian curve fit. This suggests the Maxwellian-plus-mono-energetic distribution does not fit well at these points. They are, however, considered approximately correct and they do fit with the other data. It should also be noted here that the banded appearance indicated in Figure 41 and discussed above was very faint and without sharply defined boundaries. This band has, however, since been observed under other operating conditions with .38 mm diameter orifice cathode where it was much more distinct. The dark band was observed to be very close to the luminous spot at low discharge current levels in the plume mode and to move 5 to 10 mm downstream as the current was increased. When the discharge changed to the spot mode this dark band seemed to disappear abruptly.

Two physical processes important to hollow cathode design are electron emission and heat transfer rate to the orifice. If it were possible to predict the plasma conditions at the orifice, then the calculation of both of these would be facilitated. Two approaches to the heat transfer rate calculation might be taken. In one continuum flow through the orifice would be assumed and a convective heat transfer coefficient based on local plasma properties would be employed. Bessling[22] suggests another model using a particle approach. Either approach requires assumptions which have not previously been amenable to verification. In the continuum approach an important assumption is thermal equilibrium and the applicability of the Saha equation. Bessling's model is highly dependent on the value of an assumed ionization fraction in the orifice region—a quantity which is also important in Bessling's modeling of the electron emission process. The results of Langmuir probe analysis would be most useful therefore if they could be obtained in the region of the cathode of primary interest to these models, namely the orifice region. Unfortunately reliable probe data could not be obtained within the region from 5 mm upstream to 2 mm downstream of the orifice without burning up the probe. Further, interpolated data are not reliable because of the large changes in density which appear to occur through this region. Through the application of an expanded Saha equation[22] and the designation of reasonable temperatures and pressures in the region upstream of the orifice, however, some insight into the required variation in plasma properties in this region can be obtained.

In the development of his hollow cathode model Bessling cites the expanded Saha equation mentioned above in which the electrons and neutral atoms/ions though presummably in equilibrium with themselves are at two different temperatures and therefore not in equilibrium with each other. This equation is given as

$$\frac{\alpha^{1+G}}{(1-\alpha)^G[1+\alpha/G]} = \frac{1}{P}\frac{(2\pi\ m_e)^{3/2}}{h^3}\ e^{5/2}\ T_G T_{mx}^{3/2}\left(\frac{\Sigma_i}{\Sigma_o}\right)^G \exp\left[-\frac{\phi_i}{T_{mx}}\right], \quad (6)$$

where T_G is the neutral atom and ion temperature (eV), T_{mx} is the electron temperature (eV), α is the ionization fraction, P is the total (electron plus heavy particle) pressure, m_e is the electron mass, h is Planck's constant, e is the electron charge, Σ_i/Σ_o is the ratio of internal partition functions for the singly ionized and neutral ground states (2 for mercury),

ϕ_i is the ionization potential, and G is the ratio T_G/T_{mx}. The total pressure is given by

$$P = n_e \, eT_{mx} + n_G \, eT_G \,, \tag{7}$$

where n_e and n_G are the electron and heavy particle (atom plus ion) densities respectively. The Langmuir probe data provide values for T_{mx} as a function of axial location. If T_G and P were known then the ionization fraction α and electron density n_e could be calculated from Equations 6 and 7 above at each axial location. The pressure P can be estimated by assuming that the pressure in the cathode upstream of the orifice is uniform* and is sufficient to insure choked flow through the orifice at the flow rate being maintained for the tests. Then, if energy addition in this region is neglected, the stagnation pressure is a function only of gas temperature and known physical parameters according to the equation

$$P = \frac{4\dot{m}\sqrt{T_G}}{\pi D^2} \left\{ \left(\frac{k}{R}\right) \left(\frac{2}{k+1}\right)^{\frac{k+1}{k-1}} \right\}^{-\frac{1}{2}} , \tag{8}$$

where $\dot{m}$ is the neutral propellant flow rate, D is the orifice diameter, k is the ratio of specific heats for the vapor (assumed to be near 5/3 although the results are not sensitive to its value), and R is the gas constant. The temperature T_G is an unknown but bounds can be placed on it from consideration of the measured temperatures prevailing in the cathode. Its value should lie between the local electron temperature and some

---

* The partial pressure of the electrons increases while that of the neutrals and ions decreases as one proceeds downstream toward the orifice. This is assumed to occur in such a way that the sum of these two remains constant. In reality the total pressure is probably fairly uniform until the immediate vicinity of the orifice is approached and a slight decrease in pressure is observed.

temperature characteristic of the internal cathode surfaces. The maximum electron temperature obtained in the cathode was about 1.0 eV and cathode surface temperatures above 150°C ($\sim$ 0.036 eV) have been found necessary to prevent mercury condensation. Using these two values as bounds the pressure must lie between .75 and 4.0 torr. Hollow cathode temperature studies[25] have shown that the average temperature near the orifice is closer to $\sim$ .1 eV (880°C) so this was selected as the most probable temperature for the internal surfaces. Using this temperature and the internal pressure of $\sim$ 1.25 torr calculated on the basis of it, the electron density (n_e) and ionization fraction (α) profiles were calculated for the values of Maxwellian electron temperature shown in Figure 43 as a typical case of spot mode operation. The corresponding values of electron density are shown in Figure 44 plotted as broken lines along with the experimental data (solid lines). Values of α are plotted in Figure 45. To determine an upper bound on the density and ionization fraction they were also calculated for the case of a 1.25 torr pressure and a gas temperature equal to the local electron temperature. These are also plotted on Figures 44 and 45 as center lines.

It was apparent that similar results would not be obtained for the electron temperature profile for the plume mode shown in Figure 41 as the solid line because the line was too flat. In this case the temperature profile shown by the dotted line was assumed and the same calculations discussed above resulted in the theoretical curves indicated on Figures 42 and 46. Although the assumed (dotted) temperature profile deviates from the best fit for the data points for upstream of the orifice it is seen to agree fairly well with the data points within 10 mm of it. An error bar shown at the 7.5 mm position on the calculated curves for constant gas temperature

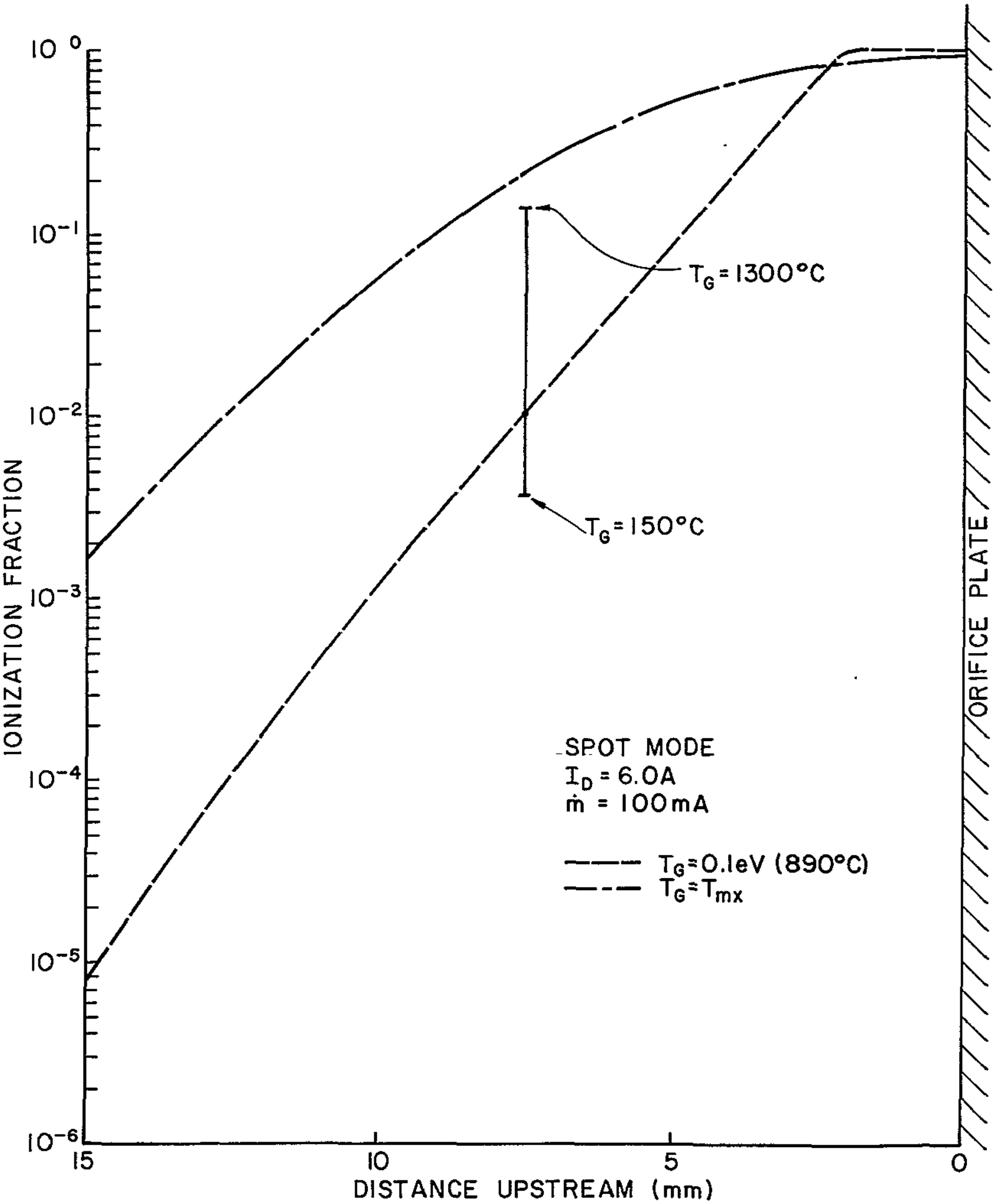

IONIZATION FRACTION PROFILES
SPOT MODE

FIGURE 45

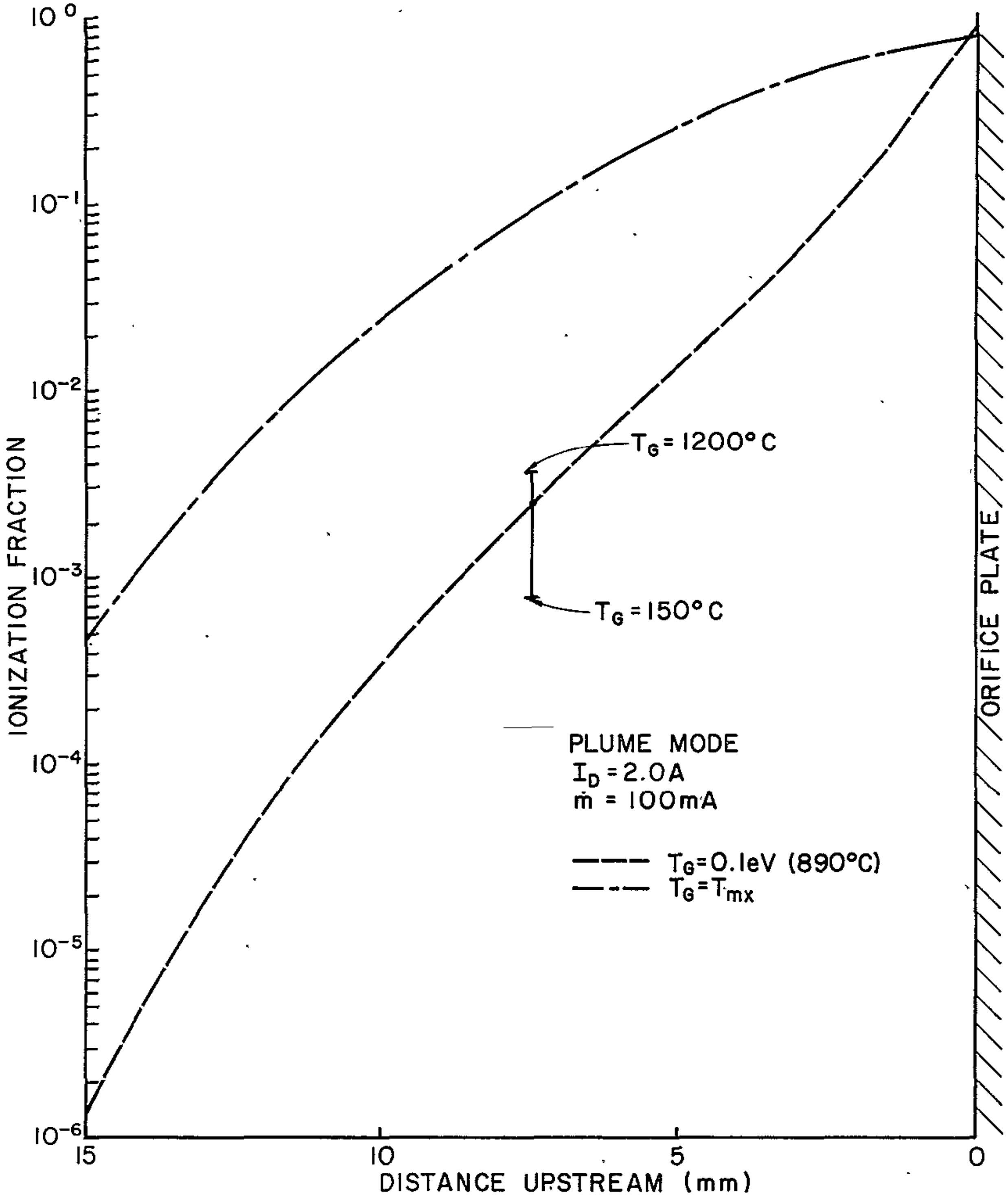

IONIZATION FRACTION PROFILES
PLUME MODE

FIGURE 46

(dashed lines) in Figures 42, 44, 45 and 46 indicates the range of density variations calculated for the cases where the neutral/ion temperature (T_G) assumes the maximum probable range of internal cathode surface temperatures.

The results of the above calculations are somewhat sensitive to the simple assumptions made regarding the magnitude and shape of the gas temperature profile and the total pressure profile in the cathode chamber. However, for such a simple model, the agreement with the experimental data is encouraging, and allowing T_G to vary should facilitate even better agreement. For example the close proximaty of the solid and dashed lines at locations more than 5 mm upstream of the orifice, suggests the ion/neutral temperature is probably about equal to the internal cathode surface temperature in this region. In this region then the ions and neutrals are not in equilibrium with the electrons. In the region zero to 5 mm upstream of the orifice there is no straightforward way to tell if the neutrals and ions are in equilibrium with the electrons. At the orifice itself however in the cases of the lower temperature T_G (dashed lines on Figs. 45 and 46) Equation (6) requires that the ionization fraction come infinitesmally close to unity. In the case where the temperature T_G is equal to the electron temperature (center lines on Figs. 45 and 46) both the shape of the curves at the approach to the orifice and the magnitudes of the ionization fractions are more reasonable (80 to 90%). This suggests that the atom/ion temperature probably increases toward the electron temperature as the orifice is approached.

The results presented in Figures 41 to 46 can now be used to gain some insight into emission mechanisms in the hollow cathode. Bessling concluded on the basis of his model that the dominant emission mechanism was thermionic-field emission in the orifice region. In order to evaluate this, note that in a plasma where the electrons and ions are at two different temperatures the Debye length, λ_D, is given by

$$\frac{1}{\lambda_D^2} = \frac{e}{\varepsilon_o}\left(\frac{n_e}{T_{mx}} + \frac{n_i}{T_G}\right) , \qquad (9)$$

where ε_o is the permittivity and n_i is the ion density and is equal to the electron density. Figures 42 and 44 suggest that at most the electron density is $\sim 1.2 \times 10^{15}$ cm^{-3}. Even assuming that the gas temperature and electron temperature differ considerably say T_G = .1 eV and T_{mx} = .8 eV the Debye length would be no smaller than 6.33×10^{-6} cm. The plasma potential in the orifice region is about 10 v. These two results combine to suggest an electric field strength at the orifice wall of

$$E = \frac{V}{\lambda_D} = 1.58 \times 10^6 \text{ V/cm}. \qquad (10)$$

This is an order of magnitude below the field strength of $\sim 10^7$ V/cm suggested by Bessling[22] as necessary for the electric field to contribute significantly to the emission. Without accounting for the possibility of locally high fields due to surface irregularities, it appears that thermionic field emission is insignificant in the orifice region.

Cathode-Insert Interaction Studies

One additional test was conducted on a hollow cathode like the one shown in Figure 35 which warrants some discussion. In this test the rolled foil insert shown in the Figure was replaced by a 1.9 mm dia. cylindrical porous tungsten insert which had been impregnated with low work function material (Semicon type 84-S). In addition the Langmuir probes were not present and the insert was attached to a wire which passed through the feedthrough to facilitate axial movement of the insert during cathode operation. A new cathode, which had never been exposed to low work function oxides and which had a 0.76 mm dia orifice was selected for the test. The upstream plate shown in Figure 35 through which the insert moving wire was fed was made of quartz for this test. The quartz window facilitated direct observation of the discharge as well as temperature measurement of the interior surface of the cathode orifice plate using an optical micro-pyrometer.

After the mercury flow rate had been stabilized into the preheated cathode, the discharge was started with the downstream end of the insert positioned 1.75 cm upstream of the orifice plate. The cathode was operated for a period of several minutes at a keeper current of 0.3 A. and a discharge current of a few amperes to allow the discharge to stabilize. The discharge current was then increased to 5 A. and the porous tungsten insert was moved toward the cathode orifice plate with the trajectory shown in the upper plot of Figure 47. It was then pulled back to the 1.75 cm position where it was held for two minutes before it was inserted and retracted rapidly as shown in Figure 47. The time variation in anode voltage and orifice plate temperature (measured at the edge of the orifice itself) which accompanied this insert movement are also shown in the figure. Although some of the times associated with the figure were estimated, the time scale is considered accurate to within $\pm$ 15 sec. and data shown as being collected at the same time were collected with a few seconds of each other.

From Figure 47 it can be seen that at the initial operating condition (a new cathode and the insert 1.75 cm from the orifice plate) the orifice plate temperature and voltage were both high ($\sim$ 1400°C and 15 V respectively).

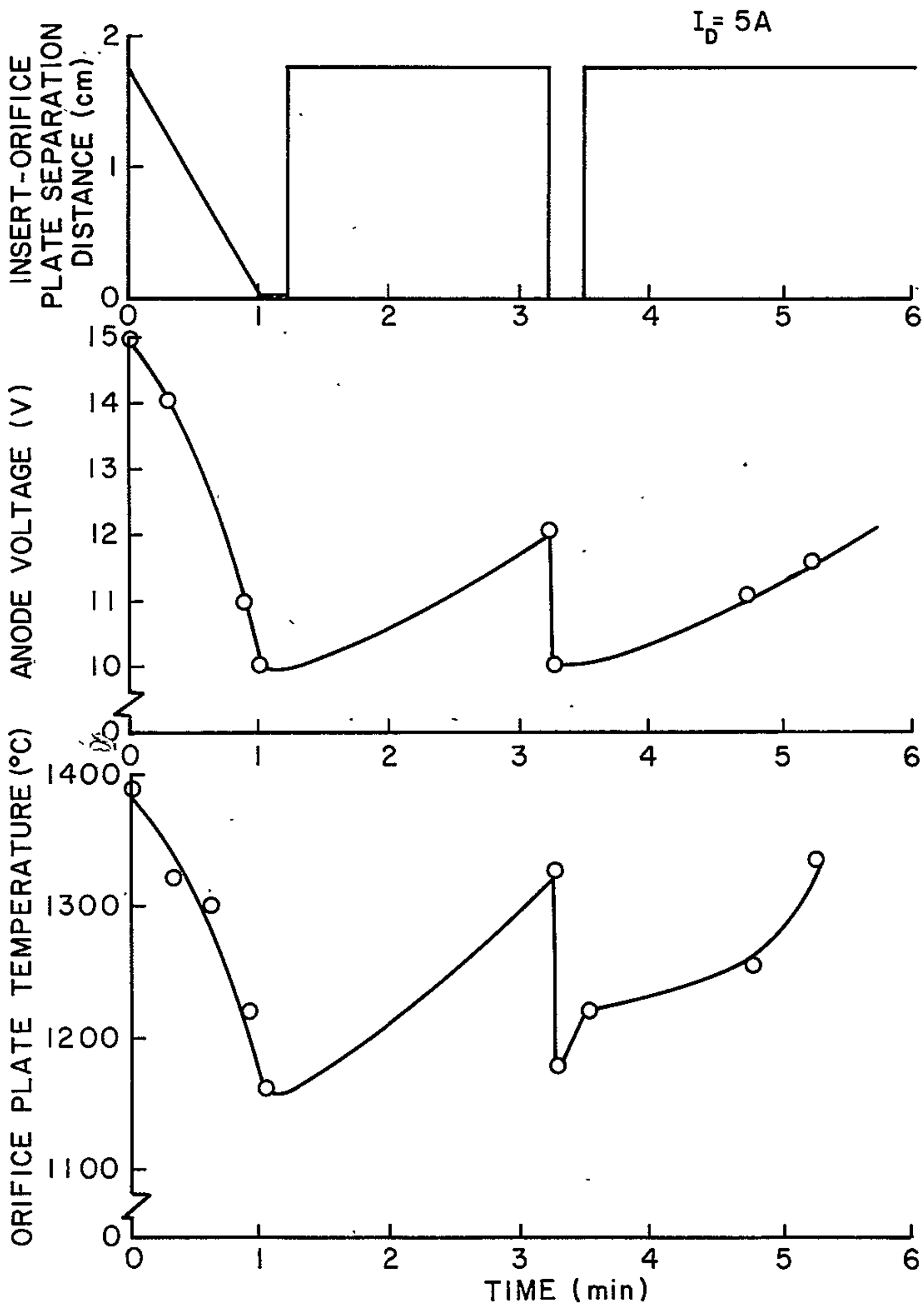

EFFECT ON INSERT POSITION ON CATHODE TEMPERATURE AND ANODE VOLTAGE

FIGURE 47

Moving the insert downstream is seen to reduce both of these quantities. Moving the insert back upstream is observed to effect a gradual increase in temperature and voltage apparently as a result of gradual depletion of the low work function material in the vicinity of the orifice. The correlation between anode voltage and temperature is striking. The temperatures shown in Figure 47 were measured at the edge of the orifice. Temperatures at the intersection between the orifice plate and cathode tube were observed to be about 100°C lower than these plotted values. After this test, the cathode was replaced with one which again had not come into contact with any low work function material. This cathode also had a 0.76 mm dia orifice but it had a dummy insert (no low work function material). It was observed to operate at orifice plate temperatures of about 1600°C and discharg voltages of 13 volts when the discharge current was 5 A. Contrary to the case with the insert-equipped cathode, where temperature gradients were observed on the orifice plate, the entire orifice plate of this second cathode appeared to be at a uniform temperature. Further, the luminosity from excited mercury atoms could be seen throughout the entire cathode support structure and into the 1/8" propellant feed tube (Figure 35). When a low work function insert was present, luminosity was not observed up stream of the insert.

Conclusions

Plasma potentials and electron temperatures appear to increase through the orifice of a cathode operating in either the spot or plume modes. Electron density profiles are very peaked in the vicinity of the orifice. The electron densities at a given location increase with discharge current in the plume mode and tend to remain constant with increases in discharge current in the spot mode.

Upstream of the orifice the measured electron temperatures and densities correlate well with calculations based on the expanded Saha equation if the neutral/ion temperature is assumed to be close to the wall temperature and the pressure in the cavity is assumed to be constant. The orifice itself appears on the other hand to be a region of a high electron collision frequency where thermal equilibrium between electrons, ions and atoms is approached. The results suggest that the ionization fraction in the orifice is high. They do not, however, suggest that thermionic-field emission is the dominant emission mechanism for the hollow cathode.

The movement of a cathode insert into a previously virgin cathode suggests that the nature of the discharge changes markedly as the availability of low work function materials in the vicinity of the orifice changes. When this material is not available discharge voltages and cathode temperatures increase greatly, and electrons tend to be drawn from surfaces far from the cathode orifice in an apparent effort to satisfy the requirement for the emission current demanded by the discharge.

8 cm THRUSTER TESTS

An 8 cm mercury ion thruster was assembled from component parts of the SIT 8 thruster[26, 27] and tested in the large (1.2 m dia. x 4.6 m long) vacuum facility at Colorado State University. The principal purpose of these tests was to determine if the doubly charged ion production model proposed by Peters[28] could be applied to discharge chambers as small as this 8 cm dia. one.

Apparatus and Test Procedure

The thruster was operated using two different sets of grids both of which employed 67% open area screens. The SHAG optics set had a 19% open area accel grid while the other one had a 44% open area accel grid. Verification of the doubly-charged ion production model required simultaneous measurement of plasma properties within the thruster and the doubly and singly-charged ion density profiles in the thrust beam. The required plasma properties were determined from Langmuir probe data[29] collected at a total of at least 16 points within the discharge chamber at each operating condition, and each of these data sets analyzed using a computer program developed for this purpose.[24] The doubly and singly-charged ion current density profiles were measured in the ion beam of the thruster using an E x B momentum analyzer.[30]

The thruster was operated at various flow rate and discharge voltage/current conditions using the two grid sets and the aforementioned data were collected. Plasma property data were next volume averaged over the primary electron region within which the bulk of the ionization is presumed to occur. This volume averaging process, which is described in detail by Peters,[31] also enables one to determine the ratios of singly and doubly-charged ion fluxes within the primary electron volume to those on its surface. These ratios are necessary for the calculation of doubly and singly-charged ion loss rates in the model.

Results

During the test sequence operation at the nominal condition was attempted to check if the source was performing as similar units had in other laboratories. Using the 19% open area accelerator grid (SHAG) it ran stably and the operating variables shown in Table I were measured. The nominal values operating variable as supplied by NASA for the SIT 8 unit are also listed for comparison.

Table I

8 cm Thruster Nominal Operating Condition

Variable	Nominal Value	As Measured
Anode-to-Neut. Potential	1205 v	1200 v
Accelerator Voltage	-300 v	-300 v
Accelerator Drain Current	0.17 mA	0.4 mA
Discharge Neutral Flow Rate	91.4 mA	90 mA
Beam Current	72 mA	73 mA
Discharge Current	0.455 A	0.60 A
Discharge Voltage	35 v	38.9 v
Keeper Current	0.1 A	0.1 A
Keeper Voltage	6.0 v	10.0 v
Cathode Heater Current	0	0
Neut. Keeper Current	0.5 A	0.5 A
Neut. Keeper Voltage	13.0 v	20 v

The most striking differences between the nominal and measured values in this table are related to the higher keeper voltage measured on both the main and neutralizer keepers. The high main keeper voltage necessitated in turn an increase in the discharge voltage so the discharge-keeper voltage difference could be maintained at a specified value of about 29 v. The reason for the higher keeper voltages is not certain, but it is believed to be related to possible contamination of the main and neutralizer cathodes an/or depletion of the low work function material which should be present in them. This is substantiated by the fact that in the first tests of these cathodes, main and neutralizer keeper voltages of 11 and 21 v respectively were observed. A subsequent attempt to add chemical R-500 through the cathode orifices reduced these voltages to about 8 and 17 v respectively. After a few hours of operation however these voltages rose to the "as measured" values given in Table I.

The "as measured" discharge current in Table I is also observed to be high. While this can be explained in part by the higher "as measured" beam current and lower discharge neutral flow rate, the discharge current is still considered high. These discrepancies were however considered sufficiently small so that the main objective of the tests (verification of the doubly-charged ion production/loss model) could be pursued.

The operating conditions at which 8 cm thruster data were collected for the verification of the doubly-charged ion model are given in the first five rows of Table II. The next row of this table indicates the volume-to-surface area ratio for the primary electron region of the 8 cm thruster as determined from iron filings maps is 0.92 cm. Following this quantity, the average plasma properties as determined from Langmuir probe traces; which had been analyzed, appropriately weighted and volume averaged; are listed. The uniformity factors which are required in the analysis are also listed. They are determined from measured properties and represent the primary electron region volume-to-surface area flux ratio for singly (F_+) and doubly (F_{++}) charged ions. Following this, the ratio of doubly-to-

Table II

8 cm Thruster Calculated Densities and Production Routes for Various Operating Conditions

	Screen/Accel Grid Open Area Percentages	67/44	67/44	67/19	67/19	67/19	67/19	67/19	67/19
Measured Operating Variables	Discharge Current (A)	.71	.26	.63	.86	.66	.60	.70	.38
	Discharge Voltage (V)	42.7	39.2	38.6	41.0	40.0	39	39	37.6
	Beam Current (mA)	66	44	73	77	72	73	75	56
	Mass Flow Rate (mA)	86	90	90	91	88	90	91	91
Measured Primary Electron Region Plasma Properties	Plasma Volume-to-Surface Area Ratio (cm)	.92	.92	.92	.92	.92	.92	.92	.92
	Avg. Maxwellian Electron Temperature (eV)	13.0	5.2	7.6	12.6	9.7	7.7	8.8	4.2
	Avg. Primary-to-Maxwellian Elec. Density Ratio	0.19	0.052	0.11	0.087	0.089	0.078	0.061	0.029
	Avg. Primary Electron Energy (eV)	29.0	24.7	27.3	23.2	19.5	21.3	19.4	20.0
	Avg. Electron Density ($cm^{-3} \times 10^{-10}$)	9.2	8.5	12.6	12.5	11.0	11.8	12.9	14.4
	Uniformity Factor F_+	2.11	1.77	1.93	1.78	1.85	1.81	1.88	1.53
	Uniformity Factor F_{++}	1.99	1.99	1.92	2.02	2.67	2.63	2.74	1.56
	Measured Doubly-to-Singly Charged Ion Current Percentage	7.96	2.0	5.4	15.4	9.5	4.6	6.2	1.5
Calculated fractions of Ions/Atoms in Various States	Neutral Ground State Atoms	.70	.64	.62	.64	.63	.61	.61	.55
	Neutral Metastable State Atoms	.033	.084	.065	.039	.055	.068	.063	.11
	Neutral Resonance State Atoms	.21	.26	.26	.26	.26	.28	.27	.32
	Singly Charged Ground State Ions	.060	.021	.055	.067	.049	.044	.054	.021
	Singly Charged Metastable Ions	.001	.000	.001	.001	.002	.002	.002	.001
	Doubly Charged Ground State Ions	.002	.000	.001	.002	.001	.001	.001	.001
Production of Singly-Charged Ions from	Neutral Ground State	.63(.27)*	.47(.32)	.50(.33)	.56(.12)	.52(.13)	.48(.18)	.49(.11)	.34(.24)
	Neutral Metastable States	.066(.25)	.19(.21)	.13(.26)	.077(.11)	.111(.12)	.14(.15)	.13(.09)	.27(.14)
	Neutral Resonance States	.31(.27)	.34(.28)	.37(.31)	.37(.11)	.36(.12)	.38(.17)	.38(.09)	.39(.18)
Production of Doubly-Charged Ions from	Neutral Ground State	.25(.037)	.093(0.)	.097(.017)	.23(0.)	.22(0.)	.14(0.)	.17(0.)	.053(0.)
	Neutral Metastable State	.012(.037)	.012(0.)	.010(.017)	.014(0.)	.019(0.)	.016(0.)	.018(0.)	.011(0.)
	Neutral Resonance State	.075(.037)	.037(0.)	.041(.017)	.094(0.)	.089(0.)	.065(0.)	.078(0.)	.030(0.)
	Singly Charged Ionic State	.66(.30)	.85(.48)	.84(.41)	.65(.13)	.67(.092)	.77(.24)	.72(.07)	.90(.43)
	Singly Charged Metastable State	.005(.22)	.004(.38)	.009(.36)	.008(.026)	.009(.034)	.009(.03)	.012(.003)	.003(.05)

* Numbers in parenthesis are the fractions of the indicated interactions effected by primary electrons.

singly-charged ion current in the beam, as determined from mass spectrometer, data are listed. Dividing each of the numbers in this row by $2\sqrt{2}$ yields the average doubly-to-singly charged ion density ratio in the discharge chamber expressed as a percentage.

The section in Table II titled "Calculated Fractions of Ions/Atoms in Various States" lists the normalized densities of the states included in the analysis and predicted by the model. The normalized density of a given specie is defined here as the specie density divided by the total heavy particle density. The sum of the normalized densities for any thruster operating condition should therefore equal unity. Table II shows, for example, that the 8 cm diameter thruster operating with the 67/44 grid set at a 42.7 v discharge voltage would be predicted to have 70% neutral ground state atoms, 21% neutral resonance state atoms, 6.0% singly-charged ground state ions and .2% doubly-charged ground state ions. The data in this section of the table are observed to be quite similar to those reported by Peters for the 15 cm and 30 cm thrusters.[28]

The last section in Table II shows the calculated production rates for singly and doubly-charged ions through the various intermediate states listed. These production rates have been normalized by the total production rate of the specie indicated. The fraction of the associated interactions effected by the primary electrons is indicated in parenthesis. For example, at the thruster's 42.7 V, 67/44 grid operating point, 63% of the single ions are produced as a result of electron interaction with neutral ground state atoms and 31% are a result of electron bombardment of neutral resonance state atoms. The neutral ground state-to-single ionic state interactions were induced by primary electrons 27% of the time and by Maxwellian electrons the remainder (73%) of the time. Again these values are relatively similar to those reported by Peters for the 15 cm diameter thruster. Comparison of the data of Table II with similar data for the 15 cm and 30 cm thruster reveals the smaller the thruster, the larger the electron temperature and the greater the fraction of the interactions that are induced by Maxwellian electrons. In all three thrusters doubly-charged ions are produced chiefly through the intermediate singly-ionized ground state.

The ratio of doubly-to-singly charged ion densities in the discharge chamber is the most important quantity generated by the analysis which produced the data of Table II. The extent to which this ratio agrees with the measured ratio is shown in Figure 48 for each of the operating points corresponding a column of Table II. Most of the data on this figure are observed to fall close to the 45° line corresponding to perfect correlation. One point corresponding to operation at the highest doubly charged ion density ratio is observed to lie significantly outside of the ± 20% error band, but in general the correlation appears to be good.

In discussing the errors in this work it is necessary to point out that the uncertainty in plasma properties, obtained from analysis of Langmuir probe traces, was observed to be significantly greater in the 8 cm thruster than it had been in the 15 cm one. It is believed that this increased uncertainty occurs because the 8 cm thruster plasma departs substantially from the Maxwellian-plus-monoenergetic distribution function that is an integral part of the probe trace analysis procedure.

Electron Acceleration Through the Baffle Aperture

A Langmuir probe was installed within the 8 cm thruster so it could be moved axially through the baffle aperture during thruster operation in the

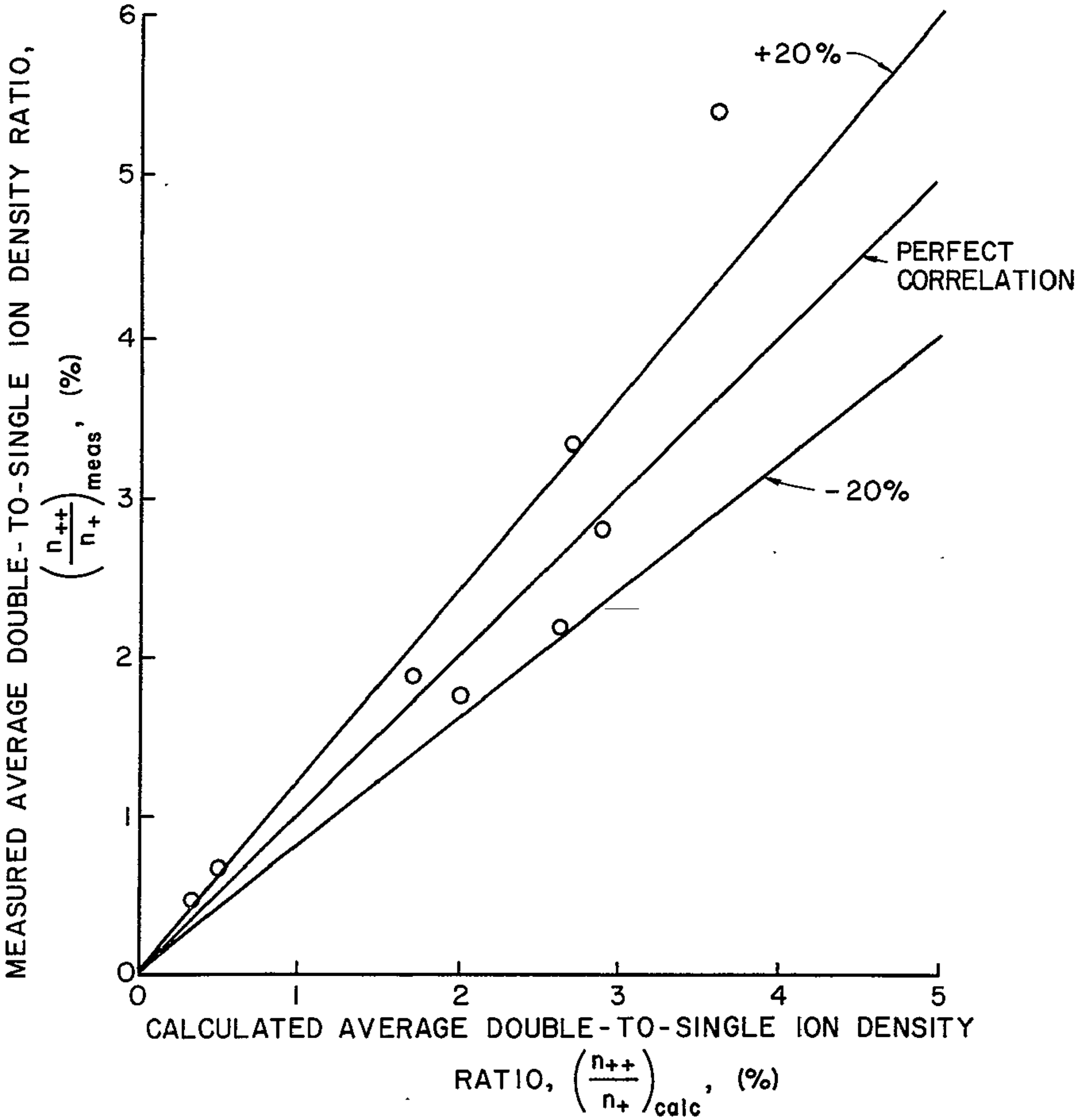

CORRELATION OF MEASURED AND CALCULATED DOUBLY-TO-SINGLY CHARGED ION RATIOS IN 8 CM THRUSTER

FIGURE 48

manner suggested by the sketch at the bottom of Figure 49. Measurements were made using this probe with the thruster operating at the conditions indicated on Figure 49 and with a 44% open area accel grid. The variation in the properties of the cathode and main discharge plasmas through the baffle aperture are also shown in Figure 49 It is considered significant that electron temperature and plasma potential show a rather steep increase 10 to 12 mm upstream of the aperture and primary electrons are observed some 6 mm upstream of the aperture. In fact it appears from the primary electron energy and plasma potential curves that the acceleration process has been completed by the time the electrons reach a position 6 mm upstream of the baffle.

These high energy electrons located upstream of the baffle can enter into reactions producing excited atoms, and singly and doubly-charged ions which will probably not escape from the cathode discharge region. These represent unnecessary energy losses which could be reduced if the electron acceleration process could be effected in the more immediate vicinity of the baffle aperture. It is believed this could be accomplished if the magnetic field lines coming from the cathode pole piece could be concentrated near its downstream edge.

Conclusions

The model for doubly-charged ion production and loss developed by Peters can be applied to the 8 cm thruster with reasonable accuracy ($\sim \pm$ 20%). The bulk of the doubly charged ions in an 8 cm dia thruster are produced from singly charged ions ionized by electrons from the high energy tail of the Maxwellian group.

Primary electron acceleration in the 8 cm thruster occurs significantly upstream of the baffle aperture.

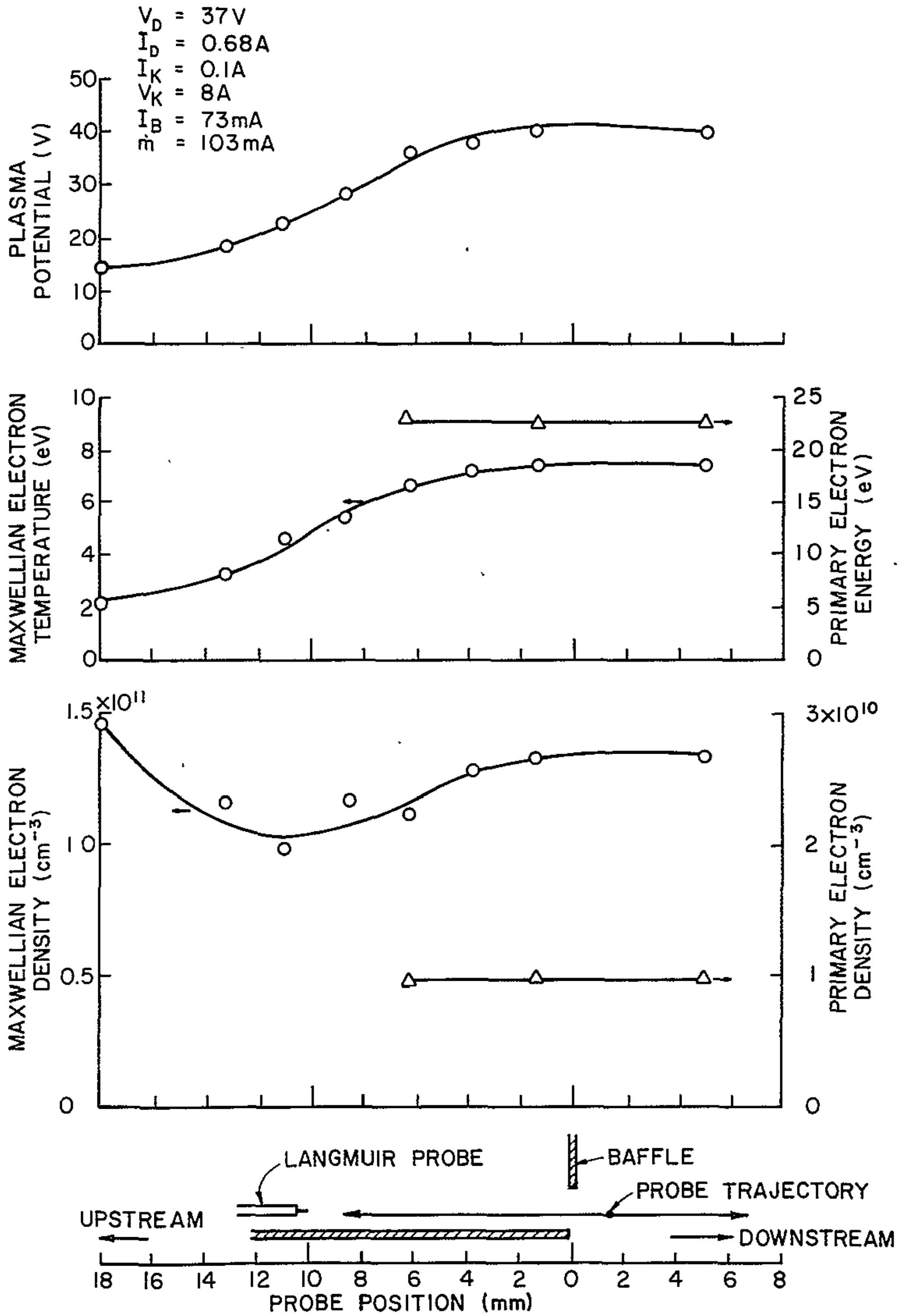

PLASMA PROPERTIES THROUGH BAFFLE APERTURE
8 cm THRUSTER

FIGURE 49

SCREEN ANODE THRUSTER

Glen Longhurst

Life tests conducted on the 30 cm mercury bombardment thruster[32] have shown screen grid erosion becomes life limiting under some thruster operating conditions. This erosion is cause by ions which are accelerated through the plasma-to-screen grid potential difference and impact on the screen grid. The bulk of the damage appears to be caused by doubly-charged ions, which acquire twice the energy of singly charged ions, as they are accelerated through a given sheath voltage drop. The sputtering yield S of a surface (atoms ejected per incident ion) in the energy range of interest here is given by

$$S \propto (E-E_0)^3 , \qquad (11)$$

where E is the incident energy of the ion (typically of order 80 eV for a doubly-charged ion) and E_0 is the sputtering threshold energy of the target material (approximately 16 eV for molybdenum). The cubic dependence of sputtering yield on energy suggests that even modest reductions in the incident ion energy will reduce the sputtering damage substantially. One method of reducing this ion energy would be to raise the potential of the screen grid to a value closer to plasma potential. Small increases in screen grid potential, such as those described previously in the "Keeper Elimination" section of this report, can be effected without changing the design chamber design and the thruster will still perform well. When the screen grid potential is increased to the point where primary electrons will have sufficient energy to pass from the plasma to the screen grid, however, the grid becomes an anode. In this case the thruster must be redesigned so its magnetic field prevents direct primary electron collection on the screen grid.

One thruster design in which the screen grid is shielded by the magnetic field is the radial field thruster design.[33] A sketch of one configuration of this thruster with an iron filings map of its magnetic field shown as Figure 50 illustrates the salient features that make it suitable for this application. Magnetic field lines are observed to pass essentially radially from the center pole piece to the outer pole piece so primary electrons emitted through the holes in the center pole piece tend to be confined between the dotted critical field lines. As the figure suggests therefore, primary electrons do not have direct access to either the screen grid or the upstream anode and both of these surfaces can be biased positive without depleting the primary electron component of the discharge plasma. The thruster is designed so the radial and axial electromagnet currents can be varied independently and so the upstream anode can be moved axially during thruster operation to facilitate thruster performance optimization. The thruster employed for these tests was 15 cm in diameter and employed a 67% open area screen grid and 54% open area accelerator grid.

Effect of Biasing Screen Grid Toward Anode Potential

Numerous changes were made in the discharge chamber design in an effort to reduce the discharge losses and increase the propellant utilization associated with its operation. Design deficiencies which resulted in poor performance in early tests, were associated with 1) the establishment of a high impedance at the point of electron acceleration into the main discharge through the holes in the center pole piece and 2) the production of a primary electron region of insufficient axial depth and

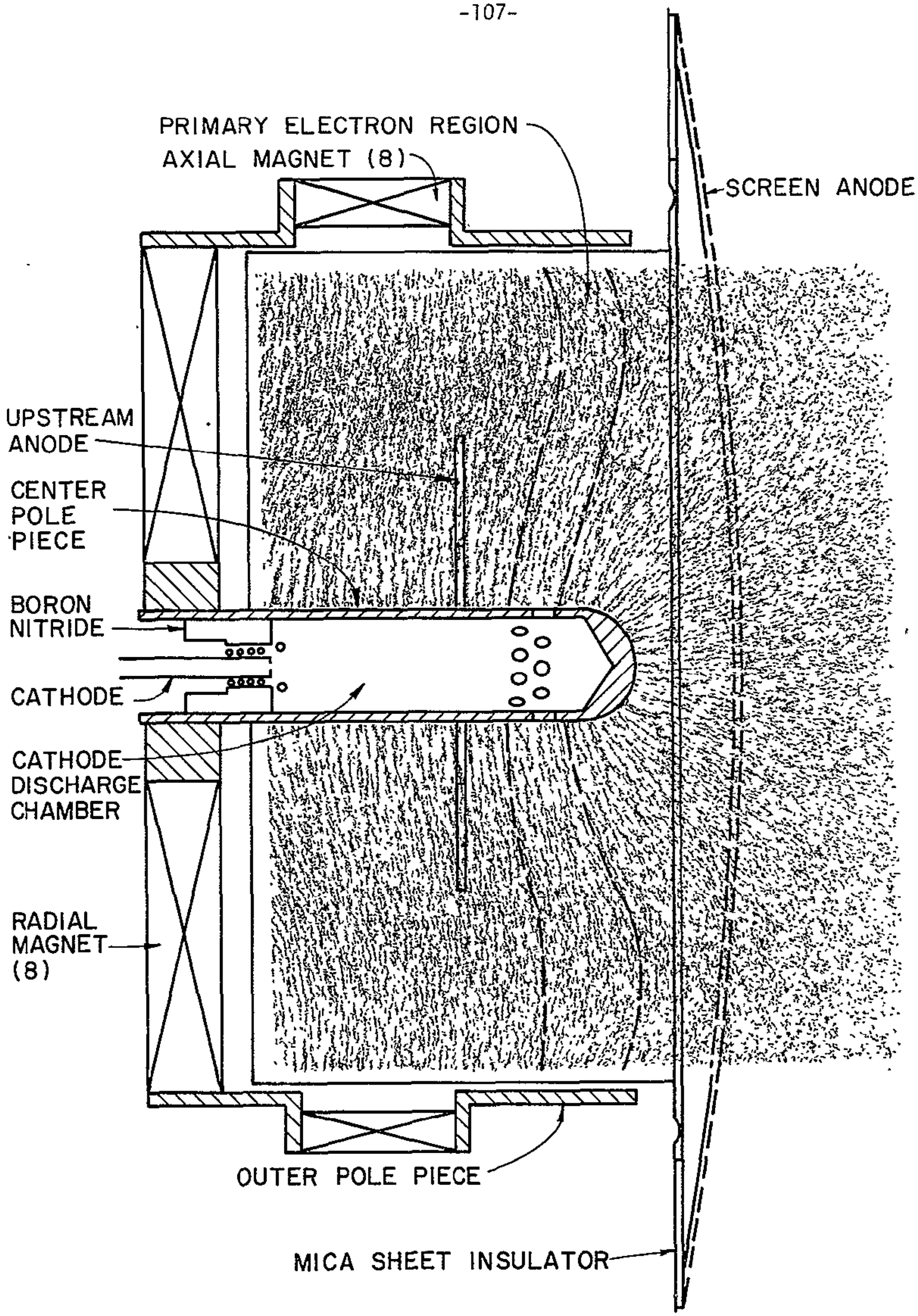

RADIAL MAGNETIC FIELD THRUSTER SCHEMATIC

FIGURE 50

uniformity to produce a high propellant utilization. While these deficiencies have not been corrected to the point where the performance is near that reported by Poeschel[34] or observed in other 15 cm thruster designs, it is considered sufficiently good to permit evaluation of the concept of screen grid biasing. Figure 51 shows the best performance curve achieved with the radial field thruster compared to that observed with the SERT II thruster[35] operating with the same grid set and at the same propellant flow rate. The solid symbols on both curves represent operation at a 37 V discharge voltage. The effect of biasing the screen grid toward this anode voltage of 37 V while holding the upstream anode voltage constant at 37 V and total discharge current constant at 4.1 A is illustrated in Figure 52. Ion beam current (and propellant utilization), discharge losses and the fraction of the discharge current carried by the screen grid are shown plotted against the screen grid bias above cathode potential. The curves show discharge losses increase and propellant utilization decreases as the screen grid bias is increased and the fraction of the discharge current collected by the screen grid increases. While this is undesirable, the data do show that this decrease in propellant utilization and increase in discharge losses is quite small until the screen grid bias is about 30 V (7 V below anode potential). This data suggests that the screen grid could be biased 10-15 V above cathode potential where sputter erosion damage would be greatly reduced without the occurrence of substantial performance degradations. Additional improvements in performance are possible with this thruster and this may change the data of Figure 52. Curves similar to those of Figure 52 have been obtained at higher discharge loss levels and this suggests that, while the entire discharge loss curve will be shifted downward and the entire beam current

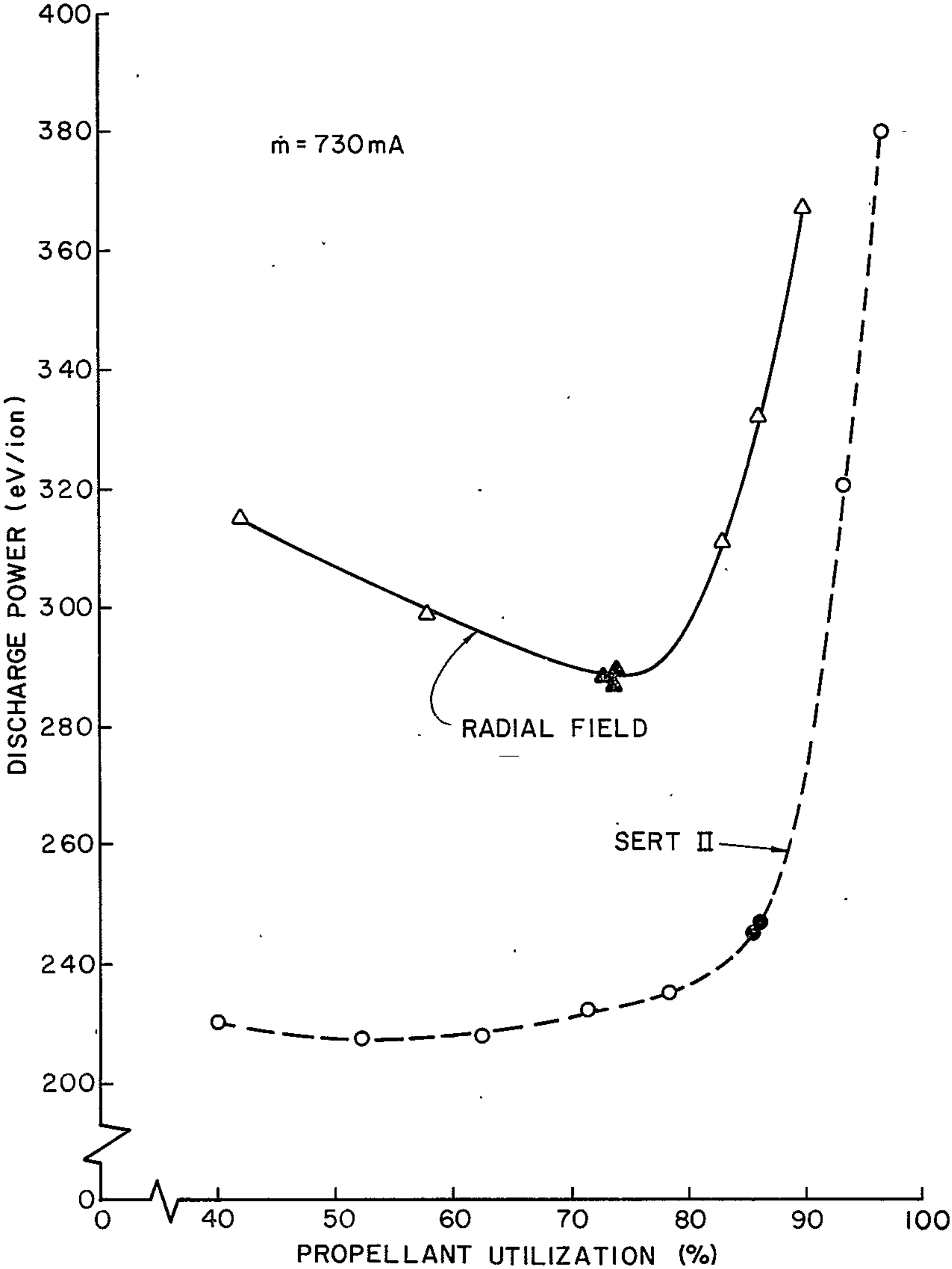

RADIAL FIELD THRUSTER PERFORMANCE

FIGURE 51

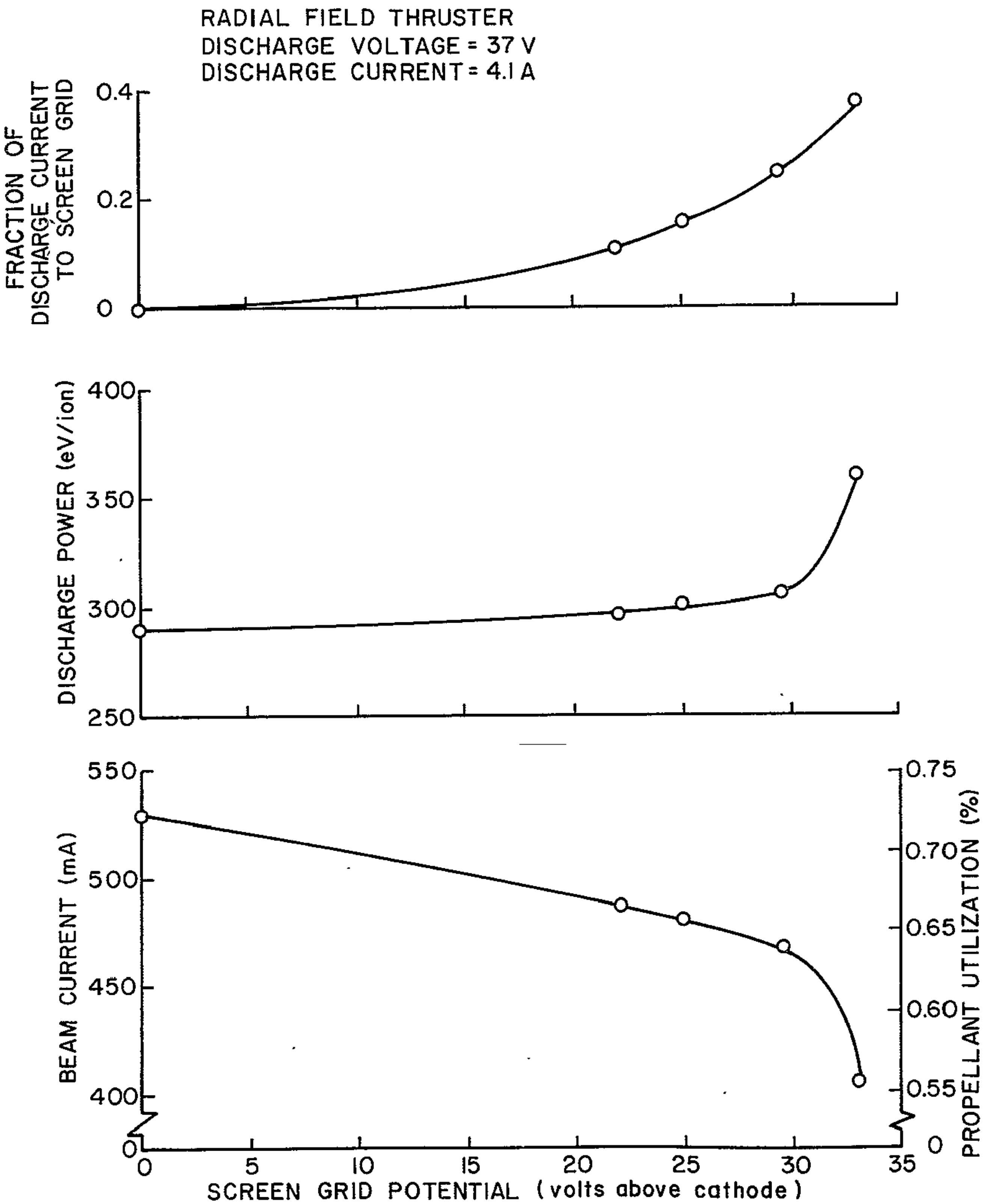

EFFECT OF SCREEN GRID BIAS

FIGURE 52

curve will be shifted upward as a result of discharge chamber improvements, the curves of Figure 52 do indicate the extent of the performance degradtion associated with biasing the screen grid. Additional tests which will focus on improving this thruster and verifying this statement are planned during the next report period.

Additional Radial Field Thruster Observations

During the course of the tests mentioned in the preceding section several features of the radial field thruster were observed which warrent discussion. First is the tendency for electrons ejected into the discharge plasma along particular field lines to tend to remain attached to those lines. This was evidenced for example in the configuration of Figure 50 as a series of luminous spokes of nearly constant diameter extending from each hole to the outer wall of the thruster. These spokes, which were most visible at high magnetic field intensities, suggest high energy electrons interact extensively along the field lines on which they are injected into the chamber before they migrate toward the anode. The fact that the spokes are of essentially constant diameter suggests that the cyclotron radius is small compared to the diameter of the holes, because the 1/r variation of the magnetic field would otherwise cause the diameter of luminous spoke to increase noticeably near the outer radius of the thruster. Numerical calculations of electron trajectories based on actual magnetic field measurements in the thruster showed that a spoke of nearly constant diameter was predicted as suggested by the filings map of Figure 50.

A discharge chamber having a configuration like the one shown in Figure 53a was made and fitted with a tungsten filament cathode which was a circular loop of constant radius located at the region of electron emission

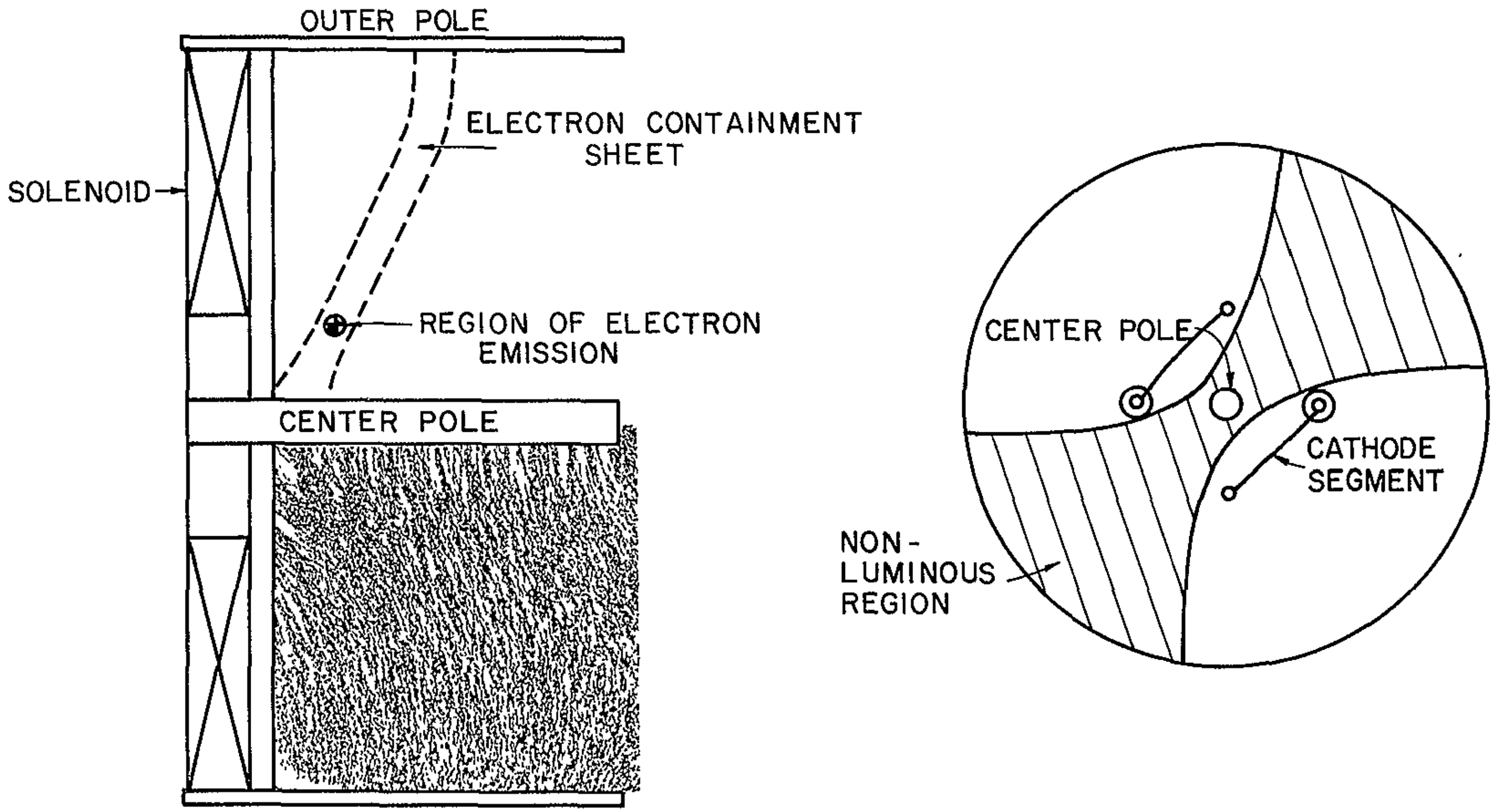

a) CIRCULAR EMISSION

b) BROKEN EMISSION SEGMENT

FIGURE 53

ELECTRON CONTAINMENT PATTERNS

identified on the figure. The loop cathode was supported in four places by screws affixed to the upstream end of the chamber. A screen at the downstream end served as the anode. The device was operated in a bell jar and a luminous sheet appeared which was azimuthally quite uniform and had a cross section similar to that shown by broken lines in Figure 53a. The thickness varied with magnetic field strength (as controlled by magnet current) but for 10 gauss radial at the outer pole piece it appeared to be about 1 cm thick. When two segments of the cathode were removed and the thruster operated under the same conditions, the luminous sheet was interrupted as shown in Figure 53b.

A second observation made on the radial field thruster was that it was very difficult to establish the desired impedance between the main and cathode discharges with the center pole piece configuration of Figure 50. Holes ranging in size from 0.3 cm dia to 0.6 cm dia were used in the pole piece and it was found that with hole diameters less than about 0.48 cm the main discharge could not be started. With this hole diameter and larger, however, the voltage drop necessary for proper thruster operation could not be sustained between the main and cathode discharge regions. Various numbers of the holes were also closed off in an attempt to increase the impedance between the main and cathode discharge regions. Making these changes in addition to adjusting the main/cathode flow rate split and upstream anode position (Fig. 50) made very little difference in the performance curve knee, which tended to lie around 500 eV/ion at 50% utilization.

It was determined that the establishment of the desired impedance between the main and cathode discharge regions necessitated the incorporation of a magnetic field across the apertures. To accomplish this the center pole piece configuration of Figure 54 was employed. With this arrangement

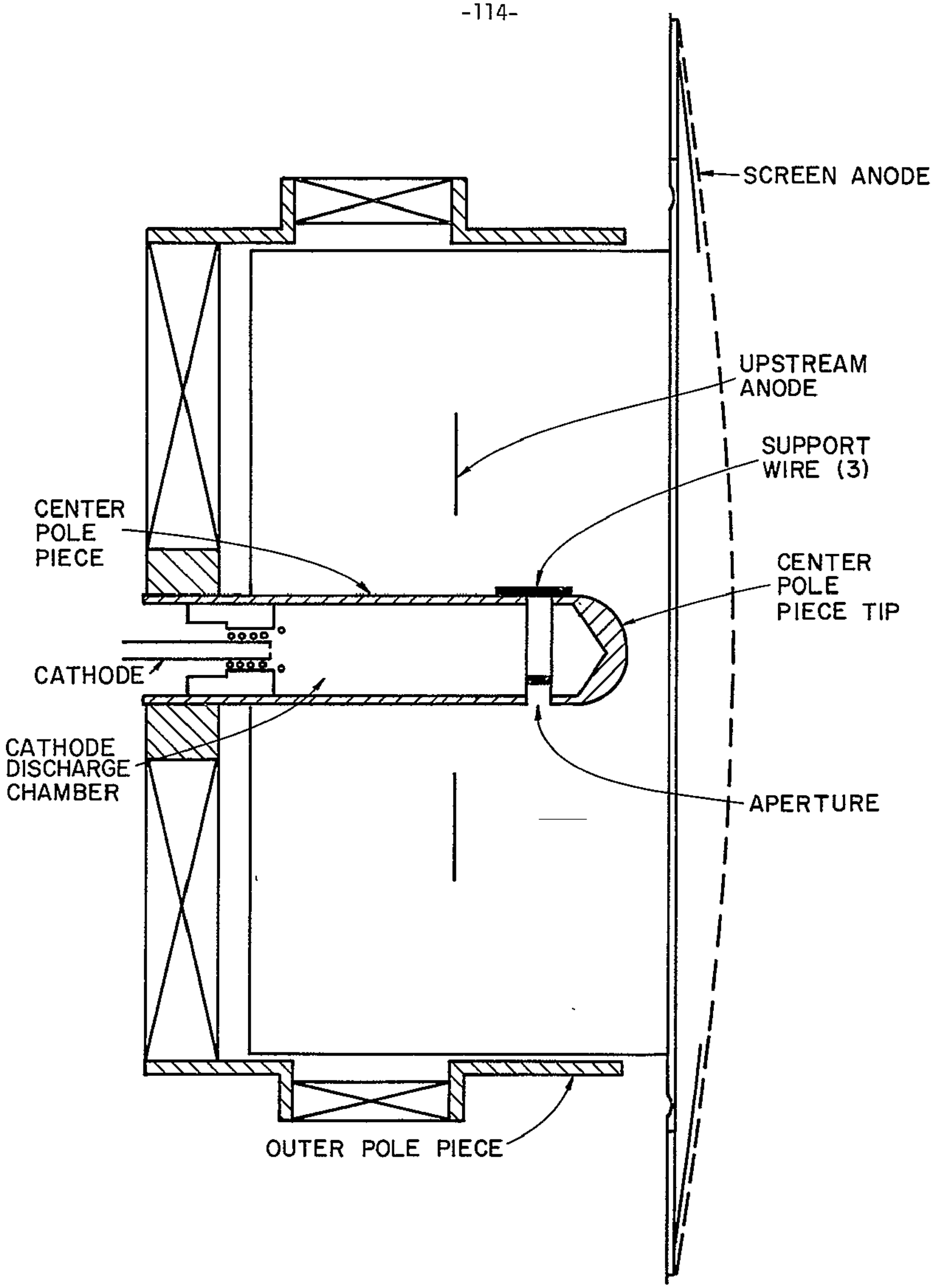

RADIAL THRUSTER/SLOT APERTURE CONFIGURATION

FIGURE 54

a magetic field was produced across the baffle aperture in such a way that it impeded electron flow from the cathode discharge region and thereby facilitated the maintenance of the desired voltage drop. Operation was attempted over a range of aperture widths and magnet current conditions and the thruster performance improved substantially over that observed with the configuration of Figure 50.

In the first design of the type suggested in Figure 54, the pole piece tip was supported by three 0.13 cm dia stainless steel (non-magnetic) wires. It was observed however that when the aperture width was sufficient to achieve the desired aperture impedance the magnetic flux passing from the center pole piece tip to the outer pole piece was reduced significantly because of the reluctance of the gap. This appeared to allow primary electron access to the screen grid when it was biased toward anode potential. To correct this, the three stainless steel wires were replaced by three ferromagnetic steel wires which saturated during operation so the magnetic field required to assure the proper aperture impedance still existed. Of several configurations of the type shown in Figure 54 which were tested, the one having an aperture width of 0.86 cm and utilizing 0.16 cm dia mild steel wire to support the tip gave the best thruster performance (that shown in Figure 51).

Further improvements in performance are considered likely in this thruster, through such changes as moving the cathode downstream into the vicinity of the aperture and possibly introducing multiple slot apertures over the length of the center pole piece. These should reduce losses associated with the cathode discharge and improve the uniformity of the primary electron distribution over the main discharge region respectively.

Thruster Stability

When this thruster was tested with the holes serving as the aperture (Figure 50) it was observed to operate fairly stably at either low magnetic fields where the discharge voltage was too low for good performance, or at high magnetic fields when the discharge voltage was excessive. During the first tests conducted with the slot aperture (Figure 54) and non-magnetic support wires it behaved similarly. In these instances the discharge tended to become more stable as the screen grid was biased closer to the anode potential. The stability did not seem to be affected by which magnet (radial or axial) was being used to produce the field. In fact both stability and performance appeared to be the same when the magnetic field level in the discharge chamber reached given values, independent of whether the field was produced by the axial magnets, the radial magnets or some combination of the two.

When the slot aperture with ferromagnetic support wires was used, the thruster operated quite stably over the full range of magnet currents. Stability was observed however to be enhanced through the use of the axial magnets in preference to the radial ones. Biasing the screen grid toward anode potential did not appear to enhance stability in this case.

THE DIFFUSION AND COLLECTION OF ELECTRONS IN ION THRUSTERS

Glen Longhurst

The stream of high energy electrons, which conveys ionization enery into the main discharge of electron bombardment thrusters, is accelerated into this discharge by the potential difference which exists between the cathode region and the main plasma. These primary electrons are generally assumed to be monoenergetic and to be confined to a region bounded by the surface of revolution of the critical field line.[36] This line is defined as the one passing from the outer edge of the cathode pole piece to the anode pole piece. Generally one would expect primary electrons to be bound to lines which pass through or very near the aperture where these electrons enter the main discharge. For hollow cathode thrusters this aperture is between the baffle and the cathode pole piece wall, and it has an annular shape like the dotted surface shown in Figure 55a. From this figure it can be seen that true primary electrons (those which have had no energy altering collisions) should be confined to the region between the surfaces of revolution of the magnetic field lines intercepting the baffle aperture at its inner and outer edge. In the model being suggested here the primary electrons move back and forth along field lines and are reflected at the baffle aperture and downstream end of the discharge chamber by the electric fields that exist at these locations.

Eventually true primary electrons have collisions, their energies are altered, and they can move off of the field lines on which they were located initially. Although the electrons may radially move in or out, the net drift is radially outward into the "collisional migration region" of Figure 55a, which again has its shape determined by the shape of magnetic

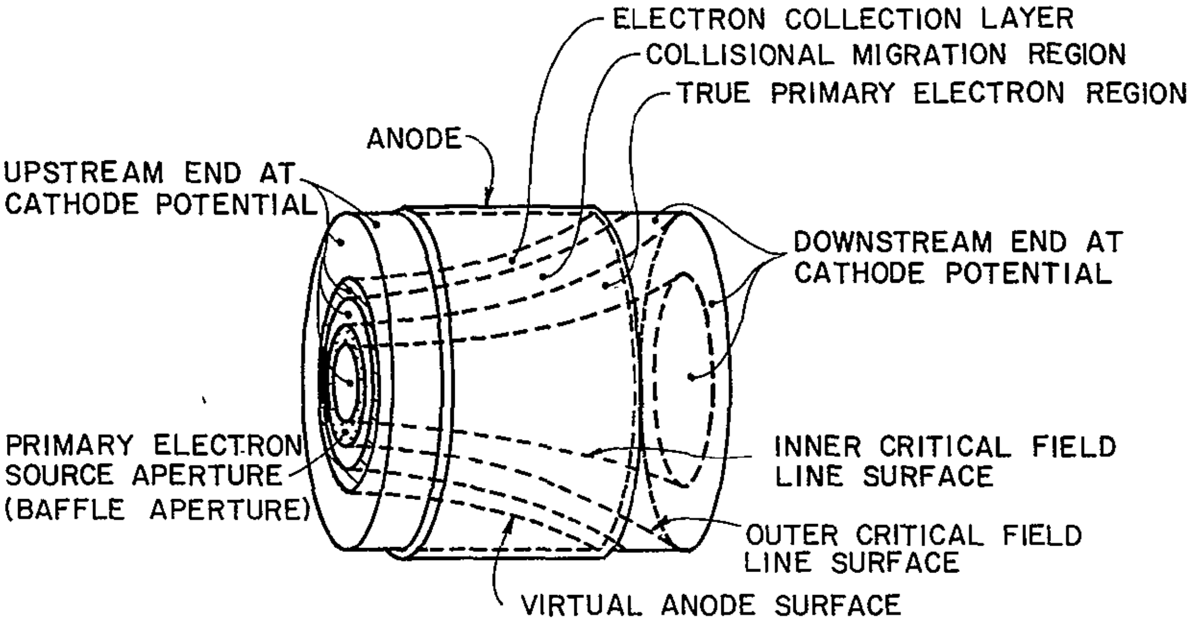

a) DIVERGENT MAGNETIC FIELD CONFIGURATION

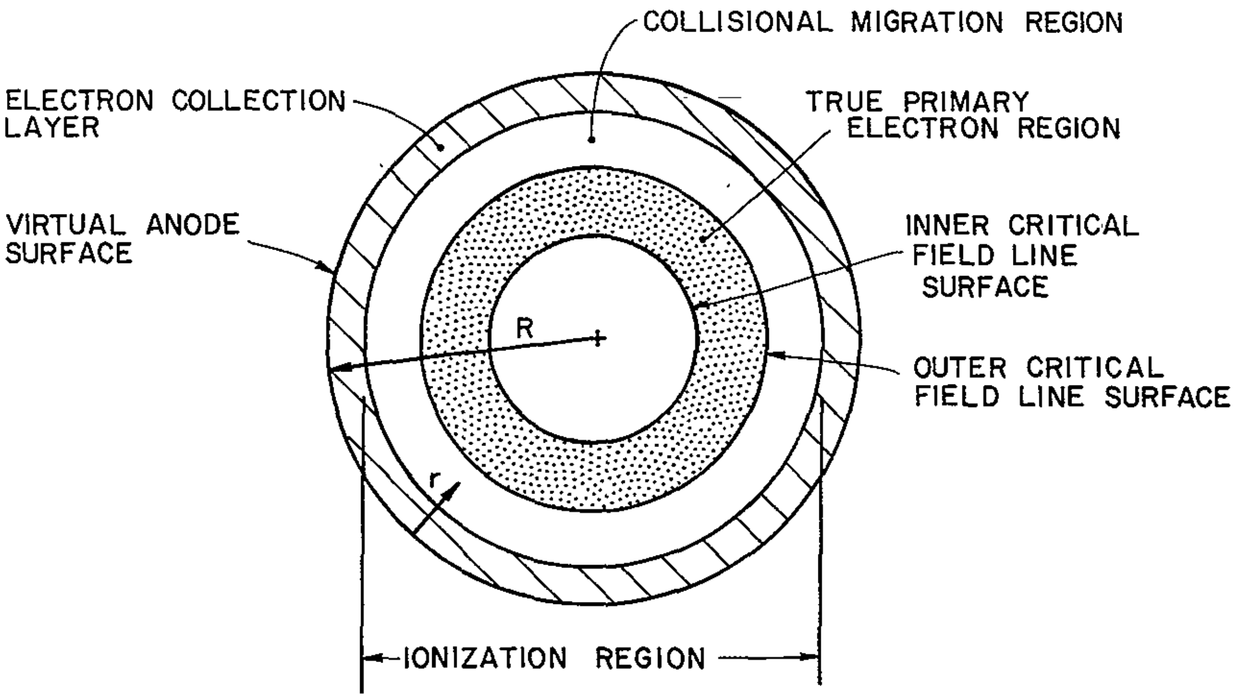

b) SIMPLIFIED GEOMETRY

THRUSTER PHENOMENOLOGICAL SCHEMATIC

FIGURE 55

field lines. This is the region through which the electrons must pass to reach the "electron collection layer" from which they can be taken to the anode. The outer surface of this layer is the surface of revolution of the magnetic field line that intercepts the anode. The electron collection at the anode is of course necessary to allow a continuous stream of primary electrons to feed energy into the plasma while preserving plasma neutrality. The electrons, which pass through the "collisional migration region," continue to move readily along field lines while being reflected at end surfaces and they are assumed able to move across field lines only as a result of collisions. With each collision the electrons lose energy, and so one would expect to see the primary electron energy distribution function change from a monoenergetic one in the "true primary electron region" to a lower average energy and move widely spread distribution in the "electron collection layer." In this region the electrons probably have a distribution function that is essentially Maxwellian. It is important to note that this proposed model, the restriction to electron migration is across field lines. The processes by which these lower energy electrons migrate to the anode and are subsequently removed from the plasma are of interest because they govern the discharge current which can be supplied and the rate at which energy supplied by the discharge current is carried to the anode by the electrons.

Plasma Properties along Magnetic Field Lines

If one can assume that electrons undergo essentially unrestricted motion along magnetic field lines compared to that across them, then analysis of the electron migration problem is greatly simplified. The assumption appears valid because the collision frequency is generally small compared with the cyclotron frequency of electron motion around the magnetic field lines. As a result electrons traverse the length of the magnetic field line to which they are bound several times before having a collision. Further it is observed that where magnetic field lines through the plasma intersect only surfaces which are at cathode potential, electrons bound to those field lines and arriving at the plasma boundary, will be reflected back into the plasma. This is the case for all of the regions identified in Figure 55a except the electron collection layer. There, electrons arriving at the anode potential plasma boundary with momentum normal to the boundary surface great enough to overcome the sheath potential will be collected by the anode and removed from the electron population.

The relative freedom of electron motion along magnetic field lines implies that intensive electron properties should be uniform along field lines. To check the validity of the assumption, lines of constant Maxwellian electron temperature were plotted and compared with the associated magnetic field configuration for three different thrusters. These were the axial and divergent (SERT II) field configurations tested by Knauer[37] and the cusped magnetic field (CMF) thruster tested by Beattie.[38] These comparisons are shown in Figure 56 where constant Maxwellian electron temperature lines are solid while magnetic field lines of force are broken. Although the configurations are not congruent, qualitative agreement is quite good considering errors inherent to Langmuir probe positioning and trace analysis and the linear interpolation of the resulting plasma property data.

Figure 57 shows a similar comparison for the Maxwellian electron density. Here constant density lines (solid) are compared with the same magnetic field lines (broken). Again the broken and solid lines show

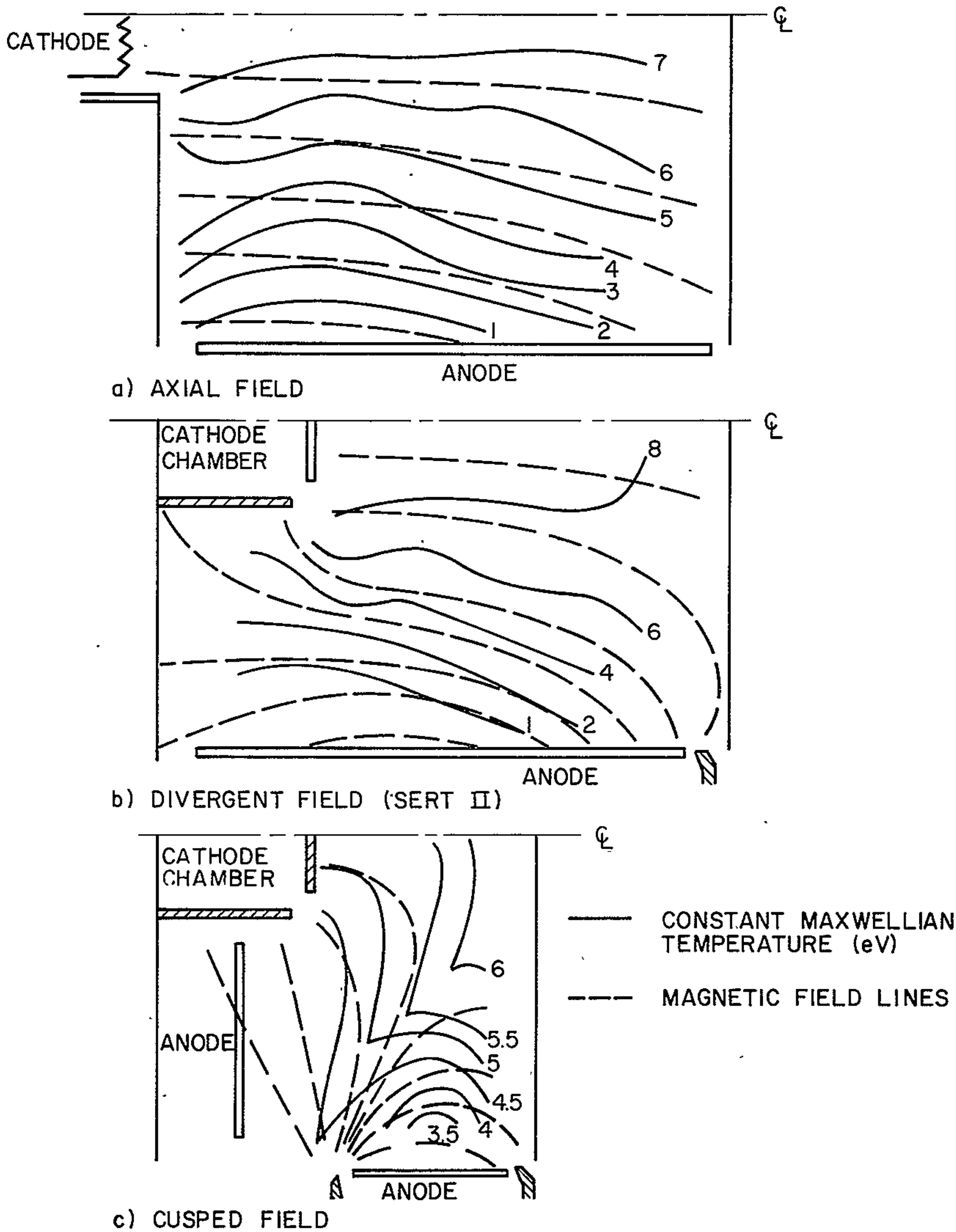

CORRELATION OF MAXWELLIAN TEMPERATURE CONTOURS
WITH MAGNETIC FIELD LINES-OF-FORCE

FIGURE 56

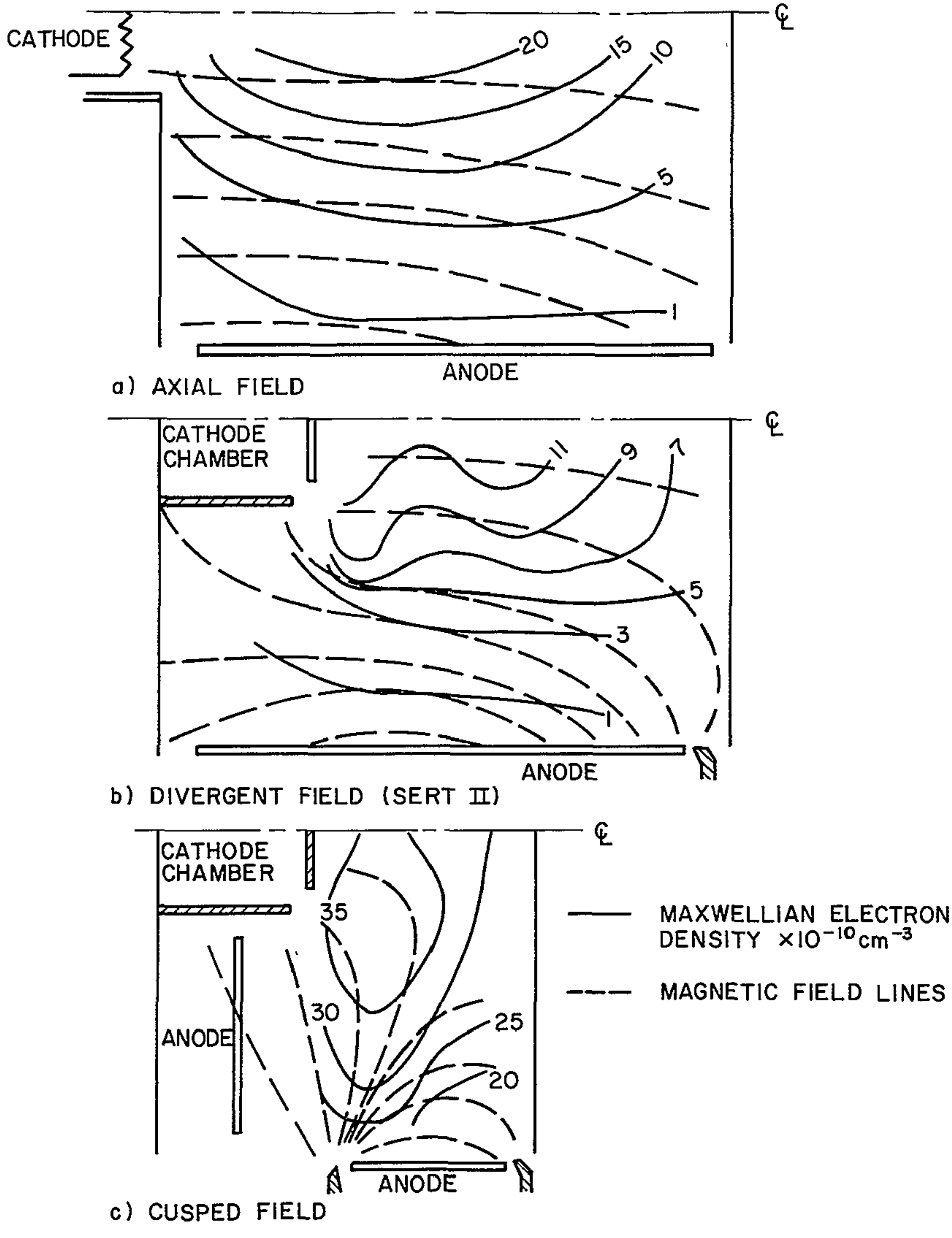

CORRELATION OF MAXWELLIAN ELECTRON DENSITY CONTOURS
WITH MAGNETIC FIELD LINES-OF-FORCE

FIGURE 57

reasonable congruency when one considers the fact that a decrease of density in regions of diverging magnetic field is expected. This is expected because the electrons tend to be bound to field lines, and as the field lines separate, the density of electrons should diminish.

Because the intensive electron properties tend to be constant along magnetic field lines, it is possible to simplify two-diminsional geometries such as the one of Figure 55a to the one-dimensional configuration shown in Figure 55b. In the simplified model the magnetic field is assumed to be uniform and normal to the plane of the figure. The virtual anode surface shown in Figure 55a is the surface of revolution of the innermost magnetic field line which intercepts the anode. It becomes a circle in the one-dimensional model (Figure 55b). The greater mobility of electrons along field lines than across them implies that only a few electrons will be diverted by collisions to orbit field lines outside the virtual anode surface before they are collected by the anode. That this is so is supported by the low plasma densities measured outside the virtual anode surface and by the observation[39] that nearly all of the anode current is drawn to that region of the actual anode where it is closest to the virtual anode surface (downstream end in the case of Figure 55a). It is noted in passing that thrusters in which the primary electron region overlaps the electron collection layer exhibit poor performance due to the loss of primary electrons before they can ionize neutral propellant atoms.

Electron Diffusion through the Collisional Migration Region

The electron current density J_e to the electron collection layer should be describable by classical diffusion theory.[40]

$$\frac{\vec{J}_e}{e} = - D\nabla n_e + \mu n_e \vec{E} \tag{12}$$

where e is the electron charge, n_e the electron density, D the diffusivity, μ the electron mobility, and $\vec{E}$ the local electric field. Assuming the plasma potential gradients are small inside the electron collection layer, the steady-state electric field $\vec{E}$ is negligible. Neglecting the second term on the right, Equation 12 becomes for the simplified model of Figure 54b

$$\frac{J_e}{e} = -D \frac{dn_e}{dr} = \frac{I_A}{e\, A_A'} + \frac{J_i}{e} \quad . \tag{13}$$

Here I_A is the net electron current drawn by the anode, A_A' is the area of the virtual anode surface, J_i is the ion current density to the actual anode as determined from the Bohm criterion for a stable sheath, and e is again the electronic charge. Using measured density gradients (dn_e/dr) across the "collisional migration regions" of the three thrusters considered in Figures 56 and 57, values of D required to satisfy Equation 13 were computed. These are listed as measured diffusivities in Table III.

Classical theorgy gives the electron diffusivity (D_L) across the weak magnetic field of a laminar plasma as

$$D_L = \frac{T_{mx}\, m_e}{e\, B^2} \tag{14}$$

where T_{mx} is the electron temperature (eV), m_e is the electron mass, e is the electronic charge, and B is the magnetic field intensity. The electron collision frequency ν is approximated by

$$\nu = (n_e \sigma_e + n_o\, \sigma_o + n_+\, \sigma_+)\, \overline{U} \tag{15}$$

where n_e, n_o, n_+ are the densities of electrons, neutrals and ions, respectively and where the corresponding σ's are total collision cross sections with those species for electrons with an average speed $\bar{U}$. It is assumed that

$$\bar{U} = \left(\frac{8eT_{mx}}{\pi m_e} \right)^{\frac{1}{2}} \quad . \tag{16}$$

Table III. Ion Thruster Diffusivities

Thruster	Diffusivity ($m^2\ sec^{-1}$)		
	Measured	Laminar	Bohm
Axial Field	26	0.8	50
Divergent Field (SERT II)	275	1.64	173.6
Cusped Magnetic Field (CMF)	117	7.5	65.8

Using measured values of plasma properties near the electron collection layer in the above equations, D_L for each of the thrusters under consideration was calculated. These values are listed as laminar diffusivities in Table III. They are observed to be lower than the "measured" values by about two orders of magnitude.

It has been observed that the laminar diffusion model does not accurately account for electron current densities observed in plasmas similar to those under consideration here.[41, 42, 43, 44] Bohm[45] has suggested that the equation

$$D_B = \frac{T_{mx}}{16\ B} \quad , \tag{17}$$

which was empirically obtained from a variety of data be used. The Bohm diffusivities were calculated for the three thrusters considered, and values appear in Table III. The agreement with "measured" values is observed to be considerably better than for laminar diffusivity calculations. According to Bohm, Equation 17 is only accurate to within a factor of 2 or 3 and this is indeed the sort of agreement between "measured" and "Bohm" values in Table III.

Departure from "laminar" diffusion to what has been called "turbulent" diffusion by Bohm[45] and others[40, 42, 43] is generally attributed to plasma instabilities. Analyses of such instabilities lead to several different modes of plasma oscillations depending on the nature of the plasma and associated magnetic fields. One such mode predicts an azimuthal component of an oscillating electric field. This component of the electric field reacts with the generally axial magnetic field to produce radial drift. The modes actually present in thruster plasmas remain to be verified before a conclusion can be drawn regarding the mechanism of electron diffusion with the plasma.

Electron Collection at the Anode

When electrons reach the electron collection layer of Figure 55a they become subject to the collection process. The one-dimensional model of Figure 55b is again assumed to apply. For mathematical simplicity the distance variable r is measured from the virtual anode surface as shown.

In this single dimension the helical motion of electrons around magnetic field lines is observable only as a sinusoidal oscillation in time, as suggested by Figure 58. The period of this oscillation would be

$$\tau = \frac{2\pi m_e}{eB} \quad . \tag{18}$$

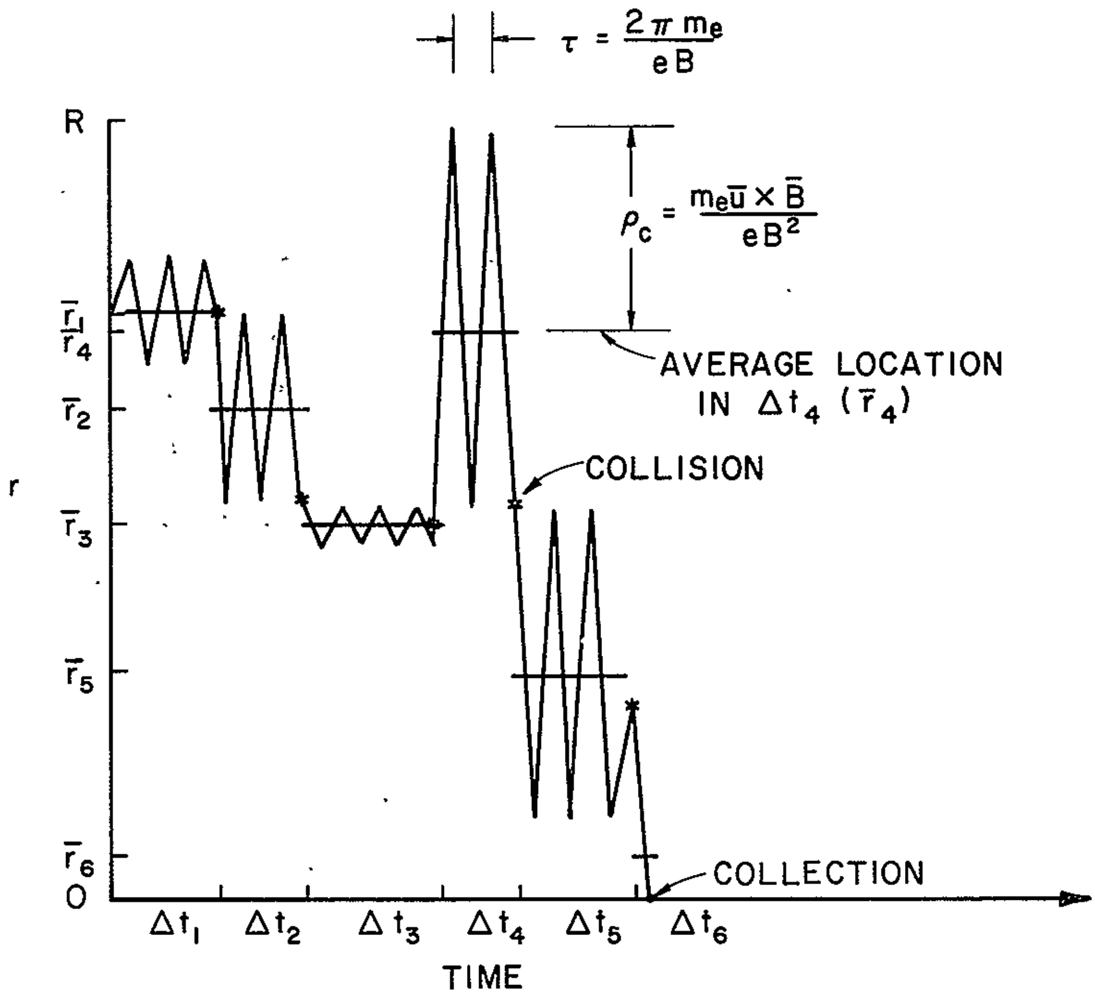

ONE-DIMENSIONAL ELECTRON MIGRATION TO ANODE

FIGURE 58

Again m_e is the electron mass, e is its charge, and B is the magnetic field intensity. The amplitude of the oscillation, which represents its maximum excursion from its average location $\bar{r}$, is the Larmor radius

$$\rho_c = \frac{m_e U \sin\theta}{eB} \tag{19}$$

where U is the electron's speed and θ is the angle between the velocity vector and the local magnetic field vector. This angle is constant over the interval of time between collisions and is not altered by specular reflections from cathode potential surfaces. The average location $\bar{r}$ is identically the location of the magnetic field line which is the electron's guiding center during some time interval Δt. As an electron has collisions, the location of its guiding center changes randomly and discontinuously as suggested by Figure 58. By defining a differential volume element per unit length to be

$$d\left(\frac{\forall}{L}\right) = 2\pi\ (R-r)\ dr \tag{20}$$

where R is the radius of the virtual anode surface, electrons may be said to become residents of $d(\forall/L)$ when their average locations $\bar{r}$ fall between r and r + dr.

If as a result of collisions an electron becomes bound to a field line which is at most one Larmor radius away from the virtual anode surface, then under the assumption that its collision frequency is much less than its cyclotron frequency, it will travel along that field line until it comes near the actual anode. If it has sufficient momentum to overcome the sheath potential which exists there, it will be collected by the anode. As a result of this collection process one would expect the electron energy distribution function measured within the electron collection layer to be deficient in electrons with sufficiently high energies to be collected.

The collection process can be quantified if one can determine the probability of electron collection in terms of the electron's average location $\bar{r}$ and its kinetic energy ε. Let the potential difference between the plasma near the anode and the anode itself be V_s. It will be assumed here that the plasma is more positive than the anode making V_s positive (this is generally the case in ion thrusters). V_s is usually 1-5 V. Because the Debye length for thruster plasmas is so short, usually of order 10^{-5} m, the sheath thickness may be neglected. Anode curvature may also be neglected so that the critical distance from the anode r_c to a magnetic field line from which an electron with Larmor radius ρ_c can be collected is shown in Figure 59. The radial component of electron momentum when it encounters the sheath must be sufficient to carry it across the sheath. This criterion for collection then becomes

$$\frac{m_e}{2} (U \operatorname{Sin} \theta \operatorname{Sin} \alpha)^2 > eV_s \quad , \tag{21}$$

where the angle α as shown in Figure 58 is given by

$$\alpha = \operatorname{Cos}^{-1}\left(\frac{r_c}{\rho_c}\right). \tag{22}$$

Substituting Equation 22 into Equation 21 gives

$$\frac{m_e U^2}{2} \operatorname{Sin}^2\theta \left(1 - \frac{r_c}{\rho_c}\right)^2 > e\, V_s \ . \tag{23}$$

The greatest distance r_{max} from which an electron having energy $\varepsilon = \frac{m_e U^2}{2}$ can be collected corresponds to the case when with speed U the electron is moving at right angles to the field vector ($\sin \theta = 1$), and from Eqn. 23 it is given by:

$$r_{max} = \frac{m_e U}{eB} \left(1 - \frac{e\, V_s}{\varepsilon}\right)^{\frac{1}{2}} \tag{24}$$

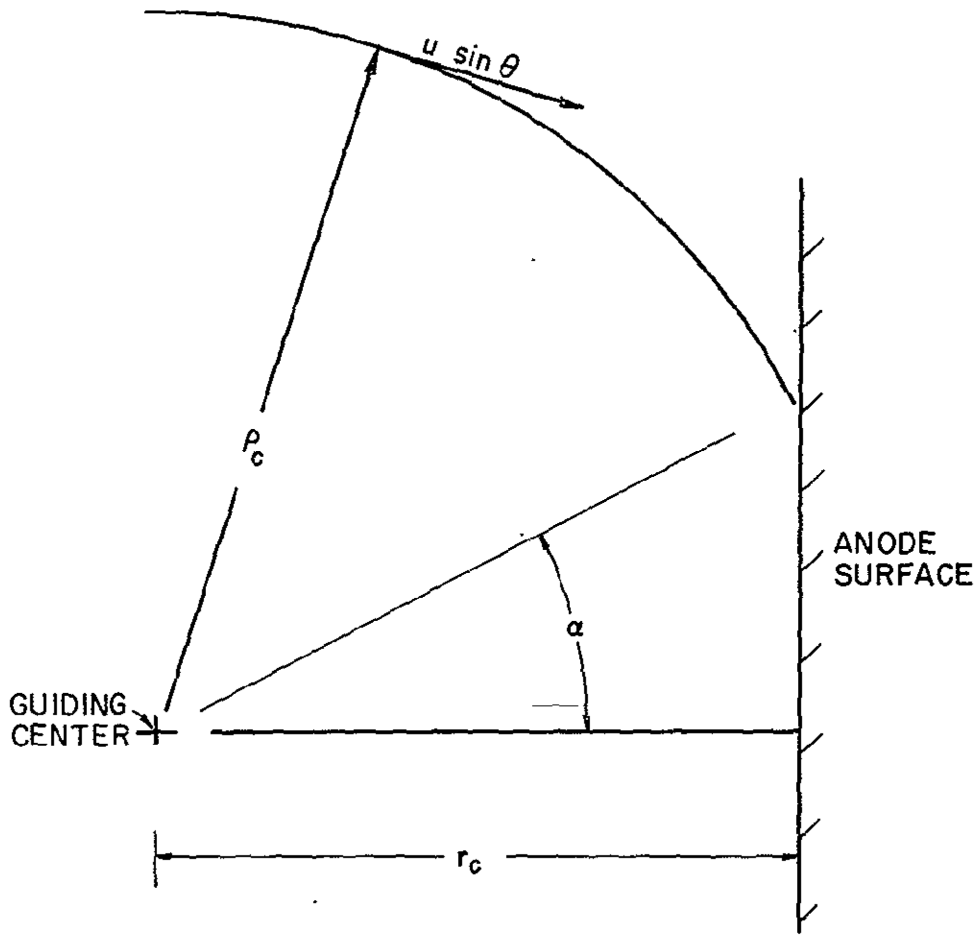

ELECTRON COLLECTION AT ANODE

FIGURE 59

If one uses the maximum velocity at which significant numbers of electrons are present, then this equation defines the thickness of the electron collection layer.

If one now considers electrons having an energy $\varepsilon = \frac{m_e U^2}{2}$ which are at a location r (less than r_{max}) then Equations 19 and 23 combine to reveal that only those electrons having an angle θ between their velocity vectors and the field vector given by the following will be collected:

$$\text{Sin } \theta > \left(\frac{(erB)^2}{2\varepsilon m_e} + \frac{e V_s}{\varepsilon} \right)^{\frac{1}{2}} \tag{25}$$

Assuming an isotropic distribution of velocity vectors at all values of r, the fraction of electrons with energy ε which will be collected from location r is called f(εr) and it is given by

$$f(\varepsilon,r) = 2 \int_{\theta^*}^{\pi/2} \frac{2\pi\ U^2 \text{ Sin } \theta \ d\theta}{4\pi\ U^2} = \text{Cos } \theta^* \ , \tag{26}$$

where θ^* represents the minimum angle between the velocity vector and the magnetic field vector for which collection is possible. From Equation 25 θ^* is given by

$$\theta^* = \text{Sin}^{-1} \left(\frac{(erB)^2}{2\varepsilon m_e} + \frac{e V_s}{\varepsilon} \right)^{\frac{1}{2}} . \tag{27}$$

Using Equation 26 and letting

$$\varepsilon^*(r) = \frac{(erB)^2}{2\ m_e} + e\ V_s \tag{28}$$

be the minimum kinetic energy for collection at average location r in magnetic field B with sheath potential V_s, one obtains

$$f(\varepsilon,r) = \begin{cases} \sqrt{1 - \frac{\varepsilon^*(r)}{\varepsilon}} & \varepsilon > \varepsilon^* \\ 0 & \varepsilon \leq \varepsilon^* \end{cases} \tag{29}$$

In the event that V_s is negative, all electrons arriving at the anode sheath would be attracted to the anode and hence would be collected. In that case Figure 59 would show $\alpha = 0$ and $r_c = \rho_c$. This causes the term $e\,V_s$ in Equation 28 to vanish.

The application of Equation 29 to the electron collection process can be best illustrated by an example. Suppose that in a particular thruster, electrons in the vicinity of the electron collection region were described by the Maxwellian distribution function

$$g(\varepsilon) = \frac{2}{\sqrt{\pi}\, eT_{mx}} \left(\frac{\varepsilon}{eT_{mx}}\right)^{\frac{1}{2}} \exp\left(-\frac{\varepsilon}{eT_{mx}}\right) . \tag{30}$$

If the temperature of these electrons was 5 eV then the distribution of electrons would be as shown by the solid line of Figure 60. At locations close to the virtual anode surface, however, a fraction $f(\varepsilon,r)$ of the electrons would be removed from the distribution function so the distribution function of the remaining electrons would be given by

$$g(\varepsilon,r) = g(\varepsilon)\,[1-f(\varepsilon,r)] . \tag{31}$$

Assuming now that $V_s \approx 0$ and $B = 13$ gauss, $\varepsilon^*(r)$, $f(\varepsilon,r)$, $g(\varepsilon)$ and $g(\varepsilon,r)$ can be calculated from Equations 28, 29, 30, and 31 respectively for various values of r. The results of doing this are shown in Figure 60. Infinitely far in from the anode ($r = \infty$) the distribution function is Maxwellian. At a distance 1 cm from the anode, the distribution function is Maxwellian for energies less than about 14 eV and beyond this point some of the electrons

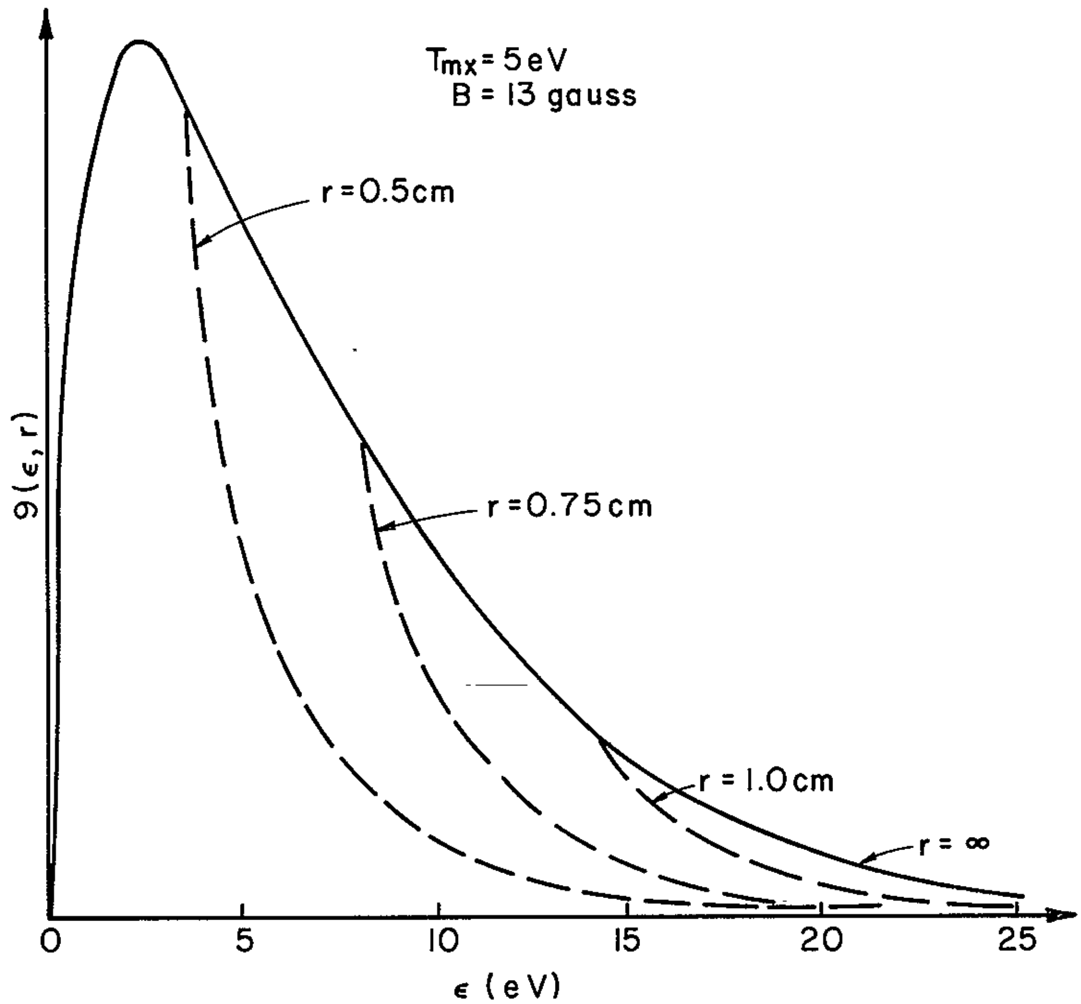

ELECTRON DISTRIBUTION FUNCTION NEAR ANODE

FIGURE 60

in the high energy tail have been removed as suggested by the dashed line. As one gets closer to the anode (r = 0.75 and 0.5 cm) more of the electrons are removed and the cutoff energy ε^* extends to lower values.

SIZE/SPECIFIC-IMPULSE SCALING RELATIONSHIPS

H. R. Kaufman

In view of the fact that ion thruster costs tend to scale with the number of components rather than their size, it is probably more cost effective to use one large thruster rather than several smaller ones. Additional thruster cost savings might be achieved by going to very high specific impulses to increase the thrust density and therefore the thrust of a unit of specified size. The extent to which thruster sizes and specific impulses can be increased under the constraints of acceptably long lifetime and good thruster performance is the subject of this analysis.

Analysis

Assume Maxwellian electron temperature, primary electron energy, and the primary-to-Maxwellian electron density ratio are all constants. These assumptions should be reasonable for operation near the "knee" of the discharge-loss/propellant-utilization performance curve for thrusters with diameters greater than about 30 cm. Since there is a tendency for electron temperature to decrease with thruster diameter this assumption is conservative.

Using the above assumptions and the doubly charged ion model[28], one obtains

$$n_{++} \propto n_e^2 V_p / A_p \quad , \qquad (32)$$

where n_{++} is the density of doubly charged ions, n_e is the total electron density, and V_p and A_p are the volume and surface area of the primary electron region. Inasmuch as $n_{++} << n_+$ is required to assure a long screen grid lifetime, $n_e \approx n_+$ and the above becomes

$$n_{++}/n_{+} \propto n_e V_p/A_p \quad . \tag{33}$$

From Equation 33, it can be concluded that the value of $n_e V_p/A_p$ should not be much greater (if any) for larger thrusters than it is for the 30 cm thruster--otherwise discharge-chamber erosion would become more serious. Keeping this parameter constant, though will limit the propellant utilization which is given by the equation

$$\eta_u \approx J_b/(J_o + J_b) = \frac{J_b/J_o}{1 + J_b/J_o} \quad , \tag{34}$$

where J_b is the ion beam current density, and J_o is the loss rate of un-ionized neutrals (same units as J_b). Equation 34 clearly shows that J_b/J_o should be as high as possible to maximize propellant utilization. For a given propellant,

$$J_o \propto n_o \quad , \tag{35}$$

where n_o is the neutral density in the discharge chamber.[46] Under the constraint of constant electron temperature, energy and primary-to-Maxwellian density ratio, the ion-beam current density becomes

$$J_b \propto n_e n_o V_p/A_p \quad . \tag{36}$$

The ratio J_b/J_o, with substitution of Equations 35 and 36 is, then,

$$J_b/J_o \propto n_e V_p/A_p \quad . \tag{37}$$

But Equation 37 uses the same grouping $n_e V_p/A_p$ that determines the ratio n_{++}/n_{+}. Limitation of the doubly-charged ion ratio thus leads to a similar limitation in maximum propellant utilization.

The maximum value of $n_e V_p/A_p$ can also be used to infer a maximum depth for the discharge chamber. From the Bohm velocity criterion[6] the ion-beam current density can be related to the discharge-chamber electron density,

$$J_b \propto n_e \qquad (38)$$

Combining Equations 36 and 38, and solving for V_p/A_p yields

$$V_p/A_p \propto 1/n_o \quad . \qquad (39)$$

Since $n_e V_p/A_p$ is limited to a maximum value however Equation 36 becomes

$$J_b \propto n_o \quad , \qquad (40)$$

and Equation 39 can therefore be rewritten as

$$V_p/A_p \propto 1/J_b \quad . \qquad (41)$$

For a large, flat discharge chamber, the depth is about twice V_p/A_p. This depth, then will vary inversely as ion-beam current density.

The energy cost of making ions in the discharge tends toward a constant of 50-60 eV/ion.[47] The higher loss per beam ion observed in actual thrusters is explainable in terms of ion-chamber geometry. For large flat chambers, between 1/3 to 1/2 of the ions produced should leave the chamber via the ion beam. Discharge losses should therefore be in the 100-180 eV/ion range for large, flat chambers.

The maximum useful thruster diameter can be determined from breakdown voltages and acceptable span-to-gap ratios. For the 1-10 mm range of grid gaps with mercury, the maximum allowable electric field is roughly 2×10^6 V/m.[47] For a reasonable net-to-total voltage ratio R of 0.7, the net accelerating voltage V_{net} would be about 1400 V per mm of accelerator system gap. Assuming dished molybdenum grids the beam diameter should not exceed 300-600 times the gap.[47] For singly ionized mercury, the specific impulse is approximately

$$I_{sp} \approx 100(V_{net})^{\frac{1}{2}} \quad . \qquad (42)$$

Substitution of 1.4×10^6V/m times the gap ℓ_g for V_{net} gives

$$I_{sp} \approx 100(1.4 \times 10^6 \ell_g)^{\frac{1}{2}} \quad . \qquad (43)$$

Solving for ℓ_g yields

$$\ell_g \approx 7 \times 10^{-11} I_{sp}^{\ 2} \quad . \qquad (44)$$

Using 300-600 times this gap as the beam diameter one obtains,

$$D_b \approx 2 - 4 \times 10^{-8} I_{sp}^{\ 2} \quad . \qquad (45)$$

The permissible beam diameter, from structural and breakdown considerations, thus increases as the square of the specific impulse. If the span-to-gap ratio of the accelerator system is held constant, and R is not decreased, an increase in diameter over that given by Equation 45 will result in no increase in thrust.

The charge-exchange erosion will also be reasonable for higher specific impulses. This can be shown from Child's law.

$$J_b \propto V^{3/2}/\ell_g^{\ 2} \quad . \qquad (46)$$

where V is the total accelerating voltage. For a constant electric field strength E, between the grids this becomes

$$J_b \propto E^2/V^{\frac{1}{2}} \propto 1/V^{\frac{1}{2}} \qquad (47)$$

The sputtering yield Y varies as V^n, where n is a number between 0 and 1 over the energy range of interest. The rate of accelerator material removed per unit area $\dot{m}_{ac}$ is given by

$$\dot{m}_{ac} \propto J_b n_o Y \ell_g \quad . \qquad (48)$$

With the substitutions of V^n for Y and $J_b(1-\eta_u)$ for n_o this becomes

$$\dot{m}_{ac} \propto J_b^2 (1-\eta_u) V^n \ell_g \quad . \qquad (49)$$

Noting that η_u will tend towards a constant for an optimum design, using Equation 47 to substitute for J_b, and recognizing a constant electric field implies $\ell_g \propto V$, Equation 44 becomes

$$\dot{m}_{ac} \propto V^n \quad . \qquad (50)$$

Charge exchange erosion per unit beam area will therefore increase as specific impulse is increased but compensation for the increased erosion can be achieved by making the accel grid thickness proportional to ℓ_g.

Designing for a constant electric field and a constant net-to-total voltage ratio also results in constant thrust per unit beam area. This can be shown from

$$T/A \propto J_b I_{sp} \quad . \qquad (51)$$

Substitution of Equations 42 and 47 and holding R constant gives

$$T/A = \text{constant} \quad .$$

Conclusions

The conclusions which can be drawn from a study such as this depend on the level of technology used in the analysis. The level assumed here has been in general, that of the current 30-cm mercury thruster. Future technology developments could obviously affect the validity of the conclusions given.

1. To keep the doubly ionized fraction within reasonable limits for discharge chamber erosion, the maximum propellant utilization will be limited. Based on present 30 cm data, this limit will be 0.90-0.95.
2. The limits on doubly ionized fraction and propellant utilization also imply a definite depth for the discharge chamber. This depth is small enough that the discharge chamber for a large, high specific impulse thruster will have L/D << 1. To maintain a uniform beam with such a chamber (without undue complexity) would require a low magnetic field strength over most of the volume. A multipole magnetic field is one configuration that would meet this low field strength requirement. From 30 cm data, the chamber depth should be 5 to 10 cm at 3000 seconds specific impulse and from Equations 41, 42, and 47 it should increase in proportion to the I_{sp} at higher values.
3. The fraction of ions produced that escapes into the ion beam should increase with thruster size and this should result in a lowering of the discharge losses (100-180 eV/ion).
4. The maximum useful thruster diameter increases rapidly with specific impulse. From Equation 45 one obtains the following:

I_{sp}(sec.)	3000	5000	7000	10000
D_b(cm)	18-36	50-100	100-200	200-400

5. The thrust per unit beam area should be approximately constant over a range of specific impulse. A factor of perhaps two improvement might be expected over 30 cm data--from a more uniform beam profile.
6. Under the imposed constraints of a fixed doubly-to-singly charged

ion fraction in the discharge chamber and a constant electric field between the grids, the discharge-chamber erosion rate will decrease with increasing specific impulse. The accelerator erosion rate will increase with specific impulse, but can be offset by making grid thickness proportional to accelerator-system gap. Because of these effects, there may be a net advantage to increasing the doubly ionized fraction (and hence propellant utilization) slightly at high specific impulses.

7. Multiple discharge-chamber cathodes will probably be required for thrusters much larger than 30 cm in diameter. The problems of parallel hollow cathodes indicate that it would be simpler to use a separate discharge supply and control loop for each cathode.

MOLECULAR NITROGEN ION DENSITIES IN MERCURY DISCHARGE CHAMBERS

During the period covered by this report anomalies in the erosion rates of cathode potential surfaces in mercury ion thrusters were discovered in tests conducted at two different laboratories. An experiment was performed that suggested these anomalies might be caused by variations in the background partial pressure of nitrogen in the test facilities. It was postulated that this occurs because some of the nitrogen molecules entering the discharge chamber are ionized. Subsequently they strike the truster walls and because they are in an ionized, reactive state they form a sputter-resistant material with the wall. If this process does occur it might provide an explanation for the experimentally observed increase in putter resistance of thruster materials with nitrogen partial pressure.

One step associated with the study of this phenomenon was the determination of the density of molecular nitrogen ions in the discharge chamber of a thruster. To calculate this quantity the model developed for the calculation of doubly charged mercury ions[28] was adapted to the problem as described below. Nitrogen ion densities were then calculated for the operating conditions of the 30 cm diameter thruster in which the anomolous erosion rates had been observed.

Analysis

Figure 61 is a schematic of a vacuum tank containing nitrogen at a partial pressure P_0 and a density n_0 together with a discharge chamber. If the vacuum tank surfaces are at an average temperature T_0 (°K), then the

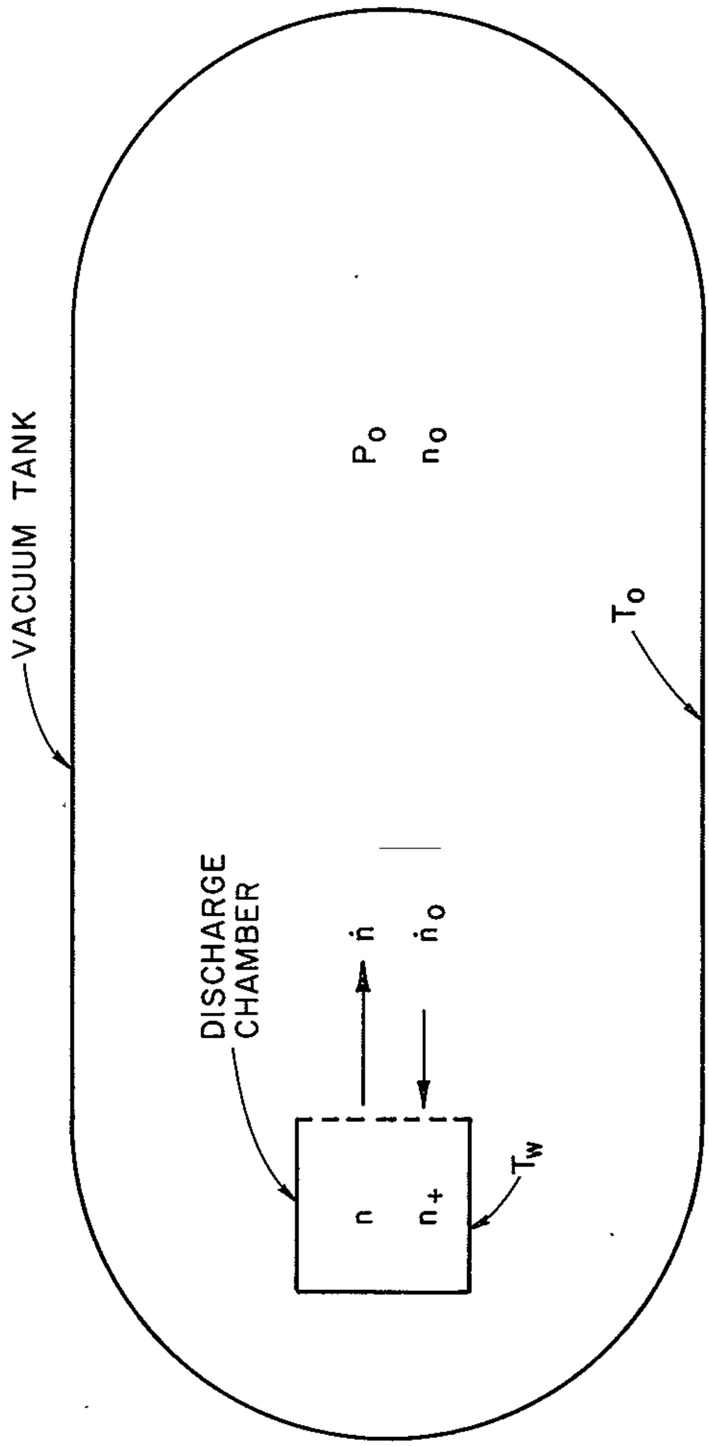

NITROGEN FLOW SCHEMATIC

FIGURE 61

nitrogen density in the tank will be given by

$$n_o = \frac{P_o}{kT_o} \quad , \tag{52}$$

where k is Boltzmann's constant. Some of these neutral nitrogen molecules flow into the discharge chamber at a rate $\dot{n}_o$ determined by the equation for free molecular flow through a sharp-edged orifice.

$$\dot{n}_o = \frac{n_o \, v_o \, A_A}{4} \tag{53}$$

Where A_A is the open area of the grid system to neutral flow (generally the open area of the accelerator grid) and v_o is the thermal velocity of the nitrogen.

$$v_o = \sqrt{\frac{8kT_o}{\pi m_o}} \tag{54}$$

The term m_o in this equation is the mass of a nitrogen molecule.

The nitrogen flow into the thruster as given by Equation 53 must be equal to the nitrogen outflow in the steady state. This outflow is the sum of the neutral outflow rate and the ionic outflow rate and is given by

$$\dot{n} = \frac{n \, v \, A_A}{4} + n_+ \, v_+ \, A_S \tag{55}$$

where n is the neutral nitrogen molecular density inside the discharge chamber, n_+ is the corresponding molecular nitrogen ion density and A_S is the open area of the grids to ions (generally close to the screen grid open area). The term v in this equation is the velocity of the neutral nitrogen molecules within the discharge chamber and is given by

$$v = \sqrt{\frac{8kT_w}{\pi m_o}} \tag{56}$$

where T_w is the discharge chamber wall temperature (°K). The term v_+ in Equation 56 is the nitrogen ion velocity as determined by the Bohm equation [48]

$$v_+ = \sqrt{\frac{T_{mx} e}{m_o} \left(1 + \frac{n_{pr}}{n_{mx}} \right)} \quad . \tag{57}$$

As suggested by this equation the electrons effecting the ionizations in the discharge chamber are assumed to consist of a Maxwellian group (temperature T_{mx}(eV) and density n_{mx}) and a monoenergetic or primary group (energy ε_{pr}(eV) and density n_{pr}). The term "e" in Equation 57 is the electron charge.

In order to calculate the ion density for use in Equation 55 it was necessary to model the ionization process occurring in the discharge chamber. It was therefore assumed that only one reaction was important in the production of molecular nitrogen ions, namely

$$N_2 + e^- \rightarrow N_2^+ + 2e^- \quad .$$

Cross sections for this reaction were obtained from the literature[49] and other possible reactions involving intermediate dissociation and/or electronic exitation reactions were neglected. These other reactions could be significant but their incorporation into the analysis would require a thorough literature survey which was not considered to be warrented here. The process defined by the above equation should produce results accurate to within $\pm$ 100%.

If one equates the production and loss rates of nitrogen molecules in the manner described by Peters[28] the following equation for the ratio of neutral-to-singly ionized nitrogen molecules in the discharge chamber is obtained.

$$\frac{n}{n_+} = \frac{1}{V_p/A_p} \frac{\left[\frac{e}{m_o} T_{mx}\left(1+\frac{n_{pr}}{n_{mx}}\right)\right]^{\frac{1}{2}}}{F+\left(n_{pr}\, P_o^+\, (\xi_{pr}) + n_{mx}\, Q_o^+\, (T_{mx})\right)} \tag{58}$$

The previously undefined terms appearing in this equation are:

V_p/A_p - volume-to-surface area ratio for the primary electron region of the discharge chamber.

F_+ - the uniformity factor describing the ion flux averaged at the surface of the primary electron region to the flux averaged over the volume of this region.

$P_o^+\ (\xi_{pr})$ - The cross section - electron velocity product pertaining to primary electrons at the energy ξ_{pr}. This parameter is plotted in Figure 62 for the reaction being considered.

$Q_o^+\ (T_{mx})$ - The cross section - electron velocity product integrated over energy for Maxwellian electrons at the temperature T_{mx}. This parameter is also plotted in Figure 62 for the reaction being considered.

Combining Equations 52 through 57 one obtains

$$\dot{n}=\dot{n}_o = \frac{P_o A_A}{4kT_o}\sqrt{\frac{8kT_o}{\pi m_o}} = n_+\left[\frac{A_A}{4}\left(\frac{n}{n_+}\right)\sqrt{\frac{8kT_w}{\pi m_o}} + A_S\sqrt{\frac{T_{mx}e}{m_o}\left(1+\frac{n_{pr}}{n_{mx}}\right)}\right] \tag{59}$$

or rearranging to solve for the nitrogen ion density

$$n_+ = \frac{P_o}{\frac{n}{n_+}\, k\sqrt{T_w T_o} + \frac{A_S}{A_A}\sqrt{2\pi(kT_o e\, T_{mx})\ (1+\frac{n_{pr}}{n_{mx}})}} \tag{60}$$

Using the geometrical and plasma conditions pertaining to the particular thruster being considered Equation 58 can first be solved and then

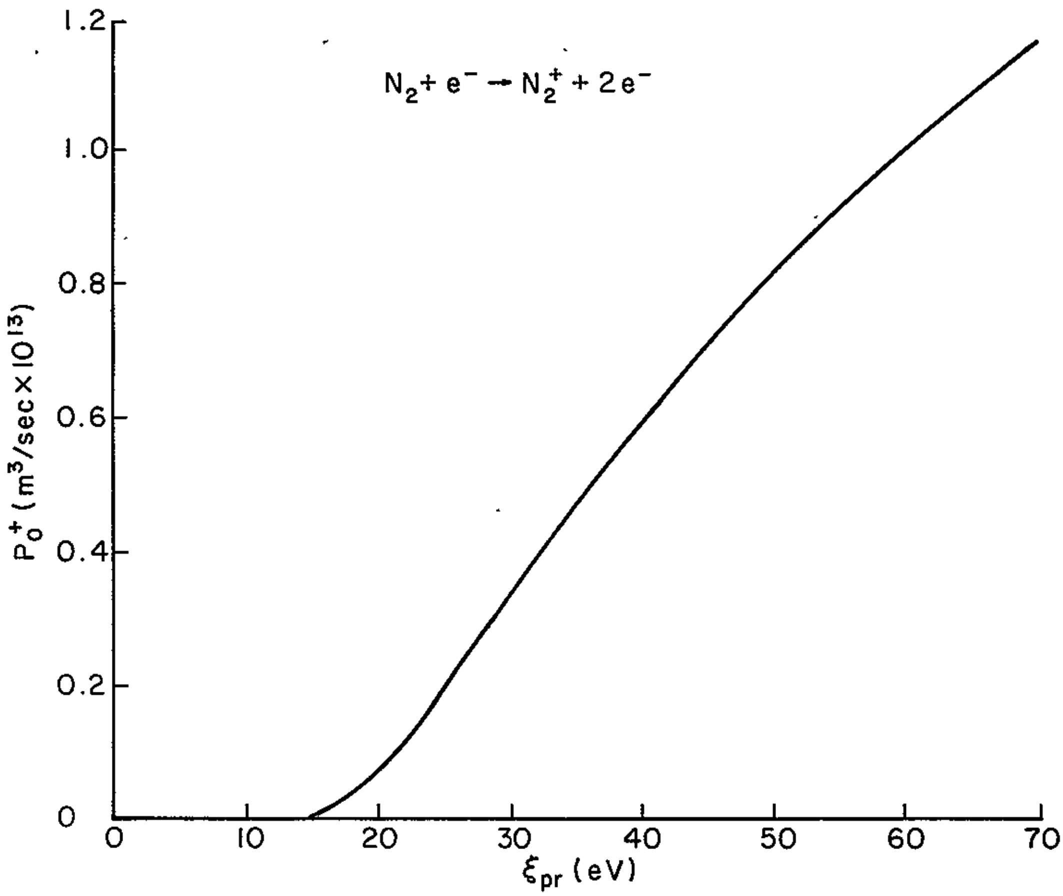

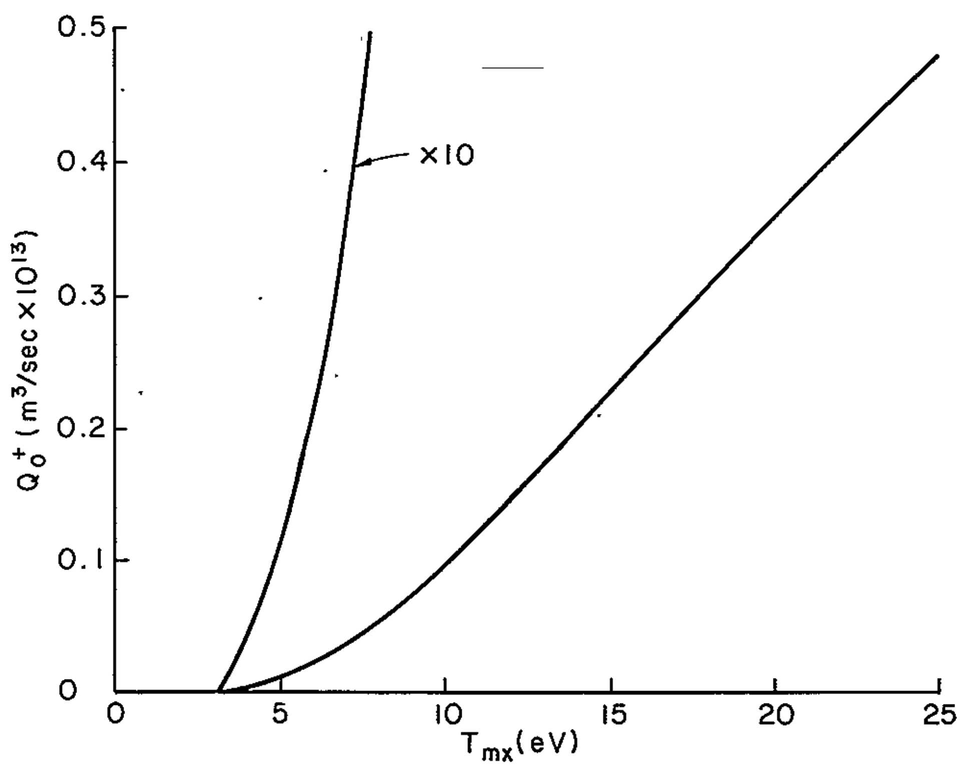

RATE FACTORS FOR MOLECULAR NITROGEN

FIGURE 62

Equation 60 can be solved for the nitrogen molecular ion density.

Application to the 30 cm Thruster

For the 30 cm thruster with EM optics operating at a 2 amp beam current the following properties apply:[28]

$\forall/A = 0.025$ m

$F_{+} = 1.5$

$n_{pr} = 3.28 \times 10^{16}$ m^{-3}

$n_{mx} = 13.1 \times 10^{16}$ m^{-3}

$T_{mx} = 3.8$ eV

$\xi_{pr} = 27.2$ eV

$n_{pr}/n_{mx} = 0.25$

$\frac{A_S}{A_A} = \frac{0.676}{0.433} = 1.56$

For these conditions Figure 62 gives $\overline{P_o^+} = 0.25 \times 10^{-13}$ m^3/sec and $Q_o^+ = 0.4 \times 10^{-15}$ m^3/sec. If the temperature of the tank liner is assumed to be

$$T_o \simeq 100°K ,$$

and the temperature of the thruster wall is assumed to be

$$T_w \simeq 500°K ,$$

then Equation 58 gives

$$\frac{n}{n_+} = 123.$$

Equation 60 then gives

$$n_+ = 1.98 \times 10^{18} P_o$$

where P_o in nt/m^2 yields n^+ in m^{-3}. Substituting values of P_o in the range of interest the results shown in Table IV are obtained.

Table IV

Molecular Nitrogen Ion Density in the 30 cm Diameter EM Thruster

P_o (torr)	n_+ (cm^{-3})
10^{-7}	2.6×10^7
10^{-6}	2.6×10^8
10^{-5}	2.6×10^9
10^{-4}	2.6×10^{10}

REFERENCES

1. Lockwood, D. L., Michelson, W. and Hamza, V., "Analytical Space-Charge Flow and Theoretical Electrostatic Rocket Engine Performance," presented at the 1st Electric Propulsion Conference, Berkely, Calif., March 14-16, 1962.

2. Hyman, J., Eckhardt, W. O., Knechtli, R. C. and Buckey, C. R., "Formation of Ion Beams from Plasma Sources: Part 1," AIAA Journal, V. 2, pp. 1739-1748, Oct. 1964.

3. Lathem, W. C., "Ion Accelerator Designs for Kaufman Thruster," Journal of Spacecraft and Rockets, V. 6, pp. 1237-1242, Nov. 1969.

4. Kaufman, H. R., "Accelerator System Solutions for Broad-Beam Ion Sources," AIAA Journal, V. 15, pp. 1025-1034, July 1977.

5. Aston, G., "Ion Optics Study," in "15 cm Mercury Ion Thruster Research" (Wilbur, P. J., Ed.), pp. 49-70, NASA CR-134905, December 1975.

6. Bohm, D., "Minimum Ionic Kinetic Energy for a Stable Sheath," The Characteristics of Electrical Discharges in Magnetic Fields, Guthrie, A., and Wakerling, R. K., Eds., McGraw-Hill, New York, pp. 77-86, 1949.

7. Child, C. D., "Discharge from Hot CaO," Phys. Rev., Vol. 32, pp. 492-511, 1911.

8. Aston, G., "The Ion-Optics of a Two-Grid Electron-Bombardment Thruster," NASA CR-135024, May 1976.

9. Masek, T. D., Poeschel, R. L., Collet, C. R., and Schnelker, D. E., "Evolution and Status of the 30-cm Engineering Model Ion Thruster," AIAA Paper No. 76-1006, 1976.

10. Hyman, J., Dulgeroff, C. R., Kami, S. and Williamson, W. S., "One-Millipound Mercury Ion Thruster," AIAA Paper No. 75-386, 1975.

11. Robinson, R. S. and Kaufman, H. R., "Ion Thruster Technology Applied to a 30-cm Multipole Sputtering Ion Source," AIAA Journal, V. 15, pp. 702-706, May 1977.

12. Kaufman, H. R., Reader, P. D. and Isaacson, G. C., "Ion Sources for Ion Machining Applications," AIAA Journal, V. 15, pp. 843-847, June 1977.

13. Alterburg, W., Freisinger, J., Hauser, J., Seibt, N. and Loeb, H. W., "Beam Formation in RF-Ion Thrusters," AIAA Paper No. 75-426, 1975.

14. Kaufman, H. R., "Technology of Electron-Bombardment Ion Thruster," Advances in Electronics and Electron Physics, Vol. 36, Academic Press Inc., San Francisco, pp. 265-373, 1974.

15. Aston, G. and Kaufman, H. R., "The Ion-Optics of a Two-Grid Electron-Bombardment Thruster," AIAA Paper No. 76-1029, 1976.

16. Wilbur, P. J., "Argon-Xenon Discharge Chamber Model for the Production of Doubly Charged Ions," in "Inert Gas Thrusters" (Kaufman, H. R., Ed.), pp. 46-64, NASA CR-135226, July 1977.

17. Meadows, G. A. and Free, B. A., "Effect of a Decel Electrode on Primary and Charge-Exchange Ion Trajectories," AIAA Paper No. 75-427, 1975.

18. Wilbur, P. J., "Effects of a Small Hole Accelerator Grid on SERT II Thruster Performance," in "15 cm Mercury Ion Thruster Research-1976,: NASA CR-135116, pp. 3 - 13, December 1976.

19. Fearn, D. G. and C. M. Philip, "An Investigation of Physical Processes in a Hollow Cathode Discharge," AIAA Paper No. 73-1137, Oct. 31 - Nov. 2, 1973.

20. Philip, C. M. and D. G. Fearn, "Recent Hollow Cathode Investigations at the R.A.E.," AIAA Paper No. 73-1137, Oct. 31 - Nov. 2, 1973.

21. Csicky, George, "Investigations of a Hollow Cathode Discharge Plasma," AIAA Paper No. 69-258, March 3-5, 1969.

22. Bessling, Harro, "Theorie der Hochtemperatur-Hohlkathode, ein Modell für den Kathodenmechanismus," DFVLR Report DLR-FB 76-50, Stuttgart, Germany, 1976.

23. Krishnan, M. et al., "Physical Processes in Hollow Cathodes," AIAA Journal, V. 15, No. 9, pp. 1217-1223, September 1977.

24. Beattie, J. R., "Numerical Procedure for Analyzing Langmuir Probe Data," AIAA Journal, V. 13, No. 7, pp. 950-952, July 1975.

25. Seigfried, D., "The Effect of the Insert on Hollow Cathode Temperatures," appears in "15 cm Mercury Ion Thruster Reserach-1976," NASA CR-135116, December 1976.

26. Anon., "8-cm Mercury Ion Thruster System Technology," NASA TM X-71611, Oct. 21-23, 1974.

27. Hyman, J. and R. L. Poeschel, "Satellite Control Mercury Ion Thruster," AIAA Paper No. 73-1132, Oct. 31 - Nov. 2, 1973.

28. Peters, R. R. et al., "Mercury Ion Thruster Doubly Charged Ion Model," Journal of Spacecraft and Rockets, V. 14, No. 8, pp. 461-468, Aug. 1977.

29. Wilbur, P. J., "Experimental Investigation of a Throttlable 15 cm Hollow Cathode Ion Thruster," NASA CR-121038, pp. 2-4, Dec. 1972.

30. Vahrenkamp, R. P., "Measurement of Double Charged Ions in the Beam of a 30-cm Mercury Bombardment Thruster," AIAA Paper 73-1057, October 1973.

31. Peters, R. R., "Double Ion Production in Mercury Thrusters," NASA CR-135019, April 1976.

32. Hughes Research Laboratories, Ion Physics Staff, "Thruster Endurance Test," NASA CR-135011, May 1976.

33. Knauer, W., R. L. Poeschel, and J. W. Ward, "Radial Field Kaufman Thruster," Journal of Spacecraft and Rockets, V. 7, No. 3, pp. 248-250, March 1970.

34. Poeschel, R. L. and R. Vahrenkamp, "The Radial Magnetic Field Geometry as an Approach to Total Ion Utilization in Kaufman Thrusters," AIAA Paper No. 72-481, April 17-19, 1972.

35. Beattie, J. R. and P. J. Wilbur, "Cusped Magnetic Field Mercury Ion Thruster," AIAA Paper No. 76-1011, Nov. 14-17, 1976.

36. King, H. J., R. L. Poeschel and J. W. Ward, " $2\frac{1}{2}$ kW Low Specific Impulse, Hollow Cathode Mercury Thruster," AIAA Paper No. 69-300, March 3-5, 1969.

37. Knauer, W., R. L. Poeschel, H. J. King, and J. W. Ward, "Discharge Chamber Studies for Mercury Bombardment Ion Thruster," NASA CR-72440, September 1968.

38. Beattie, J. R., "Cusped Magnetic field Mercury Ion Thruster," NASA CR-135047, July 1976.

39. Reader, P. D., "Investigation of a 10-Centimeter-Diameter Electron Bombardment Ion Rocket," NASA TN D-1163, 1962.

40. Chen, F. F., Introduction to Plasma Physics, Plenum Press, New York 1974.

41. Isaacson, G. C., "Multipole Gas Thruster Design," NASA CR-135101, June 1977.

42. Kadomtsev, B. B. and A. V. Nedospasov, J. Nuclear Energy, Part C, V. 1, P. 230, 1960.

43. Cap, F. F., Handbook on Plasma Instabilities, Academic Press, New York, 1976.

44. Allen, T. K., G. A. Paulikas, R. V. Pyle, "Instability of a Positive Column in a Magnetic Field," Phys. Rev. Letters, V. 5, p. 409, November 1960.

45. Bohm, D., E.H.S. Burhop, and H.S.W. Massey, "The Use of Probes for Plasma Exploration in Strong Magnetic Fields," in Characteristics of Electric Discharges in Magnetic Fields, A. Guthrie and R. K. Wakerling, Eds., McGraw-Hill, New York, 1949.

46. Kaufman, H. R., "Ion-Thruster Propellant Utilization," Ph.D. Thesis, June 1971, Dept. of Mechanical Engineering, Colorado State University, Fort Collins, Colorado.

47. Kaufman, H. R., "Technology of Electron-Bombardment Ion Thrusters," Advances in Electronics and Electron Physics, V. 36, Ed., L. Morton, Academic Press, New York, 1974, pp. 265-373.

48. Masek, T. R., "Plasma Properties and Performance of Mercury Ion Thrusters," AIAA Paper No. 69-256, March 3-5, 1969.

49. Rapp, D., and P. Englander-Gordon, "Total Cross Sections for Ionization and Attachment in Gases by Electron Impact," J. of Chem. Phys., V. 43, No. 5, pp. 1464-1479, September 1, 1965.

APPENDIX I

Two Grid Ion Beam Divergence Results for Argon

and a Screen Hole Diameter (d_s) of 2.06 mm

V_T	V_D	R	$\frac{\ell_g}{d_s}$	$\frac{d_a}{d_s}$	$\frac{t_s}{d_s}$	$\frac{t_a}{d_s}$	NP/H (nano-pervs/hole)	α (deg.)	f_D
600	32	0.7	0.494	0.642	0.185	0.370	0.346	20.6	0.9719
							0.708	18.8	0.9776
							1.062	17.5	0.9812
							1.414	15.7	0.9841
							1.741	14.4	0.9864
							2.070	14.0	0.9874
							2.422	14.1	0.9873
							2.774	14.3	0.9867
							3.092	14.6	0.9855
							3.369	15.1	0.9845
	40						0.346	18.4	0.9775
							0.708	17.3	0.9810
							1.062	15.7	0.9847
							1.414	13.7	0.9878
							1.741	12.9	0.9894
							2.070	12.9	0.9897
							2.422	13.2	0.9892
							2.774	13.7	0.9881
							3.085	14.4	0.9867
	50						0.346	16.8	0.9808
							0.708	15.7	0.9845
							1.062	13.5	0.9883
							1.414	11.8	0.9911
							1.741	11.4	0.9921
							2.070	11.9	0.9916
							2.422	12.6	0.9904
							2.734	13.2	0.9880
	32						0.436	17.3	0.9788
							0.916	16.2	0.9824
							1.373	14.2	0.9864
							1.832	12.3	0.9892
							2.289	11.9	0.9902
							2.701	12.4	0.9897
							3.135	13.3	0.9882
							3.378	13.9	0.9871
	40						0.436	15.6	0.9824
							0.916	14.4	0.9861
							1.373	12.1	0.9898
							1.832	10.7	0.9919
							2.289	10.8	0.9921
							2.701	11.4	0.9912
							3.033	12.0	0.9903
	50						0.436	13.9	0.9860
							0.916	12.6	0.9892
							1.373	9.9	0.9927
							1.832	9.5	0.9937
							2.289	10.1	0.9931
							2.622	10.7	0.9921
1100	40	0.5	0.247				0.736	29.0	0.9500
							1.503	26.5	0.9570
							2.256	25.3	0.9622
							2.992	25.3	0.9634
							3.714	25.2	0.9630
							4.598	25.6	0.9600

V_T	V_D	R	$\frac{\ell_g}{d_s}$	$\frac{d_a}{d_s}$	$\frac{t_s}{d_s}$	$\frac{t_a}{d_s}$	NP/H (nano-pervs/hole)	α (deg.)	f_D
1100	40	0.7	0.247	0.642	0.185	0.370	0.736	24.9	0.9617
							1.503	20.6	0.9751
							2.256	15.3	0.9832
							2.992	15.5	0.9834
							3.714	16.8	0.9811
							4.576	18.3	0.9775
		0.9					0.736	21.5	0.9718
							1.503	14.1	0.9884
							2.256	9.3	0.9930
							2.992	8.8	0.9936
							3.714	9.2	0.9924
							5.010	11.8	0.9865
		0.5	0.494				0.588	24.5	0.9648
							1.169	22.5	0.9675
							1.728	21.3	0.9706
							2.314	19.2	0.9735
							2.856	18.9	0.9742
							3.363	19.0	0.9735
							3.781	19.3	0.9720
							3.876	19.9	0.9715
		0.7					0.588	21.0	0.9723
							1.169	18.5	0.9793
							1.728	14.8	0.9852
							2.314	13.0	0.9881
							2.856	13.0	0.9883
							3.170	13.3	0.9876
							3.569	13.7	0.9863
							3.985	14.2	0.9834
		0.9					0.588	18.6	0.9777
							1.169	15.8	0.9870
							1.728	10.6	0.9937
							2.314	8.0	0.9957
							2.856	8.0	0.9955
							3.363	8.7	0.9946
							3.781	9.4	0.9936
							4.230	10.3	0.9910
		0.5	0.741				0.462	22.0	0.9688
							0.950	19.9	0.9743
							1.420	18.4	0.9775
							1.891	16.5	0.9803
							2.338	15.9	0.9819
							2.793	16.0	0.9822
							3.265	16.4	0.9815
							3.639	16.9	0.9800
		0.7					0.462	18.0	0.9776
							0.950	16.3	0.9824
							1.420	14.5	0.9869
							1.891	11.8	0.9906
							2.338	10.4	0.9923
							2.793	10.3	0.9926
							3.265	11.1	0.9915
							3.440	11.4	0.9910
		0.9					0.462	16.3	0.9814
							0.950	14.6	0.9863
							1.420	12.5	0.9917
							1.891	9.0	0.9955
							2.338	6.8	0.9969
							2.793	6.4	0.9973
							3.265	6.7	0.9969
							3.746	7.6	0.9959
							3.928	8.0	0.9950

V_T	V_D	R	$\frac{\ell_g}{d_s}$	$\frac{d_a}{d_s}$	$\frac{t_s}{d_s}$	$\frac{t_a}{d_s}$	NP/H (nano-pervs/hole)	α (deg.)	f_D
1100	40	0.5	1.000	0.642	0.185	0.370	0.578	18.6	0.9765
							1.183	16.5	0.9813
							1.760	15.0	0.9845
							2.351	13.4	0.9869
							2.958	13.5	0.9874
							3.519	14.3	0.9864
							3.866	14.8	0.9855
		0.7					0.578	15.8	0.9818
							1.183	14.4	0.9858
							1.760	12.4	0.9990
							2.351	9.8	0.9930
							2.958	9.1	0.9940
							3.519	9.8	0.9933
							4.082	10.5	0.9920
		0.9					0.429	14.7	0.9847
							0.866	13.4	0.9878
							1.298	12.2	0.9910
							1.703	10.6	0.9944
							2.110	8.2	0.9971
							2.646	5.7	0.9985
							2.958	4.9	0.9989
							3.347	4.9	0.9988
							3.866	5.4	0.9980
		0.7	0.494	0.278			0.108	21.0	0.9684
							0.228	22.1	0.9670
							0.342	22.3	0.9673
							0.455	22.2	0.9685
							0.570	21.8	0.9695
							0.672	21.4	0.9710
							0.728	21.1	0.9721
							0.792	20.8	0.9740
				0.469			0.228	22.2	0.9672
							0.468	22.1	0.9686
							0.695	21.3	0.9711
							0.928	20.4	0.9740
							1.169	19.6	0.9767
							1.391	18.5	0.9795
							1.613	16.8	0.9823
							1.784	15.4	0.9846
							1.933	13.8	0.9870
				0.827			0.588	20.5	0.9734
							1.169	17.9	0.9806
							1.728	14.1	0.9866
							2.314	12.7	0.9892
							2.856	13.2	0.9883
							3.569	14.3	0.9855
							4.356	15.2	0.9719
							5.097	16.1	0.9779
							5.308	16.7	0.9765
				0.642	0.062		0.588	22.4	0.9720
							1.169	20.2	0.9777
							1.728	17.6	0.9828
							2.314	14.0	0.9866
							2.856	12.9	0.9879
							3.363	13.1	0.9875
							3.778	13.7	0.9861
							3.894	13.8	0.9860
					0.123		0.588	22.2	0.9718
							1.169	19.7	0.9776
							1.728	16.9	0.9823
							2.314	14.0	0.9863

V_T	V_D	R	$\frac{\ell_g}{d_s}$	$\frac{d_a}{d_s}$	$\frac{t_s}{d_s}$	$\frac{t_a}{d_s}$	NP/H (nano-pervs/hole)	α (deg.)	f_D
1100	40	0.7	0.494	0.642	0.123	0.370	2.856	13.3	0.9877
							3.363	13.5	0.9873
							3.778	13.8	0.9862
							4.178	14.0	0.9852
							4.333	14.2	0.9841
					0.247		0.468	21.3	0.9711
							0.929	19.6	0.9767
							1.391	17.9	0.9819
							1.841	14.8	0.9860
							2.314	13.2	0.9880
							2.748	12.9	0.9883
							3.170	13.2	0.9874
							3.569	13.7	0.9865
					0.185	0.123	0.588	20.9	0.9727
							1.169	18.3	0.9804
							1.728	14.2	0.9868
							2.314	12.4	0.9899
							2.856	12.7	0.9896
							3.170	13.0	0.9890
							3.569	13.5	0.9876
							3.985	14.3	0.9848
							4.105	14.5	0.9845
						0.617	0.468	21.6	0.9706
							0.929	19.5	0.9764
							1.391	17.3	0.9816
							1.841	14.2	0.9857
							2.314	13.2	0.9874
							2.748	13.1	0.9874
							3.170	13.7	0.9872
							3.323	13.9	0.9856
						0.864	0.468	21.7	0.9704
							0.929	19.5	0.9764
							1.391	17.4	0.9808
							1.841	14.9	0.9843
							2.314	14.1	0.9860
							2.748	14.0	0.9862
							2.965	14.2	0.9854
							3.078	14.3	0.9850
	32					0.370	0.588	22.3	0.9695
							1.169	19.8	0.9770
							1.728	16.3	0.9829
							2.314	14.5	0.9856
							2.856	14.3	0.9861
							3.170	14.5	0.9854
							3.569	14.8	0.9839
							3.781	15.0	0.9830
	50						0.588	20.1	0.9743
							1.169	17.7	0.9814
							1.728	13.7	0.9874
							2.314	12.5	0.9896
							2.856	12.9	0.9890
							3.170	13.3	0.9881
							3.569	13.8	0.9865
							3.843	14.1	0.9850
	32		0.741				0.462	19.3	0.9752
							0.950	17.4	0.9802
							1.420	15.5	0.9849
							1.891	13.1	0.9887
							2.338	11.7	0.9905
							2.793	11.3	0.9911

V_T	V_D	R	$\frac{\ell_g}{d_s}$	$\frac{d_a}{d_s}$	$\frac{t_s}{d_s}$	$\frac{t_a}{d_s}$	NP/H (nano-pervs/hole)	α (deg.)	f_D
1100	32	0.7	0.741	0.642	0.185	0.370	3.265	11.7	0.9903
							3.440	12.0	0.9900
	50						0.462	16.7	0.9803
							0.950	15.1	0.9849
							1.420	13.2	0.9891
							1.891	10.2	0.9930
							2.338	9.1	0.9941
							2.793	9.5	0.9936
							3.265	10.4	0.9924
							3.291	10.5	0.9922
1500	40		0.494	0.278			0.143	20.5	0.9792
							0.292	21.6	0.9677
							0.436	22.4	0.9671
							0.582	22.4	0.9680
							0.733	22.2	0.9690
							0.871	21.7	0.9706
							0.943	21.4	0.9721
							0.997	21.0	0.9734
				0.469			0.294	24.0	0.9660
							0.585	22.5	0.9677
							0.873	21.6	0.9707
							1.156	20.6	0.9741
							1.454	19.6	0.9774
							1.726	17.8	0.9807
							2.115	15.3	0.9848
							2.306	13.4	0.9880
	32		0.494	0.642			0.595	23.5	0.9665
							1.250	20.5	0.9743
							1.862	17.1	0.9818
							2.502	15.2	0.9845
							3.078	15.8	0.9833
							3.840	16.5	0.9815
	40						0.595	22.4	0.9680
							1.250	19.9	0.9764
							1.862	16.2	0.9837
							2.502	14.2	0.9866
							3.078	14.4	0.9863
							3.673	15.2	0.9843
							4.082	15.6	0.9830
	50						0.595	21.5	0.9705
							1.250	18.9	0.9785
							1.862	14.7	0.9861
							2.502	12.9	0.9888
							3.078	13.5	0.9879
							3.673	14.4	0.9859
							4.046	14.9	0.9845
	32		0.741				0.597	20.5	0.9730
							1.186	18.0	0.9792
							1.755	15.9	0.9848
							2.350	12.9	0.9889
							2.901	11.9	0.9903
							3.446	12.2	0.9899
							3.892	12.8	0.9887
							3.989	13.0	0.9880
	40						0.597	19.6	0.9746
							1.186	17.3	0.9807
							1.755	15.1	0.9862
							2.350	12.0	0.9904
							2.901	11.1	0.9918

V_T	V_D	R	$\frac{\ell_g}{d_s}$	$\frac{d_a}{d_s}$	$\frac{t_s}{d_s}$	$\frac{t_a}{d_s}$	NP/H (nano-pervs/hole)	α (deg.)	f_D
1500	40	0.7	0.741	0.642	0.185	0.370	3.446	11.5	0.9911
							3.892	12.3	0.9898
							4.006	12.6	0.9890
	50						0.597	18.4	0.9768
							1.186	16.3	0.9825
							1.755	14.0	0.9876
							2.350	10.8	0.9917
							2.901	10.3	0.9924
							3.446	10.8	0.9920
							3.892	11.5	0.9908
1835	40						0.565	20.2	0.9737
							1.176	17.2	0.9805
							1.780	15.1	0.9853
							2.379	12.3	0.9893
							2.992	11.0	0.9912

Two Grid Ion Beam Divergence Results for Neon

and a Screen Hole Diameter (d_s) of 2.06 mm

V_T	V_D	R	$\frac{\ell_g}{d_s}$	$\frac{d_a}{d_s}$	$\frac{t_s}{d_s}$	$\frac{t_a}{d_s}$	NP/H (nano-pervs/hole)	α (deg.)	f_D
1100	46	0.7	0.494	0.642	0.185	0.370	0.534	21.4	0.9711
							1.114	19.0	0.9786
							1.686	14.9	0.9861
							2.252	12.7	0.9892
							2.831	13.3	0.9872
							3.622	15.0	0.9840

Two Grid Ion Beam Divergence Results for Krypton

and a Screen Hole Diameter (d_s) of 2.06 mm

V_T	V_D	R	$\frac{\ell_g}{d_s}$	$\frac{d_a}{d_s}$	$\frac{t_s}{d_s}$	$\frac{t_a}{d_s}$	NP/H (nano-pervs/hole)	α (deg.)	f_D
1100	32	0.7	0.494	0.642	0.185	0.370	0.504	21.6	0.9696
							1.007	19.1	0.9769
							1.511	16.1	0.9841
							2.015	13.0	0.9886
							2.502	12.2	0.9899
							3.006	12.6	0.9889
							3.650	13.5	0.9870
	40						0.504	20.5	0.9721
							1.007	18.3	0.9785
							1.511	15.2	0.9858
							2.015	12.2	0.9901
							2.502	11.5	0.9911
							3.006	12.0	0.9900
							3.551	12.8	0.9870
	50						0.504	19.6	0.9744
							1.007	17.4	0.9807
							1.511	14.1	0.9878
							2.015	11.0	0.9917
							2.502	10.7	0.9922
							3.006	11.3	0.9910
							3.343	11.9	0.9890

Two Grid Ion Beam Divergence Results for Xenon

and a Screen Hole Diameter (d_s) of 2.06 mm

V_T	V_D	R	$\frac{\ell_g}{d_s}$	$\frac{d_a}{d_s}$	$\frac{t_s}{d_s}$	$\frac{t_a}{d_s}$	NP/H (nano-pervs/hole)	α (deg.)	f_D
1100	32	0.7	0.494	0.642	0.185	0.370	0.631	20.6	0.9715
							1.260	17.5	0.9810
							1.891	13.3	0.9886
							2.522	11.7	0.9908
							3.132	12.5	0.9890
							3.401	12.9	0.9867

V_T	V_D	R	$\frac{\ell_g}{d_s}$	$\frac{d_a}{d_s}$	$\frac{t_s}{d_s}$	$\frac{t_a}{d_s}$	NP/H (nano-pervs/hole)	α (deg.)	f_D
1100	40	0.7	0.494	0.642	0.185	0.370	0.631	19.9	0.9734
							1.260	17.0	0.9822
							1.891	12.5	0.9899
							2.522	10.9	0.9919
							3.132	11.9	0.9901
							3.360	12.3	0.9875
	50						0.631	19.1	0.9754
							1.260	16.4	0.9834
							1.891	11.8	0.9911
							2.522	10.0	0.9931
							3.132	11.2	0.9910
							3.245	11.5	0.9880

Two Grid Ion Beam Divergence Results for Argon

and a Screen Hole Diameter (d_s) of 1.50 mm

1100	40	0.7	0.504	0.638	0.168	0.336	0.420	22.0	0.9670
							0.827	20.0	0.9729
							1.251	18.3	0.9779
							1.646	16.2	0.9822
							2.060	14.0	0.9859
							2.462	13.1	0.9877
							2.856	13.0	0.9875
							3.024	13.1	0.9870

Two Grid Ion Beam Divergence Results for Argon

and a Screen Hole Diameter (d_s) of 1.00 mm

1100	40	0.7	0.526	0.592	0.132	0.395	0.244	22.3	0.9651
							0.498	21.3	0.9687
							0.742	20.1	0.9731
							0.991	19.0	0.9749
							1.248	17.9	0.9771
							1.484	16.8	0.9789
							1.721	15.9	0.9805
							2.219	14.2	0.9820

DISTRIBUTION LIST

	Number of Copies
National Aeronautics and Space Administration Washington, D. C. 20546 Attn: RPE/Mr. Wayne Hudson	1
National Aeronautics and Space Administration Lewis Research Center 21000 Brookpark Road Cleveland, Ohio 44135 Attn: Research Support Procurement Section	
Mr. Allen Jones, MS 500-313	1
Technology Utilization Office, MS 3-19	1
Report Control Office, MS 5-5	1
Library, MS 60-3	2
N. T. Musial, MS 500-113	1
Mr. E. Davison, MS 3-3	1
Mr. W. E. Moeckel, Chief Scientist, MS 301-1	1
Space Propulsion and Power, MS 501-8	1
Mr. H. Douglass	1
Mr. W. Plohr	1
Mr. R. Finke	1
Mr. D. Byers	1
Mr. B. Banks	1
Mr. R. Lovell	1
Mr. W. Kerslake	30
National Aeronautics and Space Administration Marshall Space Flight Center Huntsville, Alabama 35812 Attn: Mr. Jerry P. Hethcoate	1
Research and Technology Division Wright-Patterson AFB, Ohio 45433 Attn: (ADTN) Lt. David A. Fromme	1
NASA Scientific and Technical Information Facility P. O. Box 8757 Baltimore/Washington International Airport Baltimore, MD 21240	40
Case Western Reserve University 10900 Euclid Avenue Cleveland, Ohio 44106 Attn: Dr. Eli Reshotko	1

Royal Aircraft Establishment
Space Department
Farnborough, Hants, England
Attn: Dr. D. G. Fearn 1

United Kingdom Atomic Energy Authority
Culham Laboratory
Abingdon, Berkshire, England
Attn: Dr. P. J. Harbour 1
Dr. M. F. A. Harrison 1

National Aeronautics and Space Administration
Goddard Space Flight Center
Greenbelt, Maryland 20771
Attn: Mr. W. Isley, Code 734 1
Mr. R. Callens, Code 734 1

Comsat Laboratories
P. O. Box 115
Clarksburg, Maryland 20734
Attn: Mr. B. Free 1
Mr. O. Revesz 1

Rocket Propulsion Laboratory
Edwards AFB, California 93523
Attn: LKDA/Mr. Tom Waddell 1
LKDH/Dr. Robert Vondra 1

DFVLR - Institut für Plasmadynamik
Technische Universitat Stuttgart
7 Stuttgart-Vaihingen
Allmandstr 124
West Germany
Attn: Dr. G. Krülle 1

DFVLR - Institut für Plasmadynamik
33 Braunschweig
Bienroder Weg 53
West Germany
Attn: Mr. H. Bessling 1

Giessen University
1st Institute of Physics
Giessen, West Germany
Attn: Professor H. W. Loeb 1

Jet Propulsion Laboratory
4800 Oak Grove Drive
Pasadena, California 91102
Attn: Dr. Kenneth Atkins 1
Technical Library 1
Mr. Eugene Pawlik 1
Mr. James Graf 1
Mr. Dennis Fitzgerald 1

Electro-Optical Systems, Inc.
300 North Halstead
Pasadena, California 91107
Attn: Mr. R. Worlock 1
Mr. E. James 1
Mr. W. Ramsey 1

TRW Inc.
TRW Systems
One Space Park
Redondo Beach, California 90278
Attn: Mr. M. Huberman 1
Dr. J. M. Selln 1
Dr. Sid Zafran 1

National Aeronautics and Space Administration
Ames Research Center
Moffett Field, California 94035
Attn: Technical Library 1

National Aeronautics and Space Administration
Langley Research Center
Langley Field Station
Hampton, Virginia 23365
Attn: Technical Library 1

Hughes Research Laboratories
3011 Malibu Canyon Road
Malibu, California 90265
Attn: Mr. J. H. Molitor 1
Dr. R. L. Poeschel 1
Dr. Jay Hyman 1
Mr. T. D. Masek 1
Mr. R. Vahrenkamp 1
Dr. J. R. Beattie 1

United States Air Force
Office of Scientific Research
Washington, D. C. 20025
Attn: Mr. M. Slawsky 1

Princeton University
Princeton, New Jersey 08540
Attn: Mr. W. F. Von Jaskowsky 1
Dean R. G. Jahn 1
Dr. K. E. Clark 1

Joint Institute for Laboratory Astrophysics
University of Colorado
Boulder, Colorado 80302
Attn: Dr. Gordon H. Dunn 1

Boeing Aerospace Co.
P. O. Box 3999
Seattle, Washington 98124
Attn: Mr. Donald Grim 1

Intelcom Rad Tech
7650 Convoy Court
P. O. Box 80817
San Diego, California 92138
Attn: Dr. David Vroom 1

Lockheed Missiles and Space Co.
Sunnyvale, California 94088
Attn: Dr. William L. Owens
Propulsion Systems, Dept. 62-13 1

Fairchild Republic Co.
Farmingdale, New York 11735
Attn: Dr. William Guman 1

COMSAT Corporation
950 L'Enfant Plaza SW
Washington, D. C. 20024
Attn: Mr. Sidney O. Metzger 1

Electrotechnical Laboratory
Tanashi Branch
5-4-1 Mukodai-Machi, Tanashi-Shi
Tokyo, Japan
Attn: Dr. Katsuva Nakayama 1

Bell Laboratories
600 Mountain Avenue
Murray Hill, N.J. 07974
Attn: Dr. Edward G. Spencer 1
Dr. Paul H. Schmidt 1

Mass Inst. of Tech.
Lincoln Laboratory
P. O. Box 73
Lexington, Mass. 02173
Attn: Dr. H. I. Smith 1

Sandia Laboratories
Mail Code 5742
Albuquerque, N.M. 87115
Attn: Mr. Ralph R. Peters 1

Service du Confinement des Plasma
Centre d'Etudes Nudéaues - F.A.R.
B.P. 6
92260 Fonteney-aux-Roses
France
Attn: Dr. J. F. Bonal 1